Optoelectronic quantum devices for ultra-strong light-matter interaction at mid-infrared wavelengths

Pierre Jouy

▶ To cite this version:

Université Paris Diderot - Paris 7

ED 518: Matière condensée et interfaces

Ph.D. in Physics

Optoelectronic quantum devices for ultra-strong light-matter interaction at mid-infrared wavelengths

Pierre JOUY

Laboratoire Matériaux et Phénomènes Quantiques (MPQ)

Defended on: february 10th 2012

Jury :

Reviewers :	Alberto BRAMATI
	Karl UNTERRAINER
President :	Cristiano CIUTI
Examinators :	Jean-Jacques GREFFET
	Jean-Sébastien LAURET
Invited :	Raffaele COLOMBELLI
Advisors :	Angela VASANELLI
	Carlo SIRTORI

To Etienne and Ben

Contents

Résumé

Ce travail porte sur la réalisation de dispositifs quantiques fonctionnant en régime de couplage fort entre une excitation d'un gaz d'électrons dans un puits quantique semiconducteur et un mode de cavité dans le moyen infrarouge. Les quasi-particules issues de ce couplage lumière-matière sont appelées "polaritons intersousbande".

La première partie de ce manuscrit est consacrée à l'étude d'un dispositif électroluminescent basé sur une structure à cascade quantique insérée dans une microcavité planaire. Par une analyse détaillée des spectres d'électroluminescence à différents voltages, je démontre que les états de polaritons sont peuplés de façon résonante, à une énergie qui dépend du voltage appliqué à la structure. Les résultats expérimentaux sont analysés et interprétés à l'aide d'un modèle reliant les spectres d'électroluminescence aux propriétés de l'injecteur de la structure à cascade.

Pour augmenter la sélectivité de l'injection et observer ainsi une exaltation de l'émission spontanée, un nouveau type de cavité est développé dans la seconde partie de ce travail. Il s'agit d'une cavité basée sur un confinement plasmonique, dans laquelle la lumière est confinée entre deux plans métalliques, dans une épaisseur très inférieure à la longueur d'onde. Le miroir supérieur est façonné en réseau. L'influence des différents paramètres du réseau est étudiée et deux régimes sont mis en évidence: un régime où le mode de cavité se couple à un mode de plasmon de surface et un régime où le mode de cavité ne présente pas de dispersion en énergie. En insérant des puits quantiques dopés dans une cavité de ce deuxième type, les régimes de couplage fort puis de couplage ultra-fort lumière-matière sont démontrés jusqu'à température ambiante. La valeur importante du dédoublement de Rabi et la forte densité d'états polaritoniques obtenues dans ce type de cavité en font un candidat très prometteur pour la réalisation de dispositifs électroluminescents infrarouges de grande efficacité radiative et fonctionnant sans inversion de population.

Abstract

This work focuses on the realization of quantum devices operating in the strong coupling regime between an excitation of an electron gas in a semiconductor quantum well and a cavity mode in the mid infrared. The quasi-particules issued from this light-matter coupling are called "intersubband polaritons".

The first part of this manuscript is dedicated to the study of an electroluminescent device based on a quantum cascade structure inserted in a planar microcavity. By means of a detailed analysis of the electroluminescence spectra at different voltages, I demonstrate that in this system the polariton states are resonantly populated, at energies depending on the applied bias. The experimental results are analyzed and interpreted by using a model giving the dependence of the electroluminescent spectra on the properties of the injector of the quantum cascade structure.

In order to increase the selectivity of the injection and observe an enhancement of the spontaneous emission, metal-dielectric-metal cavities are designed and realized in the second part of this work. In this cavities, light is confined in a highly subwavelength semiconductor layer. The top gold mirror is patterned into a grating, whose parameters determine the properties of the cavity modes. Two regimes are identified: one in which the cavity mode is coupled to a surface plasmon mode and one in which it presents a flat energy dispersion. By inserting doped quantum wells in a cavity of this second type, the strong and ultra-strong light-matter coupling regimes are demonstrated up to room temperature. The important value of the Rabi splitting and the high polaritonic density of states achievable in this cavity makes it a promising candidate to realize efficient mid infrared electroluminescent devices operating without electronic population inversion.

Introduction

The mid-infrared (MIR) spectral range covers wavelength between approximately $3\mu m$ and $30\mu m$. This domain of the electromagnetic spectrum has two main interests. First, it corresponds to the black body emission between $100K$ and $1500K$ (according to Wien's law). Most of the living creatures, objects and our planet itself will thus emit light in the MIR. A very broad range of applications is possible, from night vision for security purpose to the heat leak detection of buildings for ecological and economical optimization passing by the medical imaging to detect unusual local thermal activity on a patient. The other interest of this spectral region reside in the fact that a lot of molecules present vibrational resonances in the MIR frequencies. This gives easily recognizable spectroscopical features, as each molecule has a peculiar, quite intense, absorption peak at very specific frequencies. Thanks to this property molecules can be, not only detected in very low concentration, but also identified. The applications here are mainly in pollutant (CO_2, NH_3, CH_4,...) or explosives (TNT) detection and medical analyses searching for very low concentrations of certain molecules in non-intrusive breath analyses for example.

The general context of this PhD work is the realization of efficient mid-infrared optoelectronic emitters, based on intersubband transitions (i.e. transitions between confined states of a semiconductor quantum well). This work is motivated by the fact that in these systems the spontaneous emission is characterized by an extremely long lifetime when compared to non-radiative processes, giving rise to devices with very low quantum efficiency (of the order of $10^{-4} - 10^{-5}$). A way to obtain efficient semiconductor emitters in this wavelength range is exploiting stimulated instead of spontaneous emission. The so-called quantum cascade lasers, invented in 1994 [Faist et al., 1994], are today the only semiconductor lasers operating in the mid and far infrared range. Nevertheless, in order to achieve stimulated emission in these devices, one needs to engineer population inversion between the levels involved in the radiative transition. The very low non radiative lifetime of intersubband transitions makes quite difficult to store electrons on excited states and imposes relative high current thresholds.

The aim of this work is to implement novel optoelectronic emitters operating in the strong coupling regime between an intersubband excitation of a two-dimensional electron gas and a microcavity photonic mode. The quasi-particles issued from this strong light-matter coupling are called intersubband polaritons. The strength of the coupling, measured by the vacuum Rabi frequency, is proportional to several parameters, in particular the electronic density of the two dimensional gas, and inversely proportional to the volume of the microcavity. By playing on these parameters it is possible to achieve an unprecedented regime for the light-matter interaction, the so-called ultra-strong coupling regime. In this case the Rabi frequency is of the same order of magnitude as the intersubband transition frequency. In particular this regime can be achieved by using plasmonic microcavities, which allow an extreme light confinement, in volumes that are much smaller than the wavelength to the cube.

The strong coupling regime introduces in the system a novel characteristic time for the light-matter interaction, which is orders of magnitude lower than the spontaneous emission lifetime. By acting on this characteristic time one could think of improving the quantum efficiency of intersubband light-emitting devices. The possibility of merging the subband engineering typical of quantum cascade lasers and the properties of intersubband polaritons is particularly interesting for the realization of this kind of devices. In fact, only few years after the first experimental observation of intersubband polaritons [Dini et al., 2003], an electroluminescent device based on a quantum cascade structure inserted in a microcavity was demonstrated [Sapienza et al., 2008].

This PhD thesis investigates the properties of electroluminescence emitters based on polariton states. The first step is to study its voltage dependence and to relate it to the characteristics of the electrical injection into the polariton branches. We demonstrate that the electroluminescence peak can be strongly tuned with the applied voltage, resulting in the observation of a light signal at frequencies otherwise inaccessible to the electronic transitions of the system. We show that in this device only a small fraction of the electrons is injected into the polariton states. In order to increase this fraction and, as a consequence, the quantum efficiency of the device, we realized new cavities to increase the light-matter coupling (and achieve the ultra strong coupling regime) and to facilitate the selective injection in the polariton states.

This manuscript is organized as follows:

Chapter 1 is used as a general introduction. First, I introduce the main properties of quantum wells and optical absorption between subbands. Then the strong coupling regime between an intersubband excitation and a microcavity mode is introduced. The different parameters that determine the strength of the coupling are discussed. I show that for high values of the cou-

pling strength the properties of intersubband polaritons are strongly modified and the system enters the ultra-strong coupling regime.

Chapter 2 focuses on the passive characterization of an electroluminescent device based on intersubband polaritons. The photon confinement and the polaritonic dispersion are described, by simulating the absorption in the sample. Then, after a brief description of the experimental setup, we show angle resolved absorption measurements and pinpoint that the data must be represented as a function of the inplane wave vector to deduce the correct Rabi frequency.

In **Chapter 3**, we study the electroluminescence of the sample passively characterized in chapter 2. After an introduction and a state of the art of research for electroluminescent devices based on intersubband polaritons, a quick description of the fabrication process and of the experimental setup for electroluminescence is given. It is followed by an angle resolved study for a fixed voltage applied on the sample. I will show that the electroluminescence spectra can be interpreted as the result of a resonant electrical injection into polariton states. Then, voltage dependent measurements are realized to tune the electroluminescence peak energy. Finally, the effect of polaritons on the radiative quantum efficiency of the sample is discussed. In particular I discuss the limiting role of the dark states to improve the radiative efficiency.

In order to increase the Rabi spitting and to facilitate the electrical injection in the polariton states without populating the dark states, we decided to change the photon confinement using metal-dielectric-metal cavities. **Chapter 4** first describes the photon confinement in such cavities. The different steps for the sample fabrication are given and reflectivity measurements are realized to investigate the effects of the different parameters of the cavity.

In **Chapter 5** we insert doped quantum wells in a metal-dielectric-metal cavity in order to demonstrate the strong coupling regime in this type of cavity. Series of reflectivity measurements are realized on three different samples with different doping levels to verify the dependence of the polariton dispersion from the electronic density in the quantum wells. The ultra-strong coupling regime is achieved for the most doped one. Finally, angle resolved measurements allow demonstrating that the energy of the polariton states does not depend on the propagation angle of the light.

Chapter 6 is used to draw the conclusions on the samples studied and perspectives opened by this work. Preliminary results on two novel devices, whose complete characterization is still in progress, are presented in **Appendix** as well as the growth sheets.

Chapter 1

Strong and ultra-strong coupling

Contents

I will briefly present in this chapter a theoretical description of intersubband transitions and the different coupling regimes possible with a cavity mode. The concepts introduced here will be used in the following chapters.

1.1 Quantum wells and intersubband transitions

Quantum wells (QW) are artificial structures created by epitaxial growth of a succession of semiconductor layers (heterostructure) with different band gap energies. This difference results in a discontinuity of the potential energy of the valence and conduction band at the interfaces between the semiconductor layers. In this work, we will only be interested in transitions occurring in the conduction band. The left panel of figure 1.1 schemes with the black con-

tinuous line the conduction band potential ($V(z)$) along the growth direction z of a quantum well made of a $GaAs$ well and $Al_{0.45}Ga_{0.55}As$ barriers.
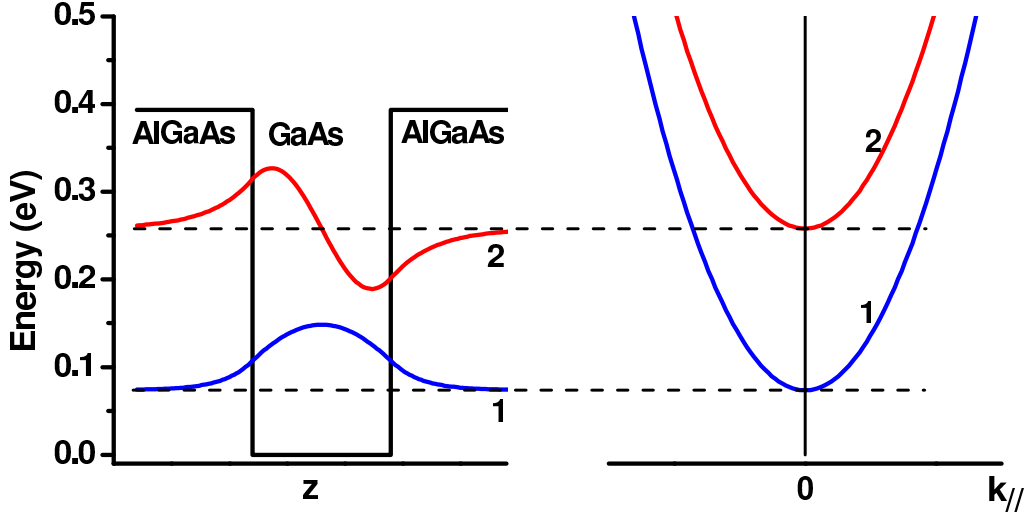
Figure 1.1: Left panel: The black line represents the calculated potential energy created by a $6nm$ thick $GaAs/Al_{0.45}Ga_{0.55}As$ quantum well along the growth direction. The colored curves are the two first wave functions in the QW and are represented at their respective energies. The right panel represents the energy dispersion of the two first states as a function of the inplane wave vector $k_{\parallel}$.

In the envelope function approximation [Bastard, 1988], the wave functions ($\Psi_i(\vec{r})$) are written as the product between the Bloch function $u(\vec{r})$, which has the same periodicity as the crystal lattice and a slowly varying envelope function $f_i(\vec{r})$ sensitive to the conduction band potential created by the QW (the index i refers to the quantum numbers of the state).

$$\Psi_i(\vec{r}) = f_i(\vec{r})u(\vec{r}) \tag{1.1}$$

As $u(\vec{r})$ is the same for both semiconductors (the two semiconductors have the same lattice constant) and assuming an abrupt interface, the electronic confinement can be calculated by solving a Schrödinger-like eigenvalue equation:

$$\frac{-\hbar^2}{2}\vec{\nabla}\left(\frac{1}{m^*(z)}\vec{\nabla}\right)f_i(\vec{r}) + V(z)f_i(\vec{r}) = E_i f_i(\vec{r}) \tag{1.2}$$

where m^* is the electron effective mass and E_i the eigenenergies. Because of the symmetry of the system, the free motion of electrons in the x and y

direction can be separated from the z direction contribution

$$f_{n,k_\parallel}(\vec{r}) = \frac{1}{\sqrt{A}} e^{i\vec{k}_\parallel \cdot \vec{\rho}} \varphi_n(z) \tag{1.3}$$

where A is the sample area, $k_\parallel$ the inplane wave vector and $\vec{r} = (\vec{\rho}, z)$.

The eigenenergies are written as:

$$E_{n,k_\parallel} = E_n + \frac{\hbar^2 k_\parallel^2}{2m^*} \tag{1.4}$$

where E_n are the confined solutions of the one-dimensional problem in the z direction. The confined states associated to energies $E_{n,k_\parallel}$ are called subbands. The subband dispersion is parabolic if the effective mass is constant. The blue and red curves of the left panel in figure 1.1 represent the two first wave functions plotted at the corresponding energy E_n in the conduction band potential. The right panel shows their dispersion as a function of $k_\parallel$. In reality, the coupling between different bands makes the effective mass energy-dependent. In our simulations this effect is taken into account by means of a three band $\vec{k} \cdot \vec{p}$ model [Sirtori et al., 1994]. Note that in this manuscript, the non-parabolicity does not play an important role as we work with $GaAs$, which has a relatively large gap.

Except for few simple cases such as infinite quantum well, the Schrödinger equation cannot be solved analytically. For several coupled quantum wells as in our structures, the result can be numerically calculated using the transfer matrix method. It consists in dividing the structure in blocks in which the potential is constant giving plane-wave solutions and to use the matching conditions at each interface to tie the blocks together. This procedure allows us to calculate the energy and wave functions of the structure at $k_\parallel = 0$.

On another hand, because our devices are highly doped, we need to take into account the potential due to the spatial separation of the localized ionized impurities and the electrons in the structure. Therefore we add to the heterostructure potential in the Schrödinger equation a mean electrostatic potential obtained by the solution of Poisson's equation. An iterative procedure allows us to consistently solve the Schrödinger-Poisson equations by calculating for each step the position of the Fermi level in the structure (i.e. the occupied subbands in the QW structure) and thus deduce the new mean electrostatic potential.

1.2 Intersubband absorption

1.2.1 Absorption coefficients

We now want to describe the transition of an electron between two confined subbands (from an initial state i to a final state f) by means of a photon absorption. The transition rate is given by the Fermi golden rule and the light-matter interaction Hamiltonian can be written in the Coulomb gauge, and neglecting the contributions of the second order in the electric field, as:

$$H' = \frac{-e}{m^*} \vec{A} \cdot \vec{p} \qquad (1.5)$$

where $\vec{A}$ is the vector potential and $\vec{p}$ the electron momentum. Neglecting the photon wave vector compared to the electron momentum, the energy conservation imposes a photon energy equal to the energy difference between the two subbands $(E_f - E_i)$ to be absorbed. In this approximation, known as the dipole approximation, we can obtain the following expression for the transition rate between two conduction subbands:

$$W_{if} = \frac{2\pi}{\hbar} \frac{e^2 E_0^2}{4m^{*2}\omega^2} |\langle i| \vec{e}_z \cdot \vec{p} |f\rangle|^2 \delta(E_f - E_i - \hbar\omega) \qquad (1.6)$$

where $\vec{e}_z$ is the polarization vector and ω the photon frequency. The matrix element $\langle i| \vec{e}_z.\vec{p} |f\rangle$ implies for intersubband transitions that only the z component of the radiation electric field gives rise to an intersubband absorption.

In order to easily compare the transition strengths between different subbands, it is convenient to define the oscillator strength of the transition

$$f_{if} = \frac{2}{m^*\hbar\omega_{if}} |\langle i| p_z |f\rangle|^2 = \frac{2m^*\omega_{if}}{\hbar} |\langle i| z |f\rangle|^2 \qquad (1.7)$$

where ω_{if} is the frequency between the initial and final states. The oscillator strength obeys the sum rule

$$\sum_f f_{if} = 1 \qquad (1.8)$$

and is positive for absorption and negative for emission. For an effective mass depending on the energy, one need to take into account the transitions from the valence band while, for m^* constant, only the transitions in the conduction band need to be taken into account.

For an infinite QW, only parity changing (odd-even or even-odd) transitions are allowed due to the inversion symmetry of the potential. In our devices, the electronic population is always in the fundamental state. In this configuration, only the transition between the first excited state (labeled

2) and the fundamental state (labeled 1) of the QW has a non negligible oscillator strength (f_{12}=0.96 while $f_{14} = 0.03$).

The absorption coefficient for a plane wave is defined as the ratio between the absorbed electromagnetic energy per unit time and volume $\hbar\omega.W_{if}/V$ and the intensity of the incident radiation $\varepsilon_0 c\eta E_0^2/2$ where η is the refractive index of the material [Liu and Capasso, 2000]. When considering a two dimension layer, with an electronic density n_s, the summation over every initial and final states gives the expression:

$$\alpha_{2D} = \frac{\pi e^2}{\varepsilon_0 c\eta\omega m^{*2}} \sum_{if} \frac{1}{(2\pi)^2} \int d^2k_\parallel |\langle i| p_z |f\rangle|^2 \tag{1.9}$$

$$\times [f_{FD}(E_{i,k_\parallel}) - f_{FD}(E_{f,k_\parallel})]\delta(E_{f,k_\parallel} - E_{i,k_\parallel} - \hbar\omega_{if})$$

where $f_{FD}(E)$ is the Fermi-Dirac distribution function. We can replace the δ function by a normalized Lorentzian corresponding to the intersubband (ISB) transition with a full width at half maximum (FWHM) γ_{21} corresponding to its broadening. Assuming a parabolic in-plane dispersion and a zero temperature (energy of the electrons limited by the Fermi energy E_F), the absorption between the first two subbands with only the first one occupied has a lorentzian line shape given by:

$$\alpha_{2D} = \frac{n_s e^2 \hbar}{2\varepsilon_0 c\eta m^*} f_{12} \frac{\gamma_{21}/2}{(E_2 - E_1 - \hbar\omega)^2 + \gamma_{21}^2/4} \tag{1.10}$$

1.2.2 Depolarization shift

The description until now is valid for low doped materials ($n_s \approx 10^{10} - 10^{11}cm^{-2}$) which implies $\alpha_{2D} << 1$. In the following I will consider highly doped QWs. In this case it is important to consider the effect of the Coulomb interaction on the absorption frequency. Indeed, an electron in a 2DEG (two dimensional electron gas) is sensitive to the external radiation excitation but also to the oscillation of the other electrons due to the external radiation. These oscillations induce an a.c. current that can be written as

$$j_z = \sigma_{zz}E \tag{1.11}$$

where σ_{zz} is the z component of the two dimensional conductivity and E the total electric field. The electric field of the external radiation E_{ext} is related to E through

$$E_{ext} = \varepsilon_{zz}E \tag{1.12}$$

where ε_{zz} is the dielectric function given by

$$\varepsilon_{zz} = 1 + i\frac{\sigma_{zz}}{\varepsilon_0 \varepsilon_{st} \omega L_{eff}} \qquad (1.13)$$

with ε_0 is the vacuum permittivity, ε_{st} the static background dielectric constant and L_{eff} the effective width of the quantum well [Ando et al., 1982]. We can introduce the modified effective conductivity $\tilde{\sigma}_{zz}$ defined as $j_z = \tilde{\sigma}_{zz} E_{ext}$. Equations 1.11, 1.12 and 1.13 give together the following expression:

$$\tilde{\sigma}_{zz} = -i\varepsilon_0 \varepsilon_{st} \omega L_{eff} \frac{\varepsilon_{zz} - 1}{\varepsilon_{zz}} \qquad (1.14)$$

The absorption per unit area is proportional to $\mathrm{Re}\{\tilde{\sigma}_{zz}\}$, i.e. to $\mathrm{Im}\{(1 - \varepsilon_{zz})/\varepsilon_{zz}\}$. The energy position of the absorption peaks is hence related to the zero of the dielectric function. In our work, only the transition between the two first subbands will be used. Therefore ε_{zz} can be written as

$$\varepsilon_{zz}(\omega) = 1 - \frac{n_s e^2 f_{12}}{m^* \varepsilon_0 \varepsilon_{st} L_{eff}} \frac{1}{\omega^2 - \omega_{21}^2 + i\gamma\omega} \qquad (1.15)$$

Replacing equation 1.15 in equation 1.14, we finally obtain

$$\tilde{\sigma}_{zz}(\omega) = \varepsilon_0 \varepsilon_{st} \omega L_{eff} \frac{i\omega_P^2}{\omega^2 - \tilde{\omega}_{21}^2 + i\gamma\omega} \qquad (1.16)$$

where

$$\tilde{\omega}_{21} = \sqrt{\omega_{21}^2 + \omega_P^2} \quad with \quad \omega_P^2 = \frac{f_{12} n_s e^2}{m^* \varepsilon_0 \varepsilon_{st} L_{eff}} \qquad (1.17)$$

ω_P is known as plasma frequency. The effect of the Coulomb interaction on the absorption spectrum is a renormalization of the transition frequency towards higher values. This phenomenon have been addressed in [Załużny, 1991] and described in [Liu and Capasso, 2000].

1.3   Weak and strong coupling regime

We now want to describe the interaction between a confined cavity photon and an intersubband transition occurring when a doped QW is placed in a photonic cavity.

1.3.1   One particle description

To simplify we will first consider the cavity and only one electron on the intersubband transition. An easy analogy can be made with two oscillators

(one corresponding to the ISB transition and one corresponding to the cavity mode) coupled together through an interaction term $\hbar\Omega$. We note $|g, 1\rangle$ the state where the electron is in the ground state of the transition with one photon in the cavity and $|e, 0\rangle$ the state where the electron is in the excited state of the transition with no photon in the cavity. We note E_{21} the intersubband transition energy and E_c the energy of the cavity photon. The Hamiltonian of the system can be written as:

$$H = \begin{pmatrix} E_{21} & \hbar\Omega \\ \hbar\Omega^* & E_c \end{pmatrix} \tag{1.18}$$

After diagonalization we find the eigenstates of the system as a linear combination of the two states $|g, 1\rangle$ and $|e, 0\rangle$:

$$\begin{cases} |\psi_+\rangle = \cos\alpha \, |g, 1\rangle + i \sin\alpha \, |e, 0\rangle \\ |\psi_-\rangle = i \sin\alpha \, |g, 1\rangle + \cos\alpha \, |e, 0\rangle \\ tan2\alpha = \frac{\hbar\Omega}{E_{21} - E_c} \end{cases}$$

Those states possess an electronic and a photonic component whose ratio is solely determined by the energy difference between the ISB transition and the cavity photon and by the coupling between them. The corresponding energies are obtained by solving the eigenvalue equation for H:

$$(E_{21} - E)(E_c - E) = |\hbar\Omega|^2 \tag{1.19}$$

The energy dispersion of the two states is plotted with black curves as a function of the energy difference $\delta = E_{21} - E_c$ in figure 1.2. The horizontal dashed line represents the intersubband transition energy E_{21} and the oblique dashed line represents the cavity mode energy E_c. When $|E_{21} - E_c| >> 1$, the two branches tend to the intersubband and the cavity mode energies. On the contrary, when $E_{21} \approx E_c$, an anti-crossing appears which is the signature of the strong coupling regime. The state corresponding to the energy E_+ is called upper polariton (UP) and the one at E_- is the lower polariton (LP). At resonance, the energy difference between the two polaritons is

$$2\hbar\Omega_R = E_{+ \, res} - E_{- \, res} \tag{1.20}$$

where Ω_R is the *vacuum Rabi frequency* in analogy to the strong coupling regime for atoms in high finesse cavities [Raimond et al., 2001].

The dual light/matter nature of the strong coupling can also be seen by studying the temporal evolution of the state $|e, 0\rangle$. This is not an eigenstate of
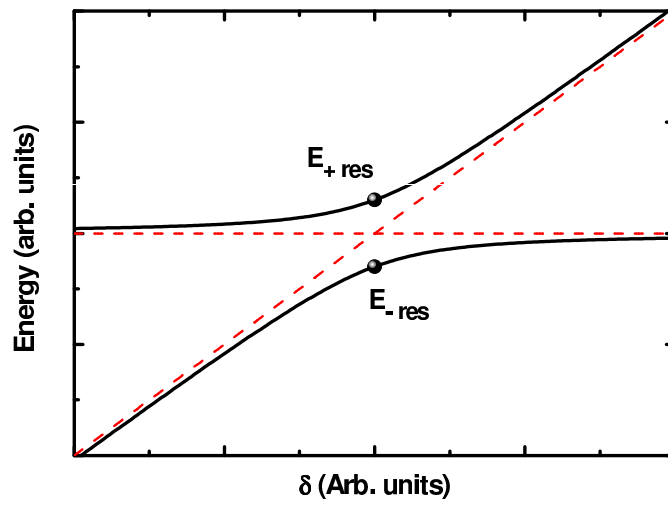
Figure 1.2: Polariton branches (black curves) energy dispersion as a function of the energy difference between the cavity mode and the intersubband transition calculated from equation 1.19. The red dashed lines represents the ISB transition (constant energy) and the cavity mode energy (dispersive energy). The black dots correspond to the energies of the two polariton branches when the cavity mode and the intersubband transition energies are resonant.

the system but it can be written as $|e,0\rangle = 1/\sqrt{2}(|\psi_+\rangle + |\psi_-\rangle)$. Its temporal evolution is thus given by

$$\psi(t) = \frac{1}{\sqrt{2}}\left[\exp\left(\frac{-iE_+t}{\hbar}\right)|\psi_+\rangle + \exp\left(\frac{-iE_-t}{\hbar}\right)|\psi_-\rangle)\right]$$

$$= \exp(-i\omega t)\left[\cos\left(\Omega_R t\right)|e,0\rangle - i\sin\left(\Omega_R t\right)|g,1\rangle\right] \qquad (1.21)$$

The probability for the system to be in the state $|e,0\rangle$ as a function of the time is thus:

$$P(t) = |\langle e,0|\psi(t)\rangle|^2 = \cos^2(\Omega_R t) \qquad (1.22)$$

This means that the system oscillates between the states $|e,0\rangle$ and $|g,1\rangle$. These oscillations are called *Rabi oscillations* as they directly depend on the Rabi frequency.

As the intersubband transition and the cavity mode have a finite lifetime, we introduce damping terms in equation 1.19. The solutions write:

$$E_\pm = \frac{E_{21} + E_c}{2} - i\frac{\gamma_{21} + \gamma_c}{2} \pm \frac{\sqrt{(E_{21} - E_c - i(\gamma_{21} - \gamma_c))^2 + |\hbar\Omega|^2}}{2} \qquad (1.23)$$

where γ_{21} and γ_c are the linewidth of respectively the ISB transition and the cavity mode. In particular, when the cavity mode is at resonance with the intersubband transition energy,

$$E_{\pm\ res} = E_{21} - i\frac{\gamma_{21} + \gamma_c}{2} \pm \frac{1}{2}\sqrt{-(\gamma_{21} - \gamma_c)^2 + |\hbar\Omega|^2} \qquad (1.24)$$

Two different regimes can thus take place. If $(\gamma_{21} - \gamma_c) > \hbar\Omega$, the square root is imaginary and the degeneracy between the two states is not removed. Only the energy broadening of the two states are affected by the coupling. This corresponds to the *weak coupling regime*. On the contrary, if $(\gamma_{21} - \gamma_c) < \hbar\Omega$, the two states have different energies and enter the *strong coupling regime*.

Because the ISB transition and the cavity mode broadening are approximately the same in our samples, it is possible to satisfy the previously mentioned strong coupling condition even with a small Rabi frequency and in particular with $2\hbar\Omega_R \ll \gamma_{21} + \gamma_c$. In this condition, it is impossible to experimentally observe the splitting between the polaritons as it is smaller than the broadenings of the ISB transition and the cavity mode. Therefore we choose a different criterion to discriminate between the strong and weak coupling regime. In atomic physics the relevant parameter for characterizing cavity quantum electrodynamics systems is their cooperativity, which

relates the reversible dipole coupling (Rabi frequency) and the irreversible coupling to the reservoirs (losses of the cavity mode and intersubband transition) [Foster et al., 2000]. This parameter is defined by

$$C = \frac{\hbar^2 \Omega_R^2}{\gamma_{21} \gamma_c} \qquad (1.25)$$

In our case, because $\gamma_{21} \approx \gamma_c$ (giving $C \approx \hbar^2 \Omega_R^2 / \gamma_{21}^2$), the experimental condition $2\hbar\Omega_R > \gamma_{21} + \gamma_c$ necessary to observe the strong coupling can be expressed as $\hbar\Omega_R > \gamma_{21}$. The strong coupling regime is thus visible when $C > 1$.

1.3.2 2D electron gas and dark states

In the devices studied during my PhD, the strong coupling regime is achieved using a cavity mode and an intersubband transition of a two dimensional electron gas (2DEG). We thus need to describe the light-matter interaction for several electrons participating to the ISB excitation excited by one photon only.

The Hamiltonian of such a system with N excitations coupled to the same cavity mode is given by:

$$H = \begin{pmatrix} E_c & \hbar\Omega & \hbar\Omega & \cdots & \hbar\Omega \\ \hbar\Omega^* & E_{21} & 0 & \cdots & 0 \\ \hbar\Omega^* & 0 & E_{21} & \cdots & 0 \\ \vdots & \vdots & \vdots & \ddots & \vdots \\ \hbar\Omega^* & 0 & 0 & \cdots & E_{21} \end{pmatrix} \qquad (1.26)$$

This Hamiltonian can be rewritten as:

$$H = \begin{pmatrix} E_c & \hbar\Omega\sqrt{N} & 0 & \cdots & 0 \\ \hbar\Omega^*\sqrt{N} & E_{21} & 0 & \cdots & 0 \\ 0 & 0 & E_{21} & \cdots & 0 \\ \vdots & \vdots & \vdots & \ddots & \vdots \\ 0 & 0 & 0 & \cdots & E_{21} \end{pmatrix} \qquad (1.27)$$

The light-matter interaction can hence be studied by considering a single oscillator interacting with the cavity mode with a coupling constant $\Omega\sqrt{N}$. The other $N-1$ oscillators are not coupled to the light. They are thus called *dark states* as they do not have any photonic component and are only matter excitations at the energy E_{21}. In contrast, the state coupled with light is called *bright state*.

The strong coupling regime between an intersubband excitation of a 2DEG and a micro-cavity photon mode has been first observed in [Dini et al., 2003], by using a planar waveguide. In this case the Rabi frequency is given by:

$$\Omega_R = \left(\frac{2\pi e^2}{\varepsilon_\infty m_0 L_{eff}} N_{2DEG} n_{QW} f_{21} \sin^2\theta \right)^{1/2} \tag{1.28}$$

where ε_∞ is the dielectric constant of the cavity, m_0 is the free electron mass, L_{eff} is the effective cavity thickness, N_{2DEG} the electronic density of the 2DEG, n_{QW} the number of quantum wells coupled to the cavity mode, f_{21} the oscillator strength of the intersubband transition and θ is the angle of propagation of the light in the cavity. In the case where the cavity is completely filled with QWs, the effective cavity thickness can be written as $L_{eff} = n_{QW} \times L_P$ where L_P is the length of the period containing the QW. It is interesting to notice that the splitting is proportional to $\sqrt{1/L_P}$ and to $\sqrt{N_{2DEG}}$. It is thus possible to widen the splitting by either decreasing the length of a period or by increasing the doping in the structure, i.e. enhencing the electronic density of the 2DEG [Anappara et al., 2005].

1.4 Ultra-strong coupling regime

The description given above works well when considering a system where the Rabi frequency represents a small fraction of the ISB transition. Nevertheless, if the ratio $2\hbar\Omega_R/E_{21}$ becomes important, we reach the so called *ultra-strong coupling regime*. In this case, the system is described by the following Hamiltonian [Todorov et al., 2010a] :

$$H = E_c(a^\dagger a + 1/2) + E_{21} b^\dagger b + \frac{iE_P}{2}\sqrt{f_w \frac{E_c}{E_{21}}}(a - a^\dagger)(b + b^\dagger) + \frac{E_P^2}{4E_{21}}(b + b^\dagger)^2 \tag{1.29}$$

where $a^\dagger$ is the photonic creation operator and $b^\dagger$ is the creation operator of an intersubband excitation, $f_w = L_{QW}/L_{cav}$ is the overlap factor between the QW containing the 2DEG and the cavity mode and E_p is the plasma energy ($\hbar\omega_P$). Introducing a new polarization operator

$$p = \frac{\tilde{E}_{21} + E_{21}}{2\sqrt{\tilde{E}_{21}E_{21}}} b + \frac{\tilde{E}_{21} - E_{21}}{2\sqrt{\tilde{E}_{21}E_{21}}} b^\dagger \tag{1.30}$$

we can write the Hamiltonian as

$$H = E_c(a^\dagger a + \frac{1}{2}) + \tilde{E}_{21} p^\dagger p + i\frac{E_P}{2}\sqrt{f_w \frac{E_c}{\tilde{E}_{21}}}(a - a^\dagger)(p + p^\dagger) \tag{1.31}$$

The eigenvalues are:

$$(E^2 - \tilde{E}_{21}^2)(E^2 - E_c^2) = f_w E_P^2 E_c^2 \tag{1.32}$$

where $\tilde{E}_{21} = \sqrt{E_{21}^2 + E_P^2}$ is the renormalized ISB transition energy due to the depolarization shift. The energies of the polariton states become

$$E\pm = \sqrt{\frac{E_c^2 + \tilde{E}_{21}^2 \pm \sqrt{(E_c^2 - \tilde{E}_{21}^2)^2 + 4(2\hbar\Omega_R)^2 E_c^2}}{2}} \tag{1.33}$$

With these notations, the Rabi frequency is given by $2\hbar\Omega_R = \sqrt{f_w}E_P$. The minimum splitting between the two states does not occurs for $E_c = E_{21}$ anymore but for $E_{c\ min} = E_{21}\sqrt{1 + \frac{E_P^2}{E_{21}^2}(1 - f_w)}$. An energy gap appears as well between the asymptote of the UP when $E_{21} >> E_c$ which tends to $\tilde{E}_{21}$ and the one of the LP when $E_{21} << E_c$ which tends to $E_{c\ min}$. It is schematized in figure 1.3 where the LP and UP branches are represented as a function of $\tilde{E}_{21} - E_{c\ min}$ as well as the two asymptotes of the polariton branches.
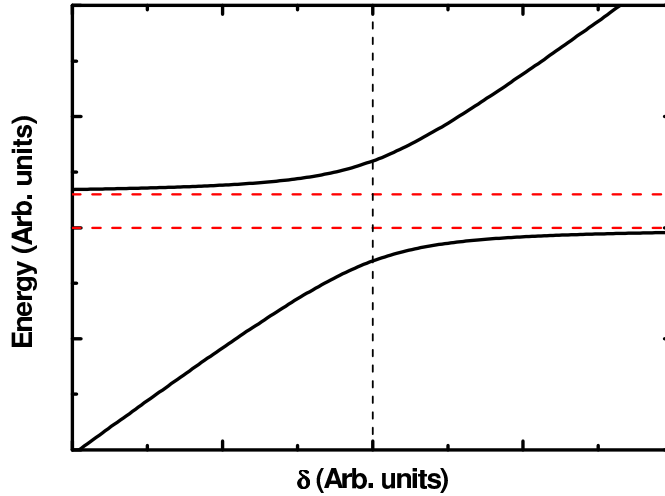

Figure 1.3: Polariton branches (black curves) energy dispersion as a function of the energy difference between the cavity mode and the intersubband transition calculated from equation 1.33. The red dashed lines represents the photonic energy gap between the two polariton branches asymptotes.

The energy gap is given by

$$E_g = \tilde{E}_{21} - E_{c\ min} \approx f_w(\tilde{E}_{21} - E_{21}) = \frac{(2\hbar\Omega_R)^2}{2E_{21}} \tag{1.34}$$

and is only visible if the depolarization shift is important (i.e. for a high electronic density in the 2DEG) or equivalently for an important value of the ratio $2\hbar\Omega_R/E_{21}$. As discussed in [Todorov et al., 2010a], this gap directly results from equation 1.32 and has its origins in the quadratic and antiresonant terms of the light-matter interaction Hamiltonian. As a consequence, given the line width of the ISB transitions, the observation of a polaritonic gap in the dispersion curve can be taken as the experimental signature of the ultrastrong coupling regime.
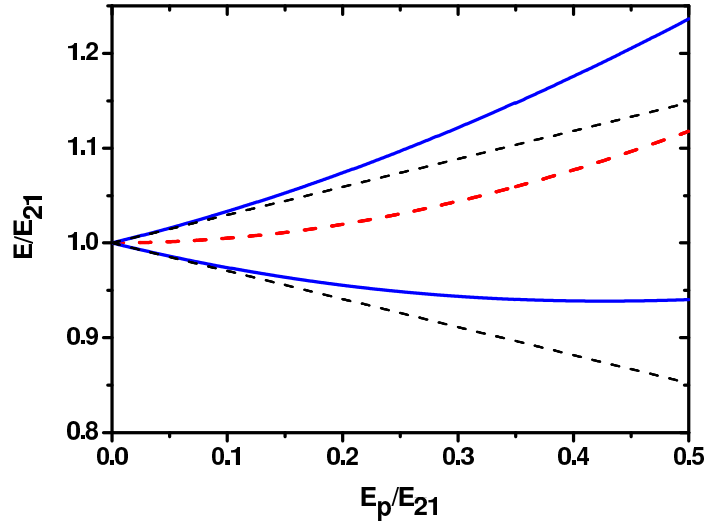

Figure 1.4: The blue curves represent the polariton branches normalized energy dispersion following equation 1.33 as a function of the normalized plasma energy. The black dashed lines correspond to the linear approximation (equation 1.19) and the red dashed curve corresponds to $\tilde{E}_{21}/E_{21}$.

Figure 1.4 represents the two polariton energies calculated with $f_w = 0.35$ (blue continuous lines) normalized by the intersubband transition energy for $E_c = E_{c\ min}$ as a function of E_P/E_{21}. It clearly appears that the branches follow the linear approximation (dashed black lines) for $E_P << E_{21}$. For higher plasma energies the dispersion is clearly non linear and we enter into the ultra-strong coupling regime. Remarkably this occurs already when E_P is of less than one order magnitude smaller than E_{21}. The red dashed line represents $\tilde{E}_{21}/E_{21}$.

Chapter 2

Absorption of the polaritonic states

Contents

2.1   Introduction

The first intersubband electroluminescent device operating in the light-matter strong coupling regime was demonstrated in reference [Sapienza et al., 2008]. I started my PhD working on this device to investigate the physical properties of the electrical injection process. The sample is based on a quantum cascade structure (QCS) inserted in a planar micro cavity.

The first aim of this chapter is to describe the cavity and the active region. The cavity mode dispersion is then presented and the so called "k space" which represents the energy dependence of the mode as a function of the

inplane wavevector. The following section is dedicated to the simulations of
the cavity mode energy dispersion and of its modification when coupled with
the 2DEG in the sample. After a brief presentation of the experimental set
up, the polaritonic dispersion obtained thanks to transmission measurements
will be presented and the importance of the k space to determine the Rabi
splitting underlined. The main results shown here have been published in
[Todorov et al., 2008] and [Jouy et al., 2010].

The active operation of the device, investigated by means of voltage and
angle dependent electroluminescence measurements, will be the object of the
next chapter.

2.2   Sample description

The sample is composed of two parts: an optical cavity and a core made
of $GaAs/Al_{0.45}Ga_{0.55}As$ quantum wells. The detailed growth sheet of the
sample is presented in appendix B.1. It has been grown by U. Gennser at LPN
(Laboratoire de Photonique et de Nanostructures). As sketched in figure 2.1,
the cavity is made of a metallic mirror on top and of two low refractive index
layers (compared to the QCS) on the bottom. The low refractive index layers
are a $560nm$ thick $GaAs$ layer Si doped and a $520nm$ thick $Al_{0.95}Ga_{0.05}As$
layer. The substrate is an undoped $GaAs$ $450\mu m$ thick wafer. Light is confined
by total internal reflection between the gold and the low refractive index layers.
From now on our convention will be to use z as the growth direction and $/\!/$
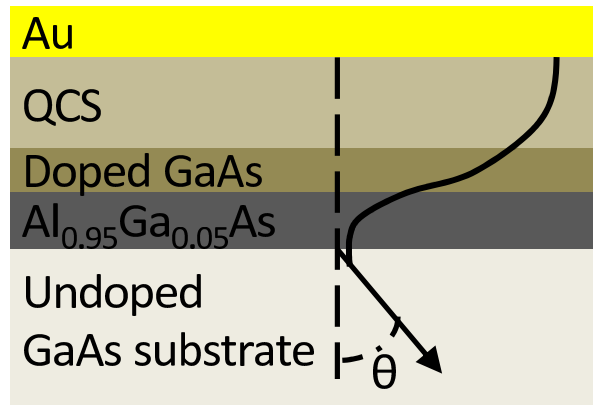for a vector in the layers plane $(\widehat{xOy})$.

Figure 2.1: Scheme of the device. θ is the angle of light propagation in the
substrat and the black continuous line represents the cavity mode vertical
electric field intensity.

The active region (AR) consists of a $GaAs/Al_{0.45}Ga_{0.55}As$ quantum cascade structure (QCS) composed by 30 periods. Each period consist of a main quantum well and an injection/extraction region, Si doped in order to have a two dimensional electron gas (2DEG) in the main well. Figure 2.2 represents the computed band diagram of two periods of the QCS as a function of z under a bias of $6V$. It is calculated by solving self consistently the Schrödinger and Poisson equations of the system. The black line represents the conduction band profile and the colored curves represent the square moduli of the wave functions plotted at the corresponding energy. The ground and excited states of the intersubband transition are in bold color line and respectively labeled 1 and 2. The calculated intersubband transition energy is $E_{21} = E_2 - E_1 = 163meV$. In the injector region, the quantum wells widths are engineered so that the wavefunctions create a triangular shaped mini-band (schematized with a red triangle) that collects electrons on a broad energy range and bring them to a single wave function (the injector state, corresponding to the purple wave function in the band diagram) tunnel coupled to the excited state of the main quantum well. The main quantum well is used for the photon emission at the energy E_{21}. Finally the extraction region (blue triangle) allows to extract electrons from subband 1 and to inject them in the following period of the QCS (the extraction of a period corresponds to the injection of the next one). By varying the applied voltage it is possible to tune the energy of the injector level with respect to level 1 and 2.

Figure 2.3 shows the calculated band diagram of the structure with no bias applied to the structure. The Fermi level is $10.7meV$ above level 1. This electronic population in the main QW allows photon absorption giving the possibility to experimentally test the photonic dispersion of our sample. By performing transmission measurements we can thus obtain the dispersion in the strong coupling regime of our device.
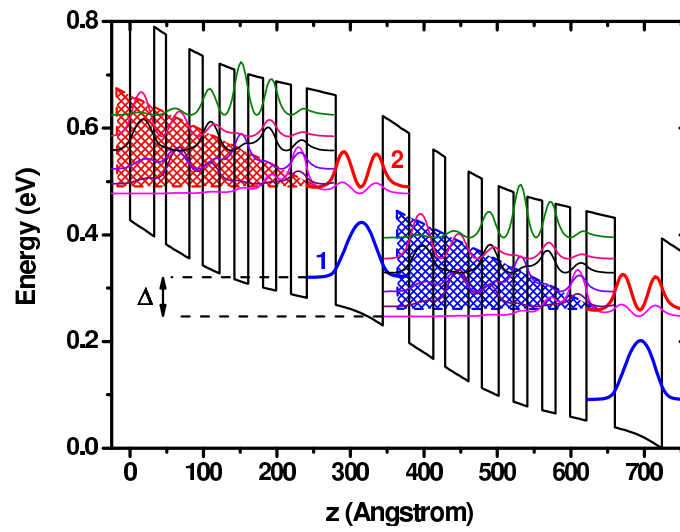
Figure 2.2: Band diagram of the quantum cascade structure at a voltage of $6V$ obtained by solving coupled Schrödinger and Poisson equations. The colored curves are the square moduli of the wave functions in the QWs and are represented at their respective energies. The red (blue) triangle schemes the injection (extraction) miniband. The fundamental and excited state of the ISB transition are in bold and respectively labeled 1 and 2. Δ is the energy difference between 1 and the injector quasi-Fermi energy of the following injection miniband.
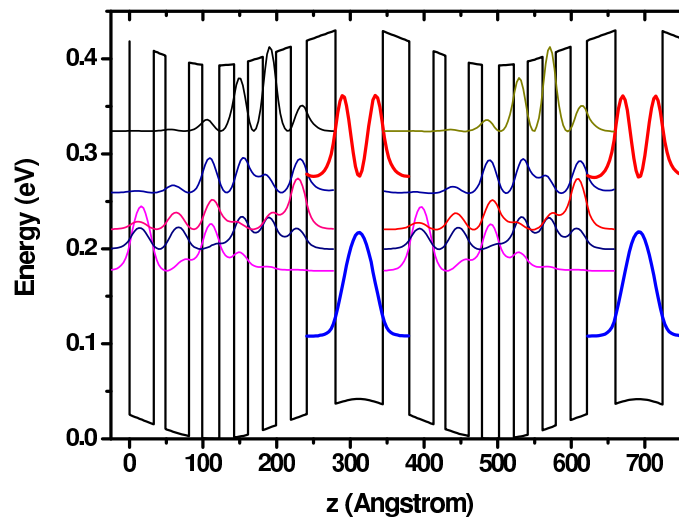

Figure 2.3: Simulated band diagram of the QCS with no applied voltage.

2.3 Description of the cavity mode

As mentioned in the previous section, photons are vertically confined between the top gold mirror and the low refractive index layers thanks to total internal reflection. This cavity behaves as a $\lambda/2$ resonator in which the wavelength must satisfy

$$\lambda = \frac{2Ln_{eff}}{K} \tag{2.1}$$

where L is the cavity thickness, K the mode index and n_{eff} is the effective index of the optical mode. Figure 2.4 represents the vertical electric field intensity (blue curve) along the z direction together with the optical index of the different layers (green curve). As one can see, a plasmonic mode "sticks" to the gold layer and most of its amplitude is located in the QCS region. It is important to notice that the mode is leaking in the substrate as the electric field is not equal to zero after the low refractive index layers. Because the
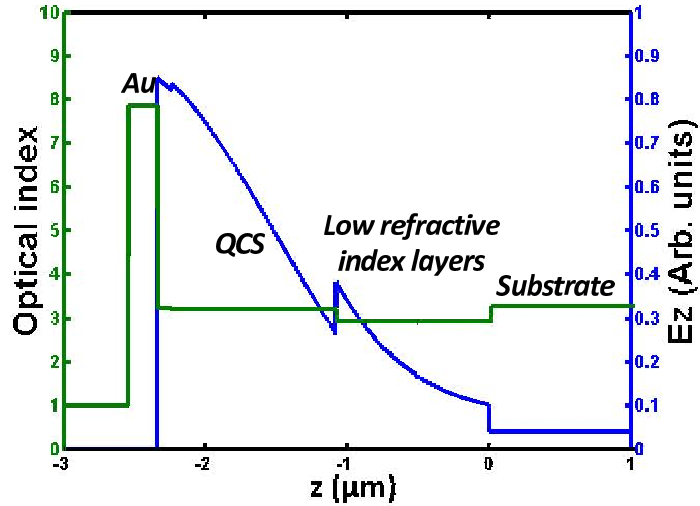

Figure 2.4: The blue (green) curve represents the simulated cavity mode vertical electric field intensity E_z (the optical refractive index) as a function of the position along the z axis in the cavity.

GaAs substrate is undoped, it is transparent for the MIR domain. It is thus possible to couple the free space and the cavity mode for optical injection or extraction through the substrate thanks to the leaky tail of the mode.

If we remove the gold on top of the AR, the refractive index difference between the air and the AR still allows to confine light thanks to total internal reflection. This is shown in figure 2.5 where the optical index of the different layers (green curve) and the confined electric field (blue curve) along the z

direction are represented. In this case the overlap of the QCS region and the cavity mode is decreased by a factor 1.77 compared to the case with metal on top and the mode leaks much more on both sides.
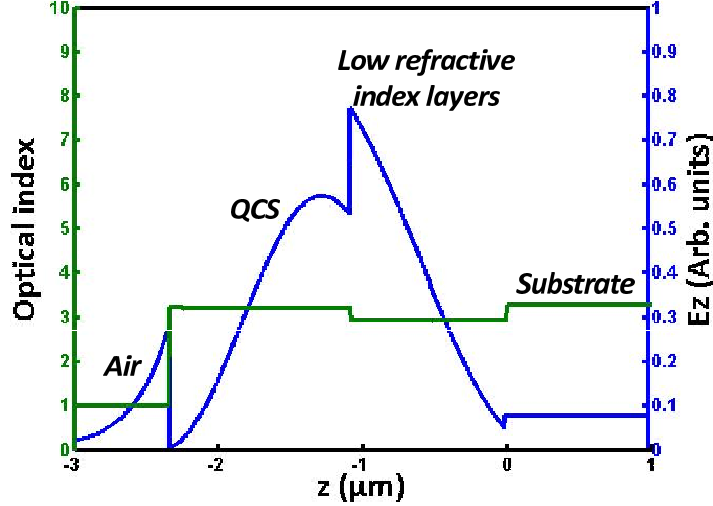

Figure 2.5: The blue (green) curve represents the simulated cavity mode vertical electric field intensity E_z (the optical refractive index) as a function of the position along the z axis in the sample without the top metallic mirror.

In our planar cavity, while the photons are confined in the z direction, they remain free in the layer plane. As a consequence, the inplane photon wave vector $k_\parallel$ can be continuously tuned giving rise to a dispersive mode energy. Figure 2.6 illustrates the energy dispersion as a function of the inplane momentum, the so called "k space". The black line represents the energy of the first cavity mode as a function of $k_\parallel$ which is given by:

$$E = \frac{\hbar c}{n_{eff}} \sqrt{k_\parallel^2 + k_z^2} \quad \text{with} \quad k_z = \frac{2\pi n_{eff}}{\lambda} \tag{2.2}$$

At $k_\parallel = 0$, the energy is minimal while, for $k_\parallel \gg k_z$ it increases linearly with the inplane wave vector. The inplane component of the wave vector can be changed by changing the angle of propagation θ (defined in figure 2.1) in the substrate. θ is related to $k_\parallel$ through the equation

$$k_\parallel = \frac{n_{sub} E \sin\theta}{\hbar c} \tag{2.3}$$

with c the light velocity and n_{sub} the substrate optical index. By increasing θ the cavity mode energy increases. Each angle corresponds to a different cavity
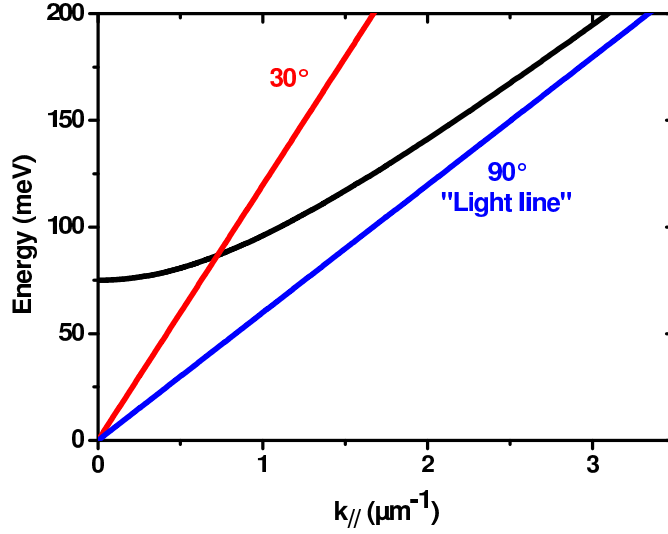
Figure 2.6: Calculated energy dispersion of the first order cavity mode as a function of the inplane wave vector (black curve). The red and blue lines represents the energy dispersion of equation 2.3 for θ respectively equal to 30° and 90°.

energy and it is therefore possible to continuously tune it by only changing the angle of propagation in the substrate. To illustrate how a spectra at a given angle contributes to the k space, the red and black lines in figure 2.6 respectively indicate the energies at $\theta = 30°$ and $\theta = 90°$. The one at 90° is called the light line and corresponds to the maximum inplane wave vector value reachable for a propagating wave at the energy E. It is given by

$$k_{\parallel\ max} = \frac{n_{sub}E}{\hbar c} \tag{2.4}$$

It is important to note that θ is not the appropriate quantum number to characterize the system. In the following I will show that it is necessary to plot the optical spectra in the k space to obtain the correct dispersion of the system.

Note that the optical index is of 3.3 for the AR and 2.9 for the low refractive index layers. The Snell-Descartes formula

$$n_{AR}sin\theta_{AR} = n_{AlAs}sin\theta_{AlAs} \tag{2.5}$$

implies that the total internal reflection in the cavity only occurs for 61.5° $<\theta<$90°. In this region, the photon confinement is optimal. For smaller angles, the cavity mode becomes more leaky, increasing its broadening (see figure 2.7 in the next section).

2.4   Simulations of the system

2.4.1   Absorption through the cavity

To simulate the absorption through the multi-layer system I used the transfer-matrix formalism in which the optical index at a given wavelength of each layer of the AR is calculated according to its Si doping level and Al concentration. By considering that the transmission through the top gold layer is zero, the absorption spectrum A is taken as $A = 1 - R$ where R is the reflectivity at the $Al_{0.95\%}Ga_{0.05\%}As/GaAs_{substrate}$ interface. We first neglect the contribution of the electron gas in the QW to the absorption spectra. In figure 2.7, the absorption is plotted in color scale (red is the maximum absorption and blue the minimum) as a function of the inplane wave vector $k_{/\!/}$ and the photon energy E. The green line represents the light line. The dashed red line represents the designed intersubband transition energy. Two different features can be observed here: the fundamental cavity mode with a FWHM (Full Width at Half Maximum) of less than $2.5meV$ at $160meV$ appearing close to the light line and the second order cavity mode much broader with a FWHM of about $25meV$ at $160meV$ and appearing at lower $k_{/\!/}$. Figure 2.8 represents the absorption coefficient as a function of $k_{/\!/}$ for an energy of $160meV$ (as represented by the red dashed line on figure 2.7) and clearly shows the two modes. The first cavity mode is at resonance with the intersubband transition energy at $k_{res} = 2.5\mu m^{-1}$ corresponding to $\theta \approx 72.5°$ and the excited cavity mode at $k_{exc} = 1.9\mu m^{-1}$ corresponding to $\theta \approx 55°$.

The simulation of the absorption corresponding to the sample without the top metallic mirror is plotted in color scale as a function of $k_{/\!/}$ and the photon energy in figure 2.9. The dashed red line represents the intersubband transition energy and the green curve represents the light line. As figure 2.10 shows, the cavity mode is at resonance with the intersubband transition energy for $k_{res} = 2.25\mu m^{-1}$ corresponding to an angle $\theta \approx 59°$. The cavity mode FWHM is here of about $12.5meV$ and is much broader than for the fundamental mode of the sample with the metal on top.

2.4.2   Coupling between the cavity mode and the ISB transition

The interaction between the 2DEG and the cavity mode is simulated by considering the 2DEG as a collection of Lorentz oscillators. The left panel of figure 2.11 corresponds to the simulated k space of the sample with gold on top. Two features appear at the intersubband transition energy: an anti crossing occurs at k_{res} while a peak of intensity is observed for k_{exc}. This is shown in
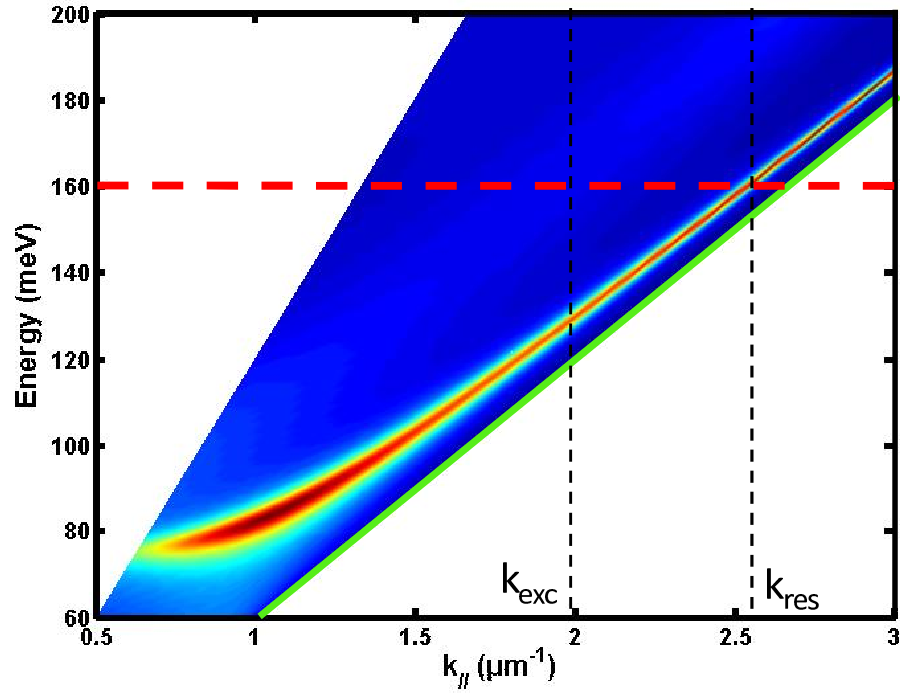
Figure 2.7: Contour plot for the simulation of the absorption coefficient of the device with the top mirror, without including the contribution of the intersubband transition. The color scale represents the absorption intensity (blue for no absorption and red for the maximum absorption) as a function of the inplane wave vector and of the energy. The position of the intersubband transition is plotted with a red dashed line. The inplane wave vectors corresponding to the resonance between the first (second) order cavity mode and the ISB transition is labeled k_{res} (k_{exc}). The green line corresponds to the light line.
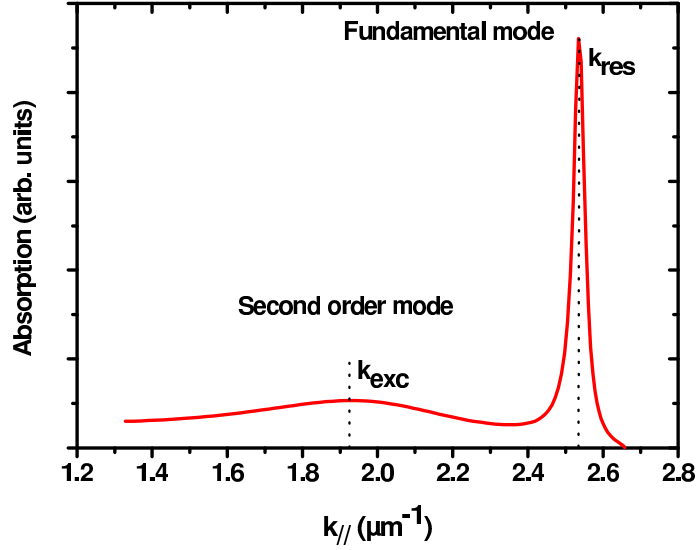
Figure 2.8: Simulated absorption intensity as a function of the inplane wave vector at $E = 160 meV$ for the sample with top metallic mirror.

the right panel of figure 2.11 where we plot the spectrum at k_{res} (red curve) and k_{exc} (black curve). The first spectrum presents two peaks corresponding to the polariton branches (the asymmetry is due to the light line that cuts a part of the spectrum) while the second has only one peak centered at the bare transition energy. The transition is therefore in strong coupling regime with the fundamental cavity mode and in weak coupling regime with the excited cavity mode. These behaviors are due to the fact that, as discussed in the first chapter, the strong coupling regime is achieved only when the condition $\Gamma_{cav}\Gamma_{21} < \Omega_R^2$ is satisfied. There Γ_{21} is the nonradiative broadening of the intersubband transition and Γ_{cav} is the cavity mode broadening.

The left panel of figure 2.12 corresponds to the simulated k space of the sample without gold on top. For this sample, the strong coupling regime cannot be achieved due to the width of the cavity mode. The spectrum at k_{res} is shown in the right panel of figure 2.12. Only one broad peak appears at the intersubband transition energy corresponding to the weak coupling regime. This sample will be thus considered as the weak coupling reference of the previous one. We will conveniently use both samples in the next chapter to illustrate the differences between strong and weak coupling and compare these two regimes.

Figure 2.9: Contour plot for the simulation of the cavity modes dispersion as a function of the inplane wave vector for the sample without top metallic mirror, without including the contribution of the intersubband transition. The position of the intersubband transition is plotted with a red dashed line. The inplane wave vectors corresponding to the resonance between the broad cavity mode and the ISB transition is labeled k_{res}. The green line corresponds to the light line.
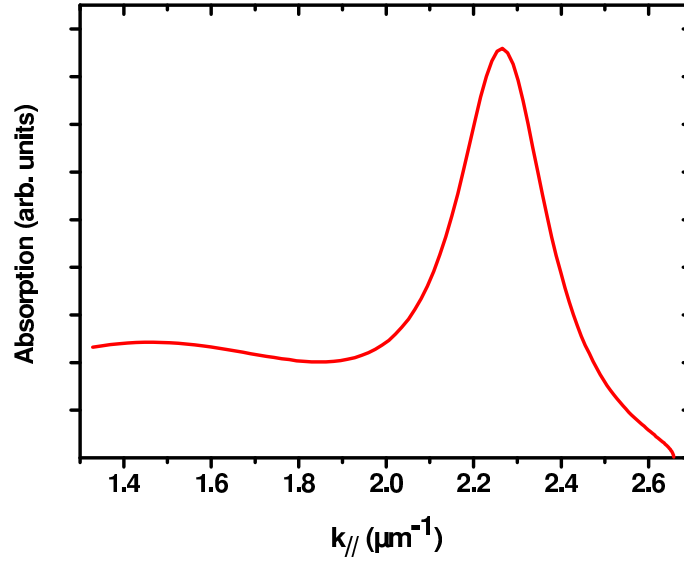
Figure 2.10: Simulated absorption intensity as a function of the inplane wave vector at $E = 160 meV$ for the sample without top metallic mirror.

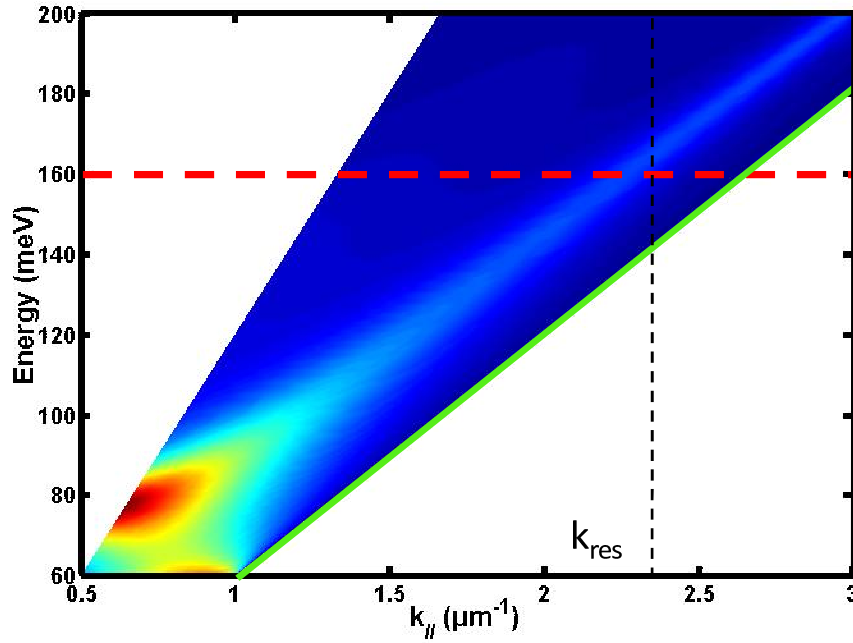Figure 2.11: Left panel: contour plot of the simulated polariton dispersion as a function of the inplane wave vector for the sample with the top metallic mirror taking into account the contribution of the intersubband transition. The green line corresponds to the light line and the vertical red (black) dashed line corresponds to k_{res} (k_{exc}). Right panel: simulated spectrum at $k_{res} = 2.5 \mu m^{-1}$ (red curve) and $k_{exc} = 1.9 \mu m^{-1}$ (black curve).
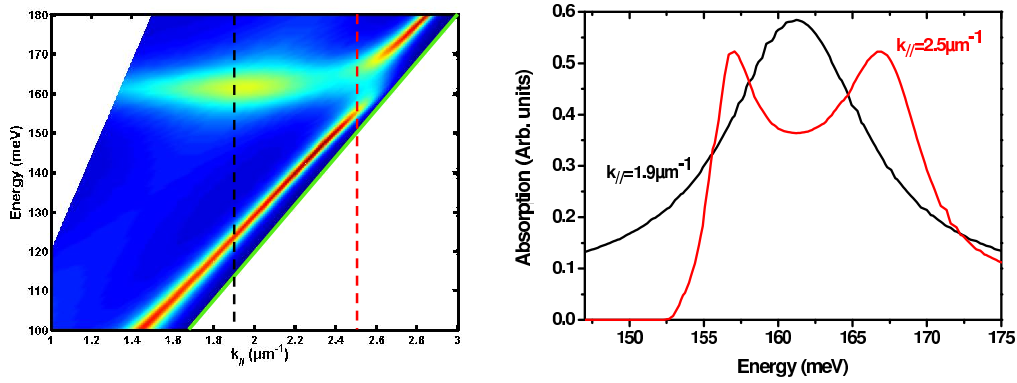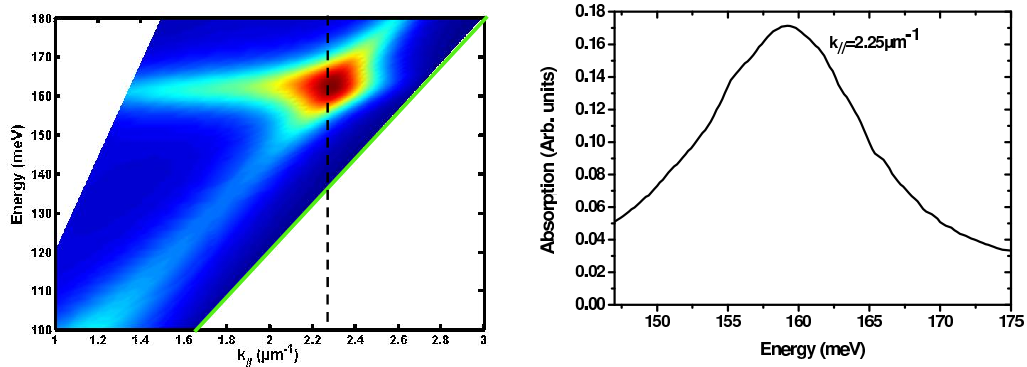
Figure 2.12: Left panel: contour plot of the simulated absorption dispersion as a function of the inplane wave vector for the sample without top metallic mirror taking into account the contribution of the intersubband transition. The green line corresponds to the light line and the vertical black dashed line corresponds to k_{res}. Right panel: simulated spectrum at k_{res}.

2.5 Experimental set up

The absorption spectrum of the device is obtained from transmission measurements. Figure 2.13 schemes the experimental setup. A globar (which is a silicon carbide thermal light that can be assimilated to a black body at about $470K$) is used as a MIR broad band source. Its beam goes through a FTIR (Fourier transform infrared spectrometer) and is then focused on the sample facet, collected and re-focused on a detector by the mean of ZnSe lenses. The diameter of the beam at the exit of the interferometer is of less than $2cm$. By using a lens with a focal distance of $10cm$, we obtain a solid angle for θ_{out} (which is the angle outside the sample) of about 10°. The detector is a photoconductive MCT (Mercury-Cadmium-Telluride) with a detectivity optimized at $\lambda = 10.3\mu m$.

The globar spectrum collected through this system without the sample is shown in figure 2.14. In our setup configuration, the energy window available for the measurement and the shape of the collected spectrum is determined by the wavelength dependance of the beam splitter (used in the FTIR) transmission, the detector working range and the different absorptions due to molecules present in the air (the system is not purged). To obtain the transmission through the device we measure the spectra with the sample and renormalize it with the spectra without the sample. To increase the contrast, we use a polarizer before the detection to only select the TM component of the globar beam as it is the only polarization susceptible to interact with the
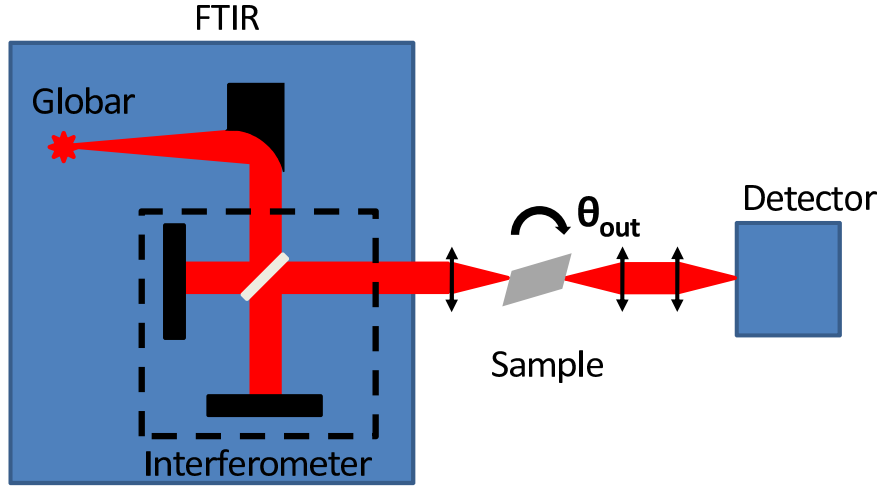
Figure 2.13: Scheme of the experimental set up for transmission measurement.

QCS and the cavity mode. The transmission spectra is thus given by

$$T = I_{TM}/I_{TM\,ref} \qquad (2.6)$$

where I_{TM} is the TM spectra with the sample and $I_{TM\,ref}$ the one without the sample.

In order to obtain the polaritonic dispersion we need to realize angle resolved measurements. To do so, we use a multi-pass geometry, as shown in figure 2.15. The bottom of the sample is mechanically polished to ensure a good reflectivity of the beam and both facets are polished with an angle θ_{pol} with respect to the substrate. Thanks to equation (2.5) it is possible to express the angle of propagation of the light in the substrate as a function of the sample parameters defined in figure 2.15:

$$\theta = \theta_{pol} + \arcsin\frac{\sin\theta_{out}}{n_{sub}} = \theta_{pol} + \theta_{in} \qquad (2.7)$$

where θ_{out} is the external angle compared to the direction normal to the facet and n_{sub} is the substrate optical index (here the substrate is undoped GaAs and $\lambda \approx 10\mu m$ so $n_{sub} \approx 3.3$).

By varying θ_{out} from -90° to 90° the light propagation angle inside the sample θ can be varied in the interval $[\theta_{pol} - 18°\ \ \theta_{pol} + 18°]$. It is therefore important to correctly choose the polishing angle θ_{pol} to be able to reach the desired angles θ in the substrate. In our system, the intersubband transition energy and the cavity mode are at resonance for an internal angle of about 72°; θ_{pol} is thus chosen to be 70° to investigate the region around the resonance.
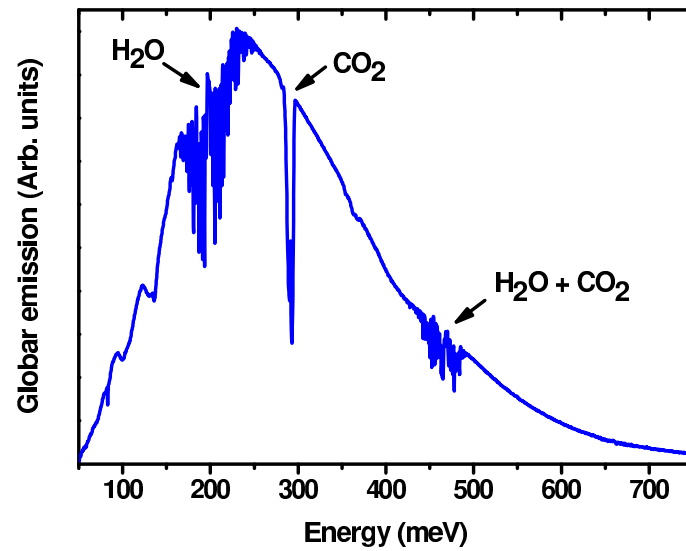
Figure 2.14: Measured emission spectra of the Globar through the transmission set up without sample. The absorption due to H_2O and CO_2 are pinpointed.
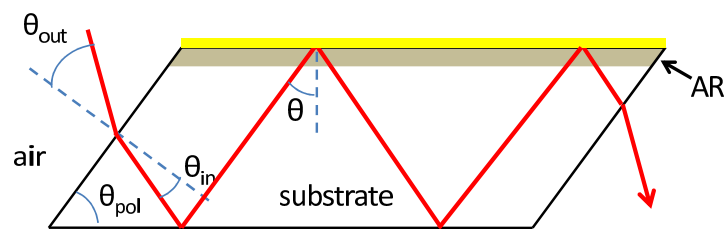

Figure 2.15: Scheme of the multi pass geometry for the sample in transmission measurements.

2.6   Absorption measurements: strong coupling

As described in section 2.2 the QCS is Si doped ($3.10^{17}cm^{-3}$) and at zero bias only the first subband of the main QW is occupied. It is thus possible to measure absorption in the unbiased device and to probe the coupling with the cavity mode by changing the angle θ.

We experimentally obtain the reflectivity at the $Al_{0.95\%}Ga_{0.05\%}As/GaAs_{sub}$ interface R by renormalizing the spectra collected after the sample by the spectra collected without the sample, following formula 2.6.

The bare intersubband absorption is measured by choosing an angle for which the cavity mode is out of resonance. According to figure 2.7 this condition is well satisfied for $\theta < 60°$. Figure 2.16 presents the absorption spectrum (blue curve) for $\theta = 54.1°$, where the intersubband transition energy appears at $161meV$ and the cavity mode energy is below $100meV$ (below our MCT detection limit). The intersubband peak can be well fitted by a Gaussian function (black dashed curve) centered at $160.4meV$ and with a FWHM of $8meV$. The broadening of the transition is attributed to interface roughness scattering and doping impurities.
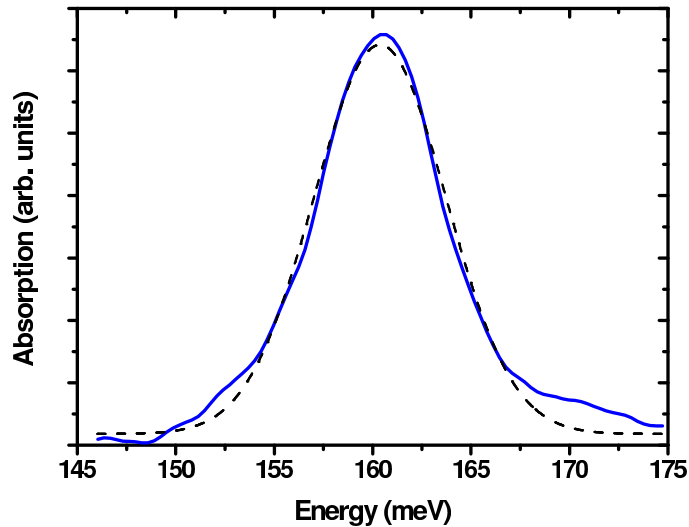
Figure 2.16: Absorption spectra for $\theta = 54.1°$ measured at $77K$ (blue curve). The black dashed line represents the fit with a Gaussian.

To investigate the light-matter coupling in the sample, we realize angle resolved measurements for $54.1°< \theta <76.5°$. Figure 2.17 summarizes absorption spectra obtained for the different internal angles at $77K$. For a good visualization of the polaritonic energy dispersion, they are normalized to the maximum

absorption value of each spectrum. They are arbitrarily shifted in the y axis and two dashed curves are guides for the eye to show the dispersion. Two absorption peaks are clearly visible, whose energy position and width changes with the internal angle. A clear anti-crossing appears, experimental signature of the strong coupling regime.
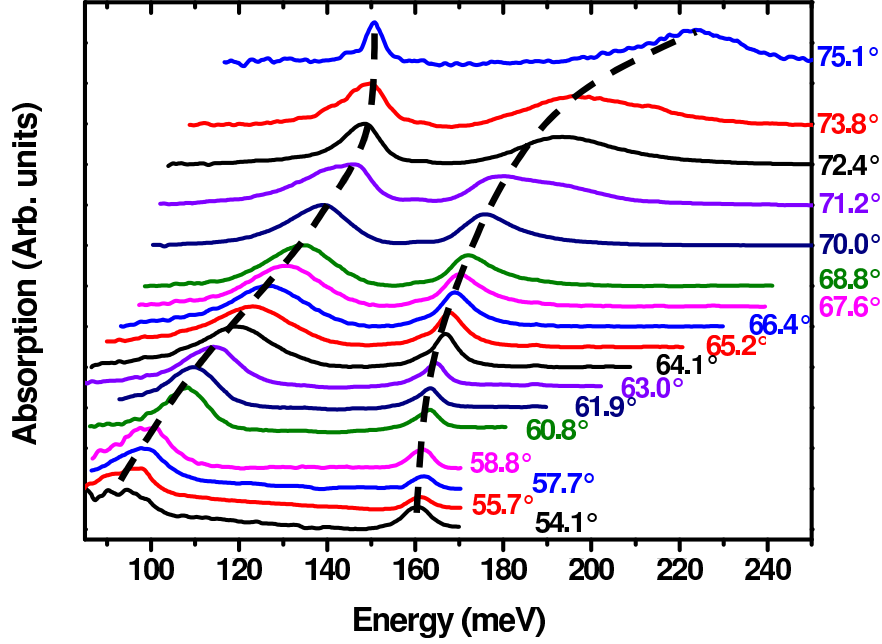
Figure 2.17: Absorption spectra for different angles θ measured at $77K$. They are arbitrarily shifted and dashed black curves underline the two peak positions for better clarity.

Using formula (2.3) it is possible to transpose all those spectra in the k space as shown in figure 2.18. This graph represents the absorption intensity in color scale as a function of the energy E and the inplane wave vector $k_{/\!/}$. Spectra have been measured with a resolution of approximately 2° for θ_{out} to follow the polaritonic dispersion evolution with a good precision (more than 35 spectra are taken to plot the k space). We clearly see the two polariton branches expected from chapter 1 with a Rabi splitting of $13meV$ at $k_{/\!/} = k_{res}$.

In the corresponding simulation (see figure 2.11), the difference of electron density between the ground and excited states of the intersubband transition $(N_1 - N_2)$ is the only adjustable parameter to correctly fit the experimental splitting between the polariton branches. The best correspondence is reached for $N_1 - N_2 = 6.10^{11}cm^{-2}$ which is very close to the nominal value $N_1 - N_2 = 7.10^{11}cm^{-2}$. The calculated Fermi energy is only $\approx 10meV$ above the

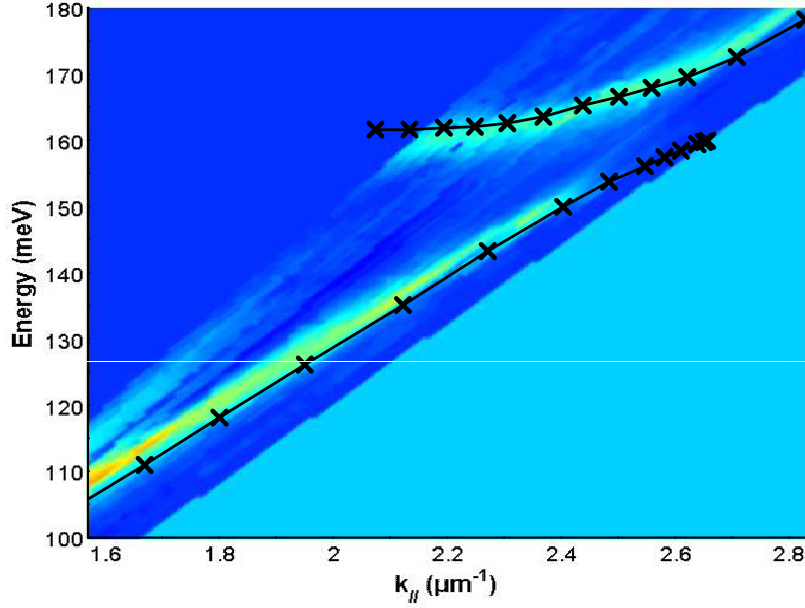Figure 2.18: Contour plot of the absorption spectra measured at $77K$. The black crosses represent the energy position of the absorption peaks obtained from the simulations ploted in 2.11

fundamental state and the measurement are taken at $77K$. In this case N_2 is totally negligible as it is more than 10 orders of magnitude lower than the electronic density on the fundamental state. A systematic correction on the angles of $0.7°$ is used to obtain the dispersion at the same $k_{/\!/}$ as the experiment. This correction is very reasonable considering the uncertainty on the polishing angle and on the reference angle position of the device during the experiment. The energy position of the absorption peaks obtained from the simulations are reported with black crosses in figure 2.18 and show a good agreement with the experience.

Figure 2.19 represents the energy difference between the two measured polariton branches as a function of θ. The minimum is reached for $\theta_{min} \approx 71°$ and its value is $35 meV$. This value has been for a long time erroneously taken as the Rabi splitting in intersubband polariton literature [Dini et al., 2003, Sapienza et al., 2007]. However, the correct splitting is obtained when considering the energy dispersion as a function of the inplane wave vector. Figure 2.20 shows the splitting between the polaritonic branches as a function of $k_{/\!/}$. The minimum is obtained for $k_{res} \approx 2.5 \mu m^{-1}$ and is of $13 meV$. This value corresponds to the correct Rabi splitting $2\hbar\Omega_R$. In figure 2.21 we report in the schematized polaritonic k space the energy positions of

the two absorption peaks measured at $\theta = \theta_{min}$ marked with triangles and at $k_{/\!/} = k_{res}$ marked with squares. This graph allows a clear visualization of the origin of the difference between the values of the splitting.
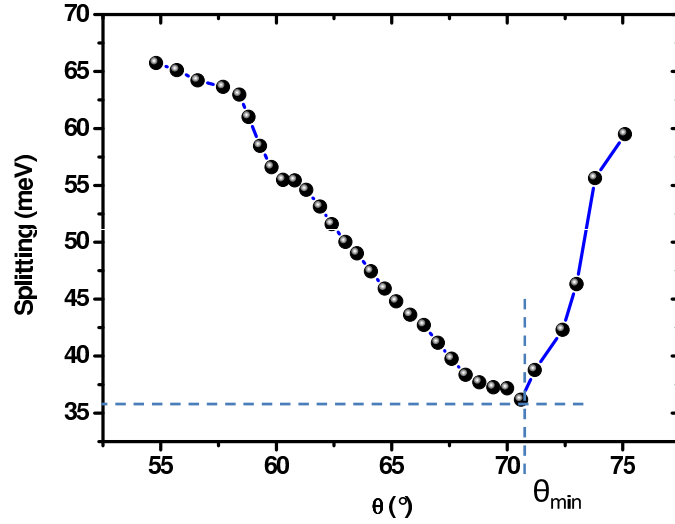
Figure 2.19: Experimental energy difference between the two polariton states as a function of the internal angle θ at $77K$.
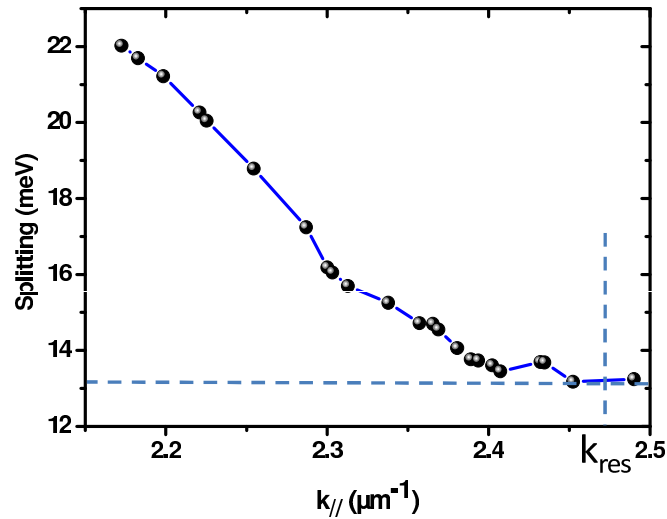
Figure 2.20: Experimental energy difference between the two polariton states as a function of the inplane wave vector $k_{/\!/}$ at $77K$.
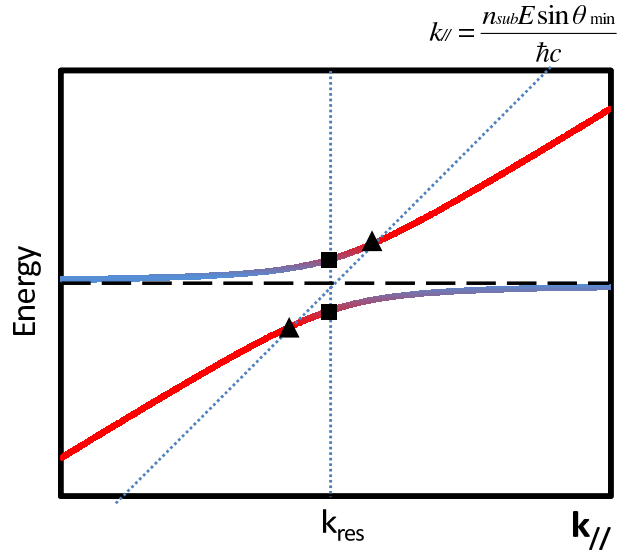
Figure 2.21: Schematic representation of the polaritonic dispersion as a function of the inplane wave vector. The black dashed line is the intersubband transition energy; the black triangles show the position of the polariton states at θ_{min}; the black squares show the energy positions of the polariton states at k_{res}.

2.7   Conclusion

To conclude, I presented in this chapter the description and the passive characterization of the electroluminescent device working in the strong coupling regime. After a brief description of the samples, I introduced the cavity dispersion and the k space as the correct representation for the polariton splitting. The experimental setup and the sample geometry has been shown before presenting our simulations and the experimental results. A Rabi splitting of 13meV is measured in the unbiased device.

The study of electroluminescence from the polaritonic states is presented in the next chapter.

Chapter 3

Resonant electrical injection in the polariton states

Contents

3.1 Electrical injection in polaritons

As mentioned in the introduction, the interest of an electroluminescent device based on intersubband polariton is to reduce the characteristic lifetime for the photons emission. Indeed, the spontaneous emission in the MIR is characterized by an extremely long lifetime when compared to the non-radiative processes. As an example we plot in figure 3.1 the radiative spontaneous emission lifetime (black curve) and the LO-phonon emission lifetime (red curve) as a function of the energy in a $GaAs/Al_{0.45}Ga_{0.55}As$ QW. While the radiative lifetime is of the order of $1\mu s$, the phonon emission lifetime is of the order of $1ps$ giving a typical quantum efficiency of the order of 10^{-6} in the MIR.
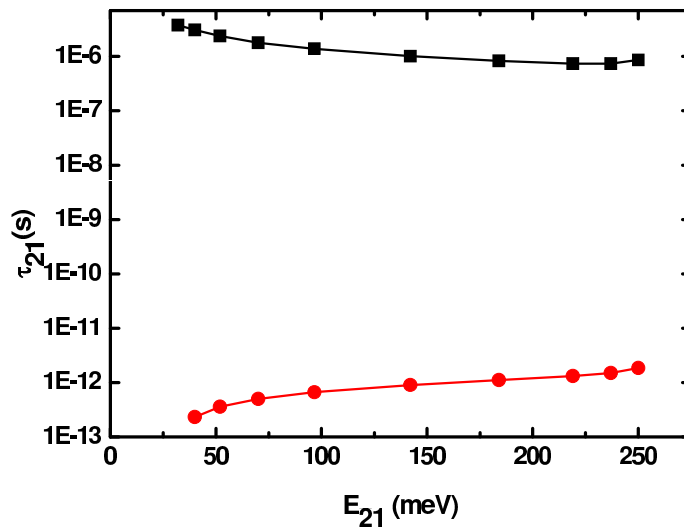
Figure 3.1: Calculated lifetime for the spontaneous emission (black curve) and the phonon emission (red curve) as a function of the energy in a $GaAs/Al_{0.45}Ga_{0.55}As$ QW.

In the strong coupling regime, the radiative spontaneous emission is a reversible process (Rabi oscillations). A new characteristic time is thus introduced in the system, proportional to $1/\Omega_R$. In the MIR, it is expected to be of the order of $1ps$ which would increase drastically the quantum efficiency.

The first step for realizing electroluminescent (EL) devices operating in the strong coupling regime was to prove the compatibility of the strong coupling regime with electrical contacts and electric current in the structure. This has been demonstrated in [Dupont et al., 2003] where photocurrent measurements were performed on a multiple QW structure inserted in a microcavity. The compatibility with a quantum cascade structure (QCS) was demonstrated

later with photovoltaic measurements [Sapienza et al., 2007] to probe the polariton states.

The first EL device based on ISB polaritons was published in [Sapienza et al., 2008] using a $GaAs/Al_{0.45}Ga_{0.55}As$ quantum cascade structure. In this reference, electroluminescence from the polariton states was demonstrated up to room temperature. In this system, the electroluminescence at a given voltage presents an emission following the polaritons dispersion but on a narrow energy window. As it will be explained later, this effect is attributed to the resonant electrical injection in the polariton states. The energy window is determined by the energy distribution of the electrons on the state of the QCS responsible of the injection in the polaritons.

The theoretical description of the EL from ISB polaritons is a complex problem because the subbands are coupled not only to the radiation but also to the injection and extraction minibands of the QCS. This problem has been addressed recently in several publications (see, for example [De Liberato and Ciuti, 2009a], and references therein), following different approaches. The first attempt to calculate the electroluminescence spectrum from an intersubband polariton device has been proposed in [Ciuti and Carusotto, 2006]. In this paper, the authors describe the input-output dynamics of an optical cavity in the light-matter ultra-strong coupling regime. They consider the case of an intersubband excitation in a cavity coupled to two bosonic dissipative baths, for the photon field and for the electronic excitation. Within this model, the authors derive an analytical expression for the EL spectrum, which is proportional to a term accounting for the spectral shape of the electronic reservoir.

In the previous chapter we demonstrated the strong coupling regime by absorption measurements. Here we present electroluminescence (EL) spectra on the same device. The first part of the chapter will focus on the fabrication process and experimental setup necessary for electroluminescence measurement. The two devices presented in chapter 2 will be studied. These are based on the same quantum cascade structure but with a different photonic confinement. Angle resolved EL spectra under a constant applied voltage for both samples will be presented to understand the peculiar features of the strong coupling regime under electrical injection. Then, I will present our model to simulate the EL spectra. Finally a study at different voltages will be detailed. I will show that the electroluminescence peak is strongly tunable with the applied voltage in the polaritonic device. The results presented in this chapter are the object of two publications [Todorov et al., 2008], [Jouy et al., 2010].

3.2   Fabrication process & experimental setup

In order to inject electrons in the QCS we need to have electrical contacts both on top and at the bottom of the active region (AR). To this end we realize mesa devices as schematized in figure 3.2. The facet is polished with an angle $\theta_{pol} = 70°$. The top $103nm$ thick doped $GaAs$ layer is needed to obtain an homogenous injection of the current on the entire mesa surface. The $560nm$ thick doped $GaAs$ layer on the other side is used both for the optical confinement as a low refractive index layer and for the extraction of the current through a contact on the side of the mesa.
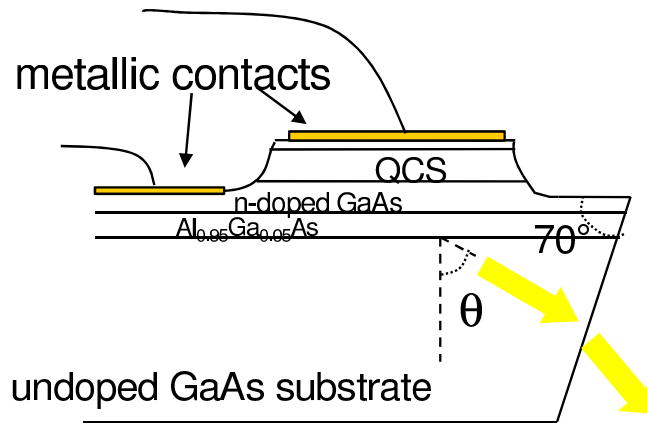
Figure 3.2: Scheme of the device for electroluminescence measurements.

Figure 3.3 describes the different steps for the samples processing. First, a photo-sensitive resist is deposited on the wafer to realize by an optical lithography circles of resist with a diameter of $200\mu m$. A $H_2SO_4/H_2O_2/H_2O$ solution with respective volumic proportions of 1 / 8 / 80 is used to chemically etch the $GaAs/AlGaAs$ active region not protected by the resist. The etch speed is of about $0.8nm$/minute and a Dektak profilometer permits to measure regularly the thickness etched in order to stop in the $560nm$ doped $GaAs$ layer. A second optical lithography allows to define the surfaces on top of the mesa and at the bottom of the mesa where the metal will be deposited. The metal is $Ni(10nm)/Ge(60nm)/Au(120nm)/Ni(20nm)/Au(200nm)$, annealed at $350° C$. Annealing is used to diffuse the Ge in the top ($103nm$ thick) and the bottom ($560nm$) doped $GaAs$ layers in order to obtain ohmic contacts. The electric contact is realized thanks to gold micro-wires with a diameter of $25\mu m$ by means of wire bonding.
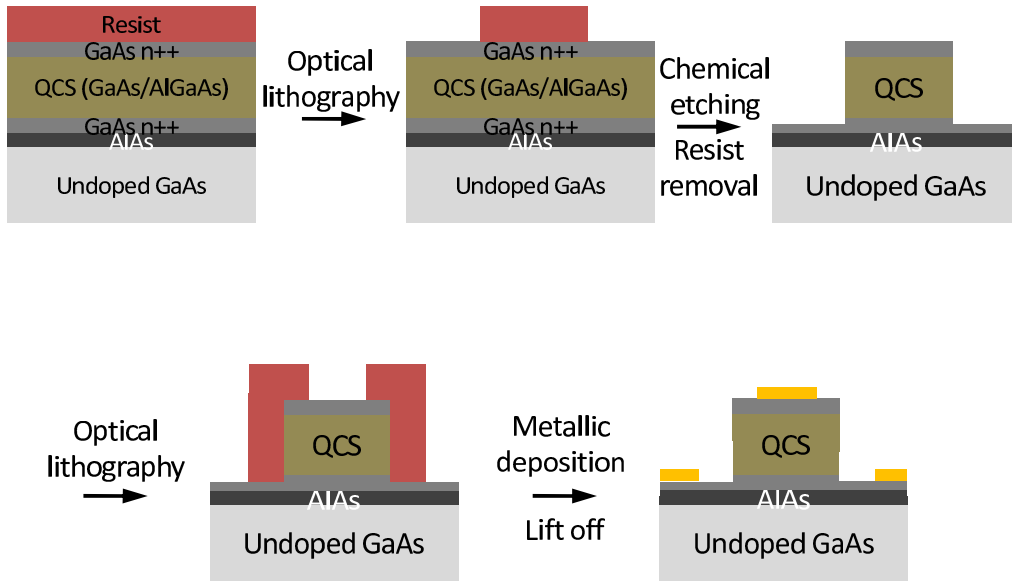
Figure 3.3: Scheme of the different steps for the sample processing.

This technique is used to realize two devices. Figure 3.4 presents an optical microscope picture from the top of the sample where two mesa devices are visible. In the left one the top metallic contact has a surface approximately equal to that of the mesa. This top contact is also the top mirror of our cavity, as discussed in chapter 2. In the device on the right, the disk of metal deposited on top has a diameter of only $50\mu m$ (about 6% of the mesa surface). In this case the electrical injection is still possible but the top metallic mirror is absent. The cavity mode is in this case like the one shown in figure 2.9. The device can thus be considered as a weak coupling reference of that on the left.

Figure 3.5 represents a scheme of the experimental setup used for EL measurements. The sample is Indium soldered on a copper holder, mounted on a cryostat cold finger and connected to BNC cables for the electrical injection. The emitted light is collected with a $ZnSe$ lens of focal distance $10cm$ and passes through the FTIR before being detected by the MCT. Because the signal obtained is very small, the sample is operated in a pulsed mode permitting a lock-in detection. This allows to get rid of the constant noise signal coming from the MIR radiations emitted in the environment surrounding the experience by subtracting the non modulated to the modulated signal.
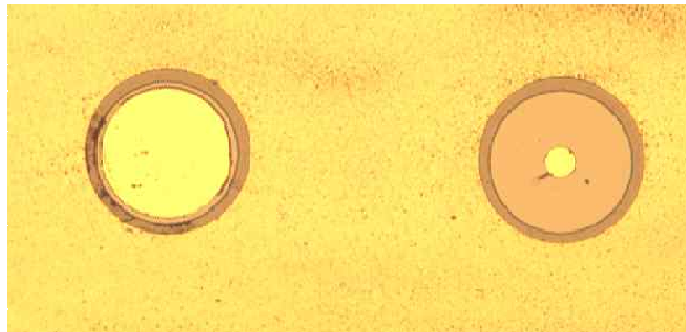
Figure 3.4: Optical microscope picture of the top of the sample. The left mesa is fully recovered with gold (polaritonic device) while the right one is only partially covered (reference device).

Figure 3.5: Scheme of the set up for electroluminescence measurements.

3.3 Electroluminescence spectra at fixed voltage

In this section, I will present electroluminescence measurements realized for a fixed applied voltage on both devices.

3.3.1 Electrical characteristics

In order to obtain the electrical characteristics of the sample, we measure the voltage applied on the device (directly on an oscilloscope) as a function of 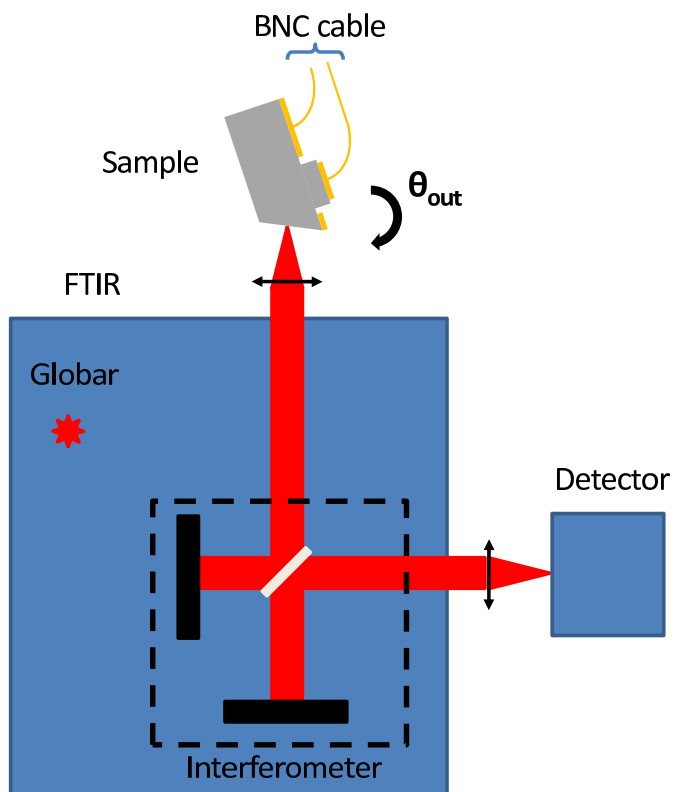the current (using a current probe). The current-voltage ($V(I)$) characteristics is shown in figure 3.6 with blue dots. As for most QCS it can be divided in two main parts: in the green area (for $0mA < I < 90mA$) the voltage rises very fast compared to the current and the curve slope drastically changes, while in the red area (above $90mA$) the voltage increases slowly and linearly with the current. It can easily be explained by considering the relative position of the injector compared to the excited state of the main quantum well (see band diagram in figure 2.2). At $0V$ the injector is not aligned with the excited state and therefore electrons cannot tunnel (this is equivalent to a high resistivity traduced in the $V(I)$ curve by a steep slope). As we increase the voltage, the injector gets closer to the excited state (green zone) and facilitates the tunneling until it reaches the resonant tunneling condition which gives the most efficient injection. Increasing the voltage further only increases linearly the current (red zone) because the injector is "locked" at resonance with the excited state as it is the configuration which minimizes the global resistance of the QCS. The linear regime is pinpointed by the black continuous line.

3.3.2 Injector characteristics

We first realized angle resolved EL measurements before alignment with an applied voltage of $4.5V$ and a current of $14mA$ (black star on the current-voltage curve in figure 3.6) for both the polaritonic and the reference device. The left panel of figure 3.7 represents the EL spectrum at two angles ($\theta = 56.6°$ and $\theta = 71.8°$) for the sample without the top metallic mirror, operating in the weak coupling regime. For clarity, the maximum peak of both spectra is normalized to the same value. In this case, the two spectra are similar and their shape corresponds to the typical spectrum obtained for a QCS before alignment [Benveniste et al., 2008]. Under this bias configuration two contributions can be identified: a main peak centered at E_{21} and a tail at lower energy (E_{inj}) corresponding to the diagonal transition from the injector directly to the fundamental state of the well (labeled 1). We can therefore
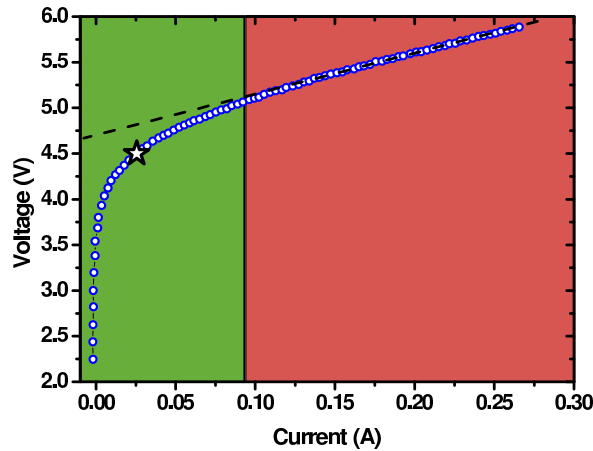
Figure 3.6: The blue dots correspond to the current-voltage characteristic of the sample measured at $77K$. The colored regions represents the different regimes present in the sample; the green is before alignment and the red is after alignment of the QCS. The black line shows the linear dependance of the current as a function of the current in the red zone and the black star pinpoints the position for $4.5V$.

extract the injector characteristics directly from the weak coupling spectra. On the other hand, the right panel of figure 3.7 represents the EL spectrum obtained for the polaritonic device with the top metallic mirror at $\theta_{res} = 71.8°$ (red squares) and far from θ_{res} ($\theta = 52.4°$; in blue dots) using the same normalization as in the left panel. These angles correspond to the two different resonance conditions: at $52.4°$ the excited cavity mode is weakly coupled with the intersubband transition. At $71.8°$ the fundamental cavity mode is strongly coupled with the intersubband transition giving rise to polaritonic states. In this second case, the maximum of the spectrum appears at the energy of the injector instead of that of the intersubband transition. The spectra at $71.8°$ for the reference and polaritonic sample are directly compared in the bottom panel of figure 3.7 and clearly shows an extra feature appearing for the polariton sample at low energy. One can notice that the spectra at low angle for the reference and the polaritonic sample are approximately the same which confirms the weak coupling to the excited cavity mode for the low angles of the polaritonic sample. It is thus possible to deduce the injector energy dispersion within the same mesa where the strong coupling is measured by only choosing the appropriate angle. This technique ensures the exact same voltage and current conditions for the polaritonic and the weakly coupled spectra. In figure 3.8 the spectra for $\theta = 52.4°$ of the sample with the top mirror (black squares)

is well fitted (red continuous line) by a sum of two gaussians (dashed black lines). The one corresponding to the injector is peaked at $E_{inj} = 151.6 meV$ with a FWHM of $\sigma_{inj} = 10 meV$ and the one corresponding to the intersubband transition is set to be $E_{21} = 161 meV$ and $\sigma_{21} = 9 meV$ as deduced from the passive characterization of the sample discussed in chapter 2.
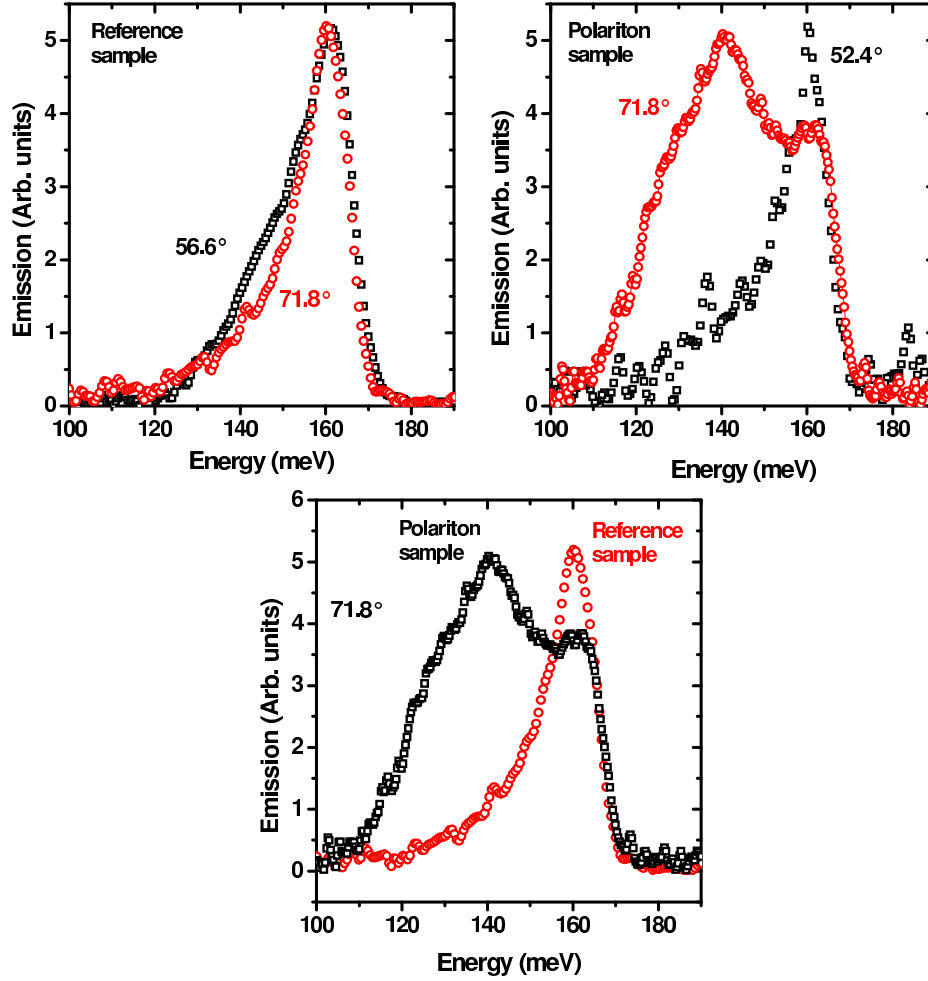
Figure 3.7: **Left panel**: measured electroluminescence spectra for the reference sample at $77K$, with an applied voltage of $4.5V$ for $\theta = 56.6°$ (black squares) and $\theta = 71.8°$ (red dots). **Right panel**: measured electroluminescence spectra for the polaritonic sample at $77K$, with an applied voltage of $4.5V$ for $\theta = 52.4°$ (black squares) and $\theta = 71.8°$ (red dots). **Bottom panel**: comparison between the EL spectra at 71.8° from the reference sample (red dots) and the polaritonic device (black squares). Note the extra feature appearing at low energy for the polaritonic device.
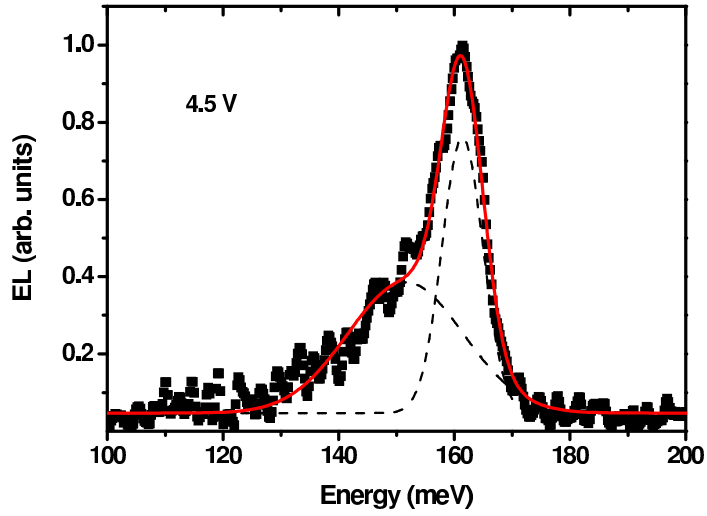
Figure 3.8: The black dots represents the electroluminescent spectra from the polaritonic sample at $77K$ for an angle $\theta = 57.9°$ and a bias voltage of $4.5V$. The red curve corresponds to the fit with a sum of two gaussians functions (black dashed lines).

3.3.3 Electroluminescence spectra in the k space

In order to obtain the k space for both samples thanks to equation 2.3, we measure the EL spectra for about 40 different angles with the same applied voltage of $4.5V$. Figure 3.9 show the k spaces for the sample with (left panel) and without (right panel) the top metallic mirror. As one can notice, the two dispersions are very different. In the polaritonic device two contributions appear. The main one comes from the strong coupling and follows the lower polariton branch dispersion centered around $150meV$. Therefore, there is no intensity at the intersubband transition energy for k_{res} due to the Rabi splitting at resonance. The second contribution is at the intersubband transition energy and corresponds to its weak coupling with the excited cavity mode discussed in figure 2.7. Indeed, thanks to the width of the excited cavity mode, we can see the weak coupling even at higher inplane wave vector than k_{exc}. This gives rise to an EL signal centered at the intersubband transition energy with a tail at lower energy. For the reference device, only one contribution appears corresponding to the weak coupling of the intersubband transition with the broad cavity mode appearing at k_{res} described in figure 2.9. The comparison of those two k spaces clearly shows that the strong coupling regime allows to obtain EL at energies otherwise inaccessible. In comparison to the

k space obtained for the absorption in the previous chapter (figure 2.11), we can underline that the polaritonic EL is limited to a narrower energy window (from $110meV$ to $170meV$).
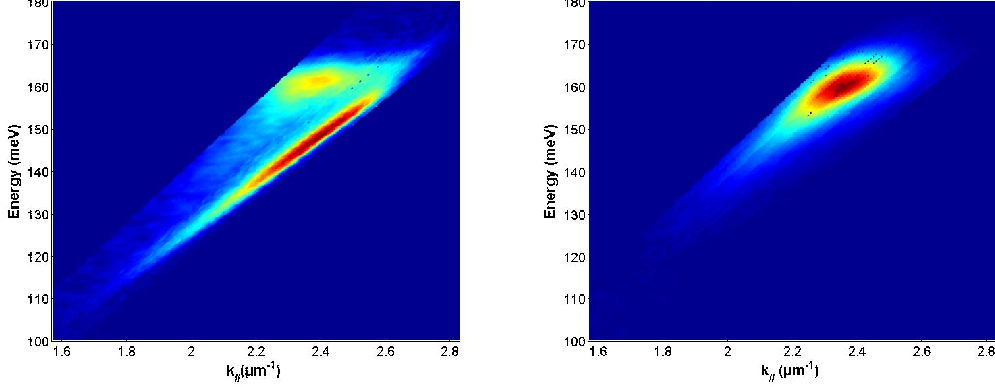
Figure 3.9: Contour plot of the electroluminescence from the reference device measured at $77K$ as a function of the inplane wave vector and of the energy for an applied voltage of $4.5V$ on the polaritonic (left panel) and the reference (right panel) sample.

3.4 Simulations of the electroluminescence spectra at fixed voltage

The data presented in the previous section show that EL spectra follow the lower polariton dispersion in a limited energy window. The spectrum also strongly depends on the internal angle. Therefore, several elements have to be taken into account to simulate the data. Geometric factor will be studied in paragraph 3.4.1 with a sample not designed to display the strong coupling regime. Section 3.4.2 will present the influence of the photonic density of states and of the AR on the spectra.

3.4.1 Fresnel coefficients

In order to realize the simulations corresponding to the experimental EL k spaces, we first need to take into account the geometry of the samples. We realized angle resolved measurement on a $GaAs$ EL device realized by Elsa Benveniste in our laboratory [Benveniste et al., 2009] with the same shape ($200\mu m$ ∅ mesa) as our samples to determine the correct transmission coefficients. This device is based on an active region very similar to that of our

device, but the sample is not designed to display the strong coupling regime. Angle resolved EL measurements on this sample allows us to determine the angular dependance of the EL intensity inherent to the mesa geometry used for our devices. Figure 3.10 shows the integrated intensity of the EL spectra as a function of the internal angle for $\theta_{pol} = 60°$ (black squares) and $\theta_{pol} = 70°$ (blue triangles) where θ_{pol} is the polishing angle. The curves present a maximum of intensity respectively around 58.5° and 62°. This behavior is very different from the integrated EL intensity from a dipole in free space, which is expected to vary as $\sin^2 \theta$ [Landau and Lifchits, 1994] as represented on the figure 3.11 with a black curve. In order to calculate the expected EL intensity from a dipole in the multilayer structure of the device, we use the transfer matrix simulation and obtain the red curve. Even if this simulation gives an angular dependance closer to the experimental one, we need to take into account the Fresnel reflection coefficients at the polished facet to reproduce correctly the intensity dependance of the polishing angle.
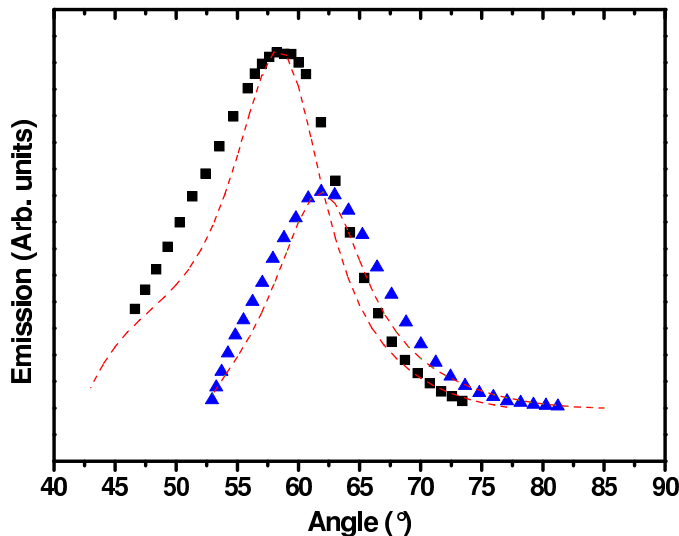
Figure 3.10: The black squares (blue triangles) represent the integrated electroluminescence of the device realized by Elsa Benveniste measured at $77K$ for an applied voltage of $4.5V$ for $\theta_{pol} = 60°$ ($\theta_{pol} = 70°$) as a function of θ. The red dashed lines are the corresponding simulations taking into account the geometry of the samples.

The intensity transmitted through the facet per unit angle $d\theta_{out}$ is obtained with

$$dI_{out} = TdI_{in} \qquad (3.1)$$
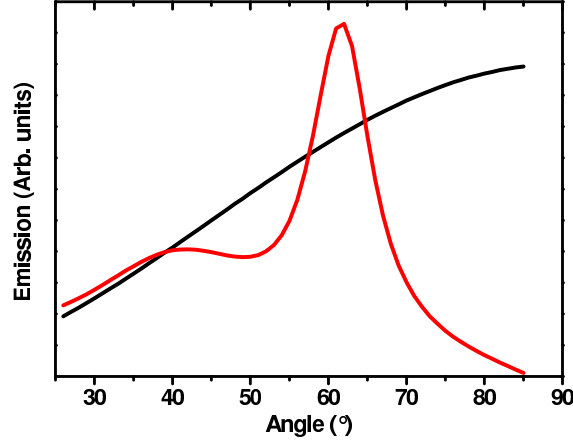
Figure 3.11: The black curve represent the function $\sin^2\theta$. The red curve is the integrated electroluminescence inside the substrate as a function of θ simulated by the transfer matrix formalism for an applied voltage of $4.5V$.

where I_{in} is the intensity in the sample and T is the Fresnel intensity transmission coefficient given by:

$$T = \frac{4n_{sub}\cos\theta_{out}\cos\theta_{in}}{(n_{sub}\cos\theta_{out}+\cos\theta_{in})^2} \tag{3.2}$$

Therefore we need to calculate the transmitted intensity per unit angle $dI_{out}/d\theta_{out}$. From equation 3.1, we deduce

$$\frac{dI_{out}}{d\theta_{out}} = T\frac{dI_{in}}{d\theta_{out}} = T\frac{dI_{in}}{d\theta_{in}}\frac{d\theta_{in}}{d\theta_{out}} \tag{3.3}$$

The Snell-Descartes equation gives $d\theta_{in}/d\theta_{out} = \cos\theta_{out}/(n\cos\theta_{in})$. As presented in reference [Lukosz and Kunz, 1977] and [Benisty et al., 1998], by replacing the terms in equation 3.3, we obtain that the collected power per unit angle depends on the emitted power per unit angle $(dI_{in}/d\theta_{in})$ as

$$\frac{dI_{out}}{d\theta_{out}} \propto \frac{\cos^2\theta_{out}}{(n_s\cos\theta_{out}+\cos\theta_{in})^2}\frac{dI_{in}}{d\theta_{in}} \tag{3.4}$$

To obtain the optical power collected by the detector, we need to multiply the emitted intensity per unit angle by the apparent surface of the facet in the direction of observation (which is proportional to $\cos\theta_{out}$) and by the projection of the surface of the mesa on the polished facet (which is proportional to $\cos\theta$). Using equation 3.4, $\cos^2+\sin^2=1$ and $\theta_{in}=\theta_{pol}-\theta$, the geometric term including the Fresnel coefficient finally becomes

$$F(\theta) \propto \frac{[1-n_s^2\sin^2(\theta_{pol}-\theta)]^{3/2}\cos\theta}{\{n_s[1-n_s^2\sin^2(\theta_{pol}-\theta)]^{1/2}+\cos(\theta_{pol}-\theta)\}^2} \tag{3.5}$$

Thanks to this correction we can reproduce the shape of the data with the transfer matrix simulation for both polishing angles (red curves in figure 3.10) with a systematic angle correction of -7° for $\theta_{pol} = 60°$ and -4° for $\theta_{pol} = 70°$. Once again, those correction on the angle are reasonable considering the experimental uncertainties. The fact that the corrections are different for the two polishing angles (and in the next section for the simulations of the polaritonic sample) comes both from the uncertainty on the polishing angle and on the experimental position of the 0° angle.

3.4.2   Simulated k space

To reproduce our experimental k space for the polaritonic sample, we now need to simulate the EL taking place inside our sample. Never the less, the theoretical description of the EL from intersubband polaritons is a complex problem because the subbands are coupled not only to the radiation but also to the injection and extraction minibands of the QCS. The EL spectra are simulated as the product of the photonic density of states and of the occupancy of the polariton branches, determined by the voltage applied to the device. The photonic density of states is given by the absorption spectrum $A_N(E)$ (in the strong coupling regime). The occupancy of the polariton states is described by a Gaussian function, centered at the energy corresponding to that of the injector. This description is analog to that of the photoluminescence from microcavity exciton polaritons [Stanley et al., 1996], [Weisbuch et al., 2000], [Houdré et al., 1994], [Houdré, 2005]. Indeed, it is described as the occupancy of the polariton states times the coupling out of such polaritons, i.e., the reverse process of incoupling of outside photons, given by the absorption coefficient. Taking into account the Fresnel coefficients $F(\theta)$ calculated above, the EL collected from our device is proportional to

$$L(E,\theta) \propto A_N(E,\theta) \times \exp{-\frac{(E - E_{inj})^2}{2\sigma_{inj}^2}} \times F(\theta) \qquad (3.6)$$

where $A_N(E,\theta)$ is the absorption spectrum at the angle θ (the index N reminds the dependance of this dispersion on the square root of the electronic population in the fundamental state for the polaritonic device), E_{inj} the injector energy compared to the ground state and σ_{inj} the FWHM of the gaussian corresponding to the injector.

The left panel of figure 3.12 is the simulated k space corresponding to the left panel of figure 3.9. It has been calculated by using equation 3.6. An electronic density of $4.10^{11} cm^{-2}$ is used to calculate the absorption and a correction of 5° is needed (this correction is still reasonable with the uncertainties

on the reference angle chosen during the measurements) to reproduce the experimental spectra. The parameters E_{inj} and σ_{inj} coming from the fit in figure 3.8 are slightly adjusted to respectively $150.5meV$ and $12meV$ to obtain the best correspondence with the data. In the left panel of figure 3.12 we can observe both the contributions at the intersubband transition energy at k_{exc} and that following the lower polaritonic branch at k_{res}. Those two features reproduce both the weak coupling with the excited cavity mode and the lower polariton branch contributions observed in the experimental spectra.
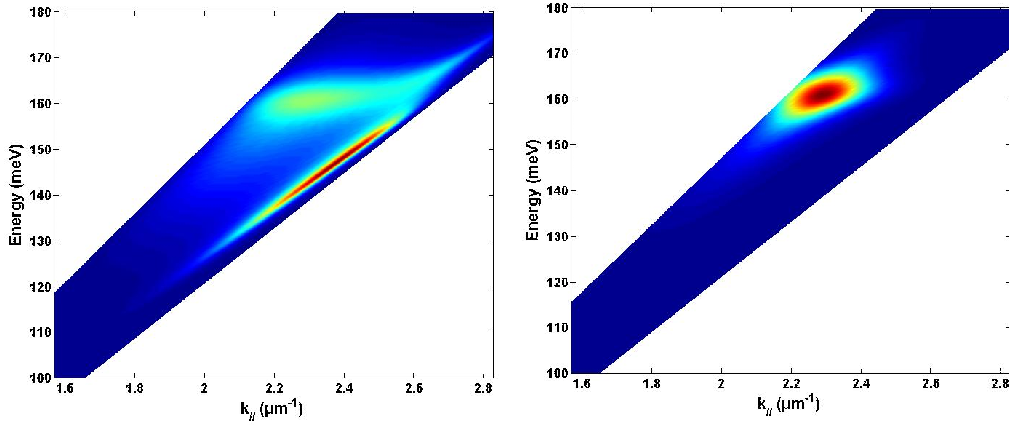
Figure 3.12: Contour plot of the simulated electroluminescence as a function of the inplane wave vector and of the energy for an applied voltage of $4.5V$ for the sample with (left panel) and without (right panel) the top gold mirror.

As a comparison, the right panel of figure 3.12 shows the simulated k space with the same parameters but for the sample without the top metallic mirror. Only one peak is visible at the intersubband transition energy for k_{res} with a low energy tail. This spectrum is in good agreement with the experimental one in the right panel of figure 3.9.

3.4.3 Electrical vs photonic resonant injection

Before concluding this section, I would like to compare the EL spectrum of the polaritonic device with the effect of an optical pump on a medium containing ISB polaritons.

Figure 3.13 shows the contour plot obtained by multiplying the bare EL spectrum EL_{bare} (obtained far from resonance at 57.9°) and the polaritonic absorption dispersion and the Fresnel term $F(\theta)$. It corresponds to the equation:

$$L(E, \theta) \propto A_N(E, \theta) \times EL_{bare} \times F(\theta) \qquad (3.7)$$

Here the energy window for the injection in the polariton states is given by the sum of the Gaussians corresponding to the diagonal transition from the injector to the fundamental state and of the Gaussian corresponding to the ISB transition (as shown in figure 3.8 $EL_{bare} = \alpha \exp -(E - E_{inj})^2/2\sigma_{inj}^2 + \beta \exp -(E - E_{21})^2/2\sigma_{21}^2$, where α and β are coefficient that depend on the voltage applied). Two contributions are vis-
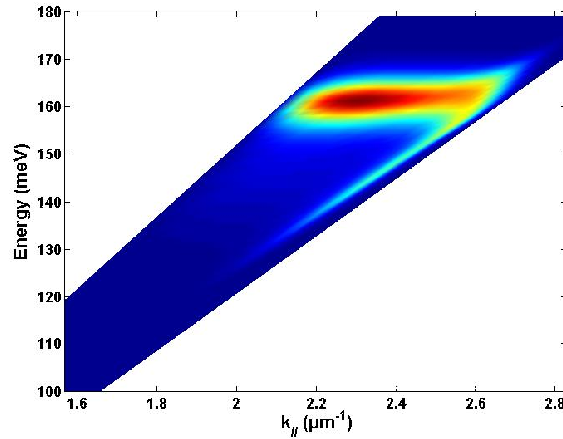
Figure 3.13: Contour plot of the simulated electroluminescence with photonic injection process into the polariton states as a function of the inplane wave vector and of the energy for an applied voltage of $4.5V$.

ible: a main peak at the intersubband transition energy centered at k_{exc} and a much smaller contribution following the lower branch dispersion around k_{res}. In this case the main contribution comes from the weak coupling with the excited cavity mode. The simulations realized so far were based on a resonant injection of the electrons from the injector (corresponding to the Gaussian centered at the injector energy) directly in the polaritonic states as schemed in figure 3.14. On the contrary, in this case the main contribution comes from the strong coupling with the fundamental cavity mode. This simulation would correspond to an optical pumping of the polariton states by an internal emitter; as schemed in figure 3.15 the light emitted from the QCS EL_{bare} (corresponding to the sum of the ISB transition (dashed blue line) and the diagonal transition (red dashed line)) would populate the polaritonic dispersion.

By comparing figure 3.12 and 3.13 to the experimental spectrum it clearly appears that the first one is in better correspondence. It thus proves that the EL spectra of our sample is due to the resonant injection of electrons from the injector into the polariton states and not due to the injection of photons

emitted within the QCS into the polaritonic states. An example of this kind of device will be presented in the appendix.
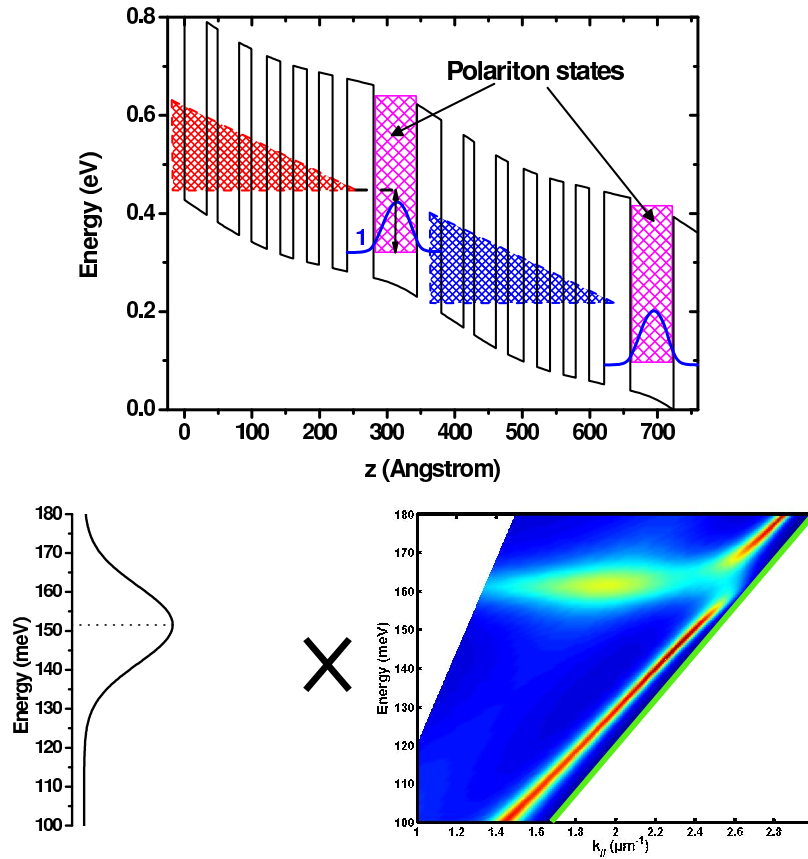
Figure 3.14: Top panel: band diagram showing the direct injection of electrons in the polariton states. Bottom panel: the simulation presented in figure 3.12 is the product of the injector energy dispersion deduced from figure 3.8 times the absorption simulation (including the Fresnel coefficients).

Figure 3.15: Top panel: band diagram showing the two contributions E_{21} and E_{inj} in the bare EL. Bottom panel: the simulation presented in figure 3.13 is the product of th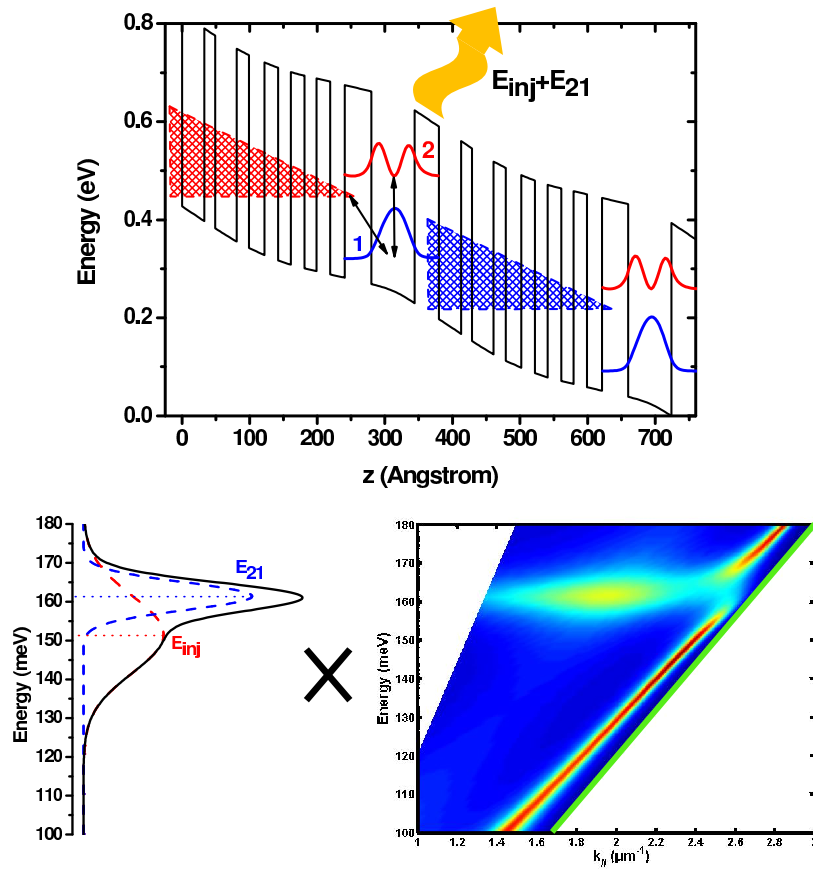e bare EL spectra (with the contributions of the ISB E_{21} and the diagonal transition E_{inj}) times the absorption simulation (including the Fresnel coefficients).

3.5 Voltage dependance of the electroluminescence spectra

3.5.1 Experimental EL spectra at different voltages

In order to study the dependance of the EL as a function of the applied voltage, we realized angle resolved measurements for different positions on the current-voltage curve from figure 3.6. The six panels in figure 3.16 represent the experimental k space at $77K$ for the following electrical characteristics: $4V$ ($4.7mA$), $4.5V$ ($14mA$), $5V$ ($58mA$), $6V$ ($258mA$), $7.75V$ ($718mA$) and $13V$ ($2000mA$). Each one presents the two contributions due to the weak coupling with the excited cavity mode and to the lower polariton branch issued from the strong coupling with the cavity mode. Two effects are visible while increasing the voltage. The first is a transfer of the EL intensity between the lower polariton branch in favor of the spot weakly coupled, while increasing the voltage. The second effect is that the energy of the contribution from the lower polariton branch increases from $144meV$ at $4V$ to $160meV$ at $13V$ and the FWHM gets narrower for the highest voltages. This effect can be explained by the alignment conditions of the injector with the excited state of the intersubband transition. This is schematized on the right side of figure 3.16 where we represent the main quantum well (black line) with the fundamental and excited states (in blue) as well as the injector and extraction minibands (in red) for different voltages. As we move to higher voltages the energy between the injector and the fundamental state increases. Furthermore, at low voltage ($4V$ for example), the wave functions forming the injector miniband are poorly aligned because designed for a voltage of $6V$. In this condition, the miniband shape is no longer triangular as its wave functions involved in the electrical injection (i.e. close to the main well) appear at different energies, giving rise to a very broad injection. By increasing the voltage these wave functions become aligned and are tunnel coupled to the upper state of the radiative transition.

We summarize on figure 3.17, as a function of the inplane wave vector, the energy position of the maximum peak from the EL spectra measured at the different voltages (color dots). A series of two peaks appear for each voltages: one at low energy presenting an important dispersion and one constant at the ISB transition energy. The black curve and dots represent the position for the simulated absorption of the lower polariton branch corresponding to the black crosses in figure 2.18. As one can see, the low energy peaks position for the different voltages perfectly reproduce the lower polariton branch dispersion confirming its attribution to the emission from the polariton states. The contribution at the ISB energy corresponds on the contrary to the weak coupling to the excited cavity mode.
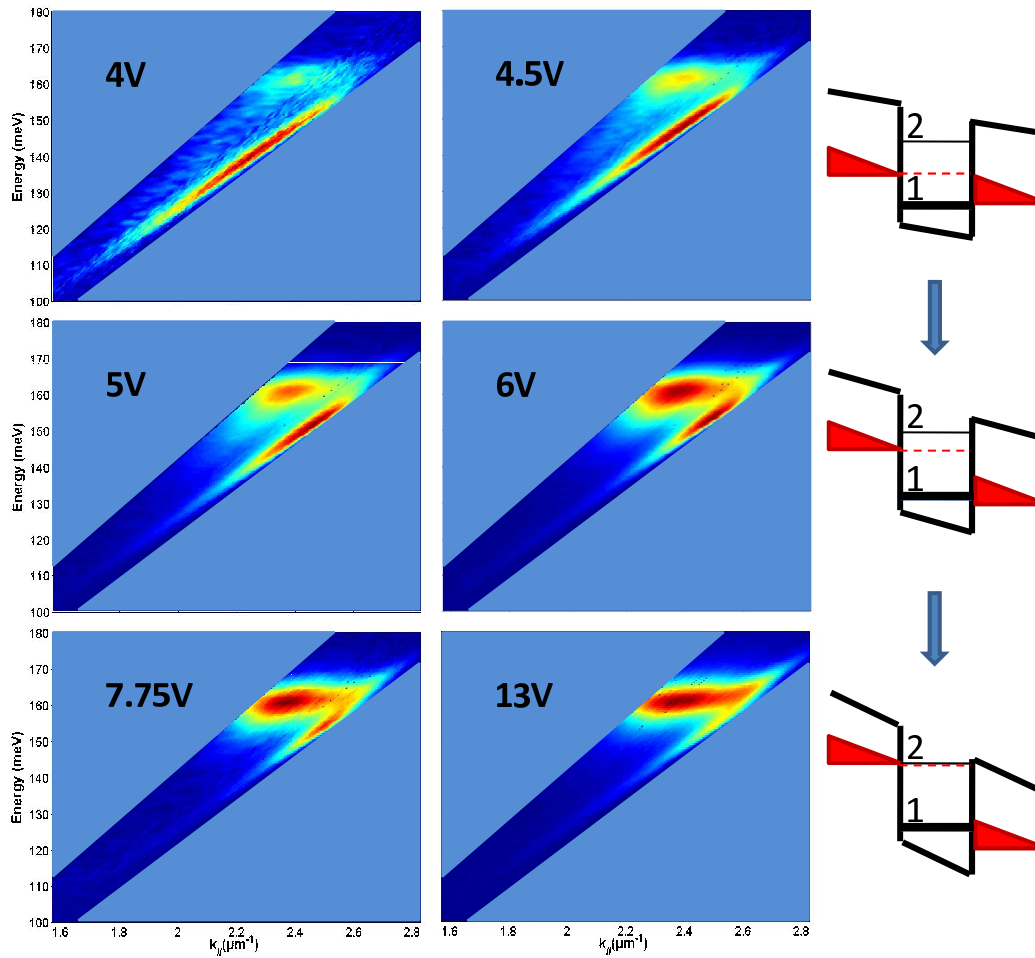
Figure 3.16: Contour plots of the electroluminescence of the polaritonic sample measured at $77K$ as a function of the inplane wave vector and of the energy, for different applied voltages.
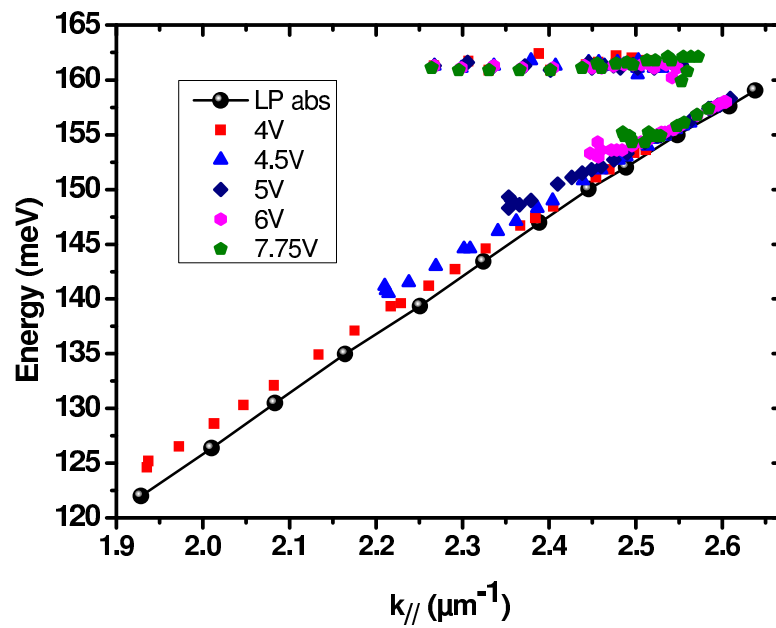
Figure 3.17: Energy position of the maximum peaks from the experimental EL spectra for the different voltages (color dots) as a function of the inplane wave vector. The black curve represents the absorption dispersion (lower polariton branch) calculated with our transfer matrix program.

3.5.2   Simulated EL at different voltages

As the polaritonic absorption depends on the electronic density in the ground state of the transition, we need to estimate its value to simulate the EL at the different applied voltages. In fact, changing the applied voltage can redistribute the electrons in other QWs of the QCS. To estimate the electronic density for each voltage, we have analyzed the wave vector dependence of the EL signal at $160meV$. At this energy close to the intersubband transition, the EL strongly depends on the Rabi splitting and thus changes for different values of the electronic density. As an example we report in the left panel of figure 3.18 the simulations (proportional to $A_N(E, \theta) \times F(\theta)$) for a density $N = 2.10^{11}cm^{-2}$ (black curve), $N = 4.10^{11}cm^{-2}$ (red curve) and $N = 6.10^{11}cm^{-2}$ (blue curve) of the absorption as a function of $k_{\parallel}$. The three curves present indeed a drastically different shape due to the different coupling with the fundamental and first excited cavity mode. We thus plot in the right panel of figure 3.18 the EL signal measured at $160meV$ as a function of $k_{\parallel}$ for each measured voltage. For better comparison, the spectra are normalized to the intensity peak. One can notice that all the spectra present the same shape here which means that the electronic density stays constant for all the voltages studied. The best fit of the experimental data is obtained for $N = 4.10^{11}cm^{-2}$ (red line in the left panel of figure 3.18). As expected, this value is lower than the one at $0V$ bias due to electron redistribution but stays important thanks to the QCS design optimized to preserve a long tunneling time out from the fundamental state (thick extraction barrier).

The consistence of this value can be checked with a rate equation model in which the ground-state population N_1 is given by ([Colombelli et al., 2005])

$$N_1 = \frac{J}{q}\tau_{out} + N \exp\left(-\frac{\Delta}{k_B T}\right) \tag{3.8}$$

where J is the current density, q is the electron charge, τ_{out} the tunneling time from subband 1 into extraction state, N is the total doping concentration minus the density of electrons that participate in the transport, and Δ is the energy difference between state 1 and the quasi-Fermi energy in the previous period, as indicated in figure 2.2. The term $N \exp\left(-\Delta/k_B T\right)$ comes from the so called "back filling" which corresponds to electrons from the extractor thermally populating the main quantum well. From equation 3.8, for a current of $2A$ (corresponding to a voltage of $13V$), we obtain $\tau_{out} \approx 4-5ps$. This is compatible with a tunneling out of the fundamental subband assisted by interface roughness scattering, which in our system gives $\approx 6ps$ [Leuliet et al., 2006]. In the simulations that I will present, the voltage dependance of the electronic density in the fundamental state will be neglected and for each voltage I will consider $N = 4.10^{11}cm^{-2}$.
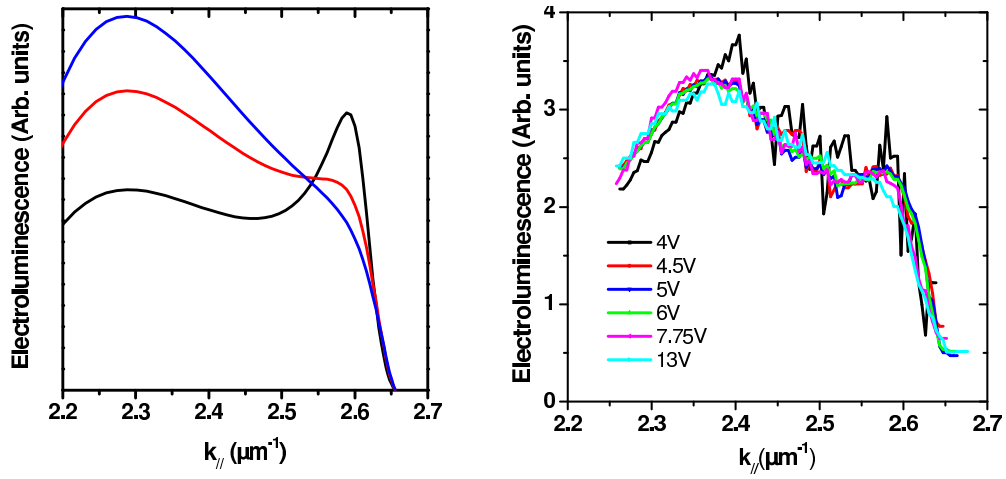
Figure 3.18: Left panel: simulated electroluminescence intensity as a function of the inplane wave vector at the energy of $160meV$ for the polaritonic sample. The black line is obtained for an electronic density of $2.10^{11}cm^{-2}$, the red for an electronic density of $4.10^{11}cm^{-2}$ and the blue for an electronic density of $6.10^{11}cm^{-2}$. Right panel: electroluminescence intensity measured at $77K$ as a function of the inplane wave vector at the energy of $160meV$ for the different applied voltages (color curves) on the polaritonic sample. Each curve is normalized by its corresponding current.

On another side, as the injector energy varies with the voltage, we need to extract the injector characteristics as in subsection 3.3.2 for the different bias. In figure 3.19 are represented the spectra measured for $\theta = 57.9°$ (black dots), the fit (red continuous line) and the two Gaussians from the fit (dashed black line). The maximum intensity of each spectrum is normalized to 1. As the voltage increases, the injector energy increases and its FWHM decreases. Note that the fit for $4V$ is not presented because the signal/noise ratio of the spectra is too low to be accurate. The fit at $13V$ is not shown either because the injector is too close to the intersubband energy.
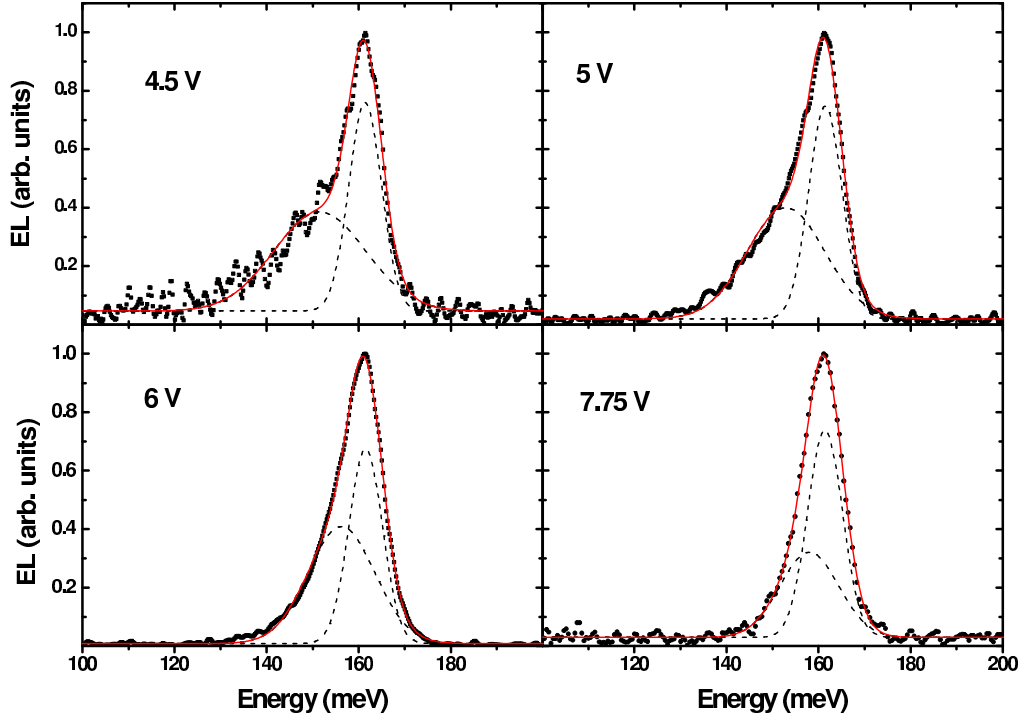
Figure 3.19: Each panel corresponds to a different voltage applied on the QCS. The black dots represents the electroluminescent spectra from the polaritonic sample at $77K$ for an angle $\theta = 57.9$. The red curve corresponds to the fit with the sum of the two gaussians functions (black dashed lines).

Figure 3.20 shows the simulated k space at the same voltages as in figure 3.16. The switch of the dominant contribution from the lower polariton branch to the weak coupling with the higher order mode is well reproduced for each voltage. The increase of the energy and the energy window of the EL perfectly corresponds to the experience.
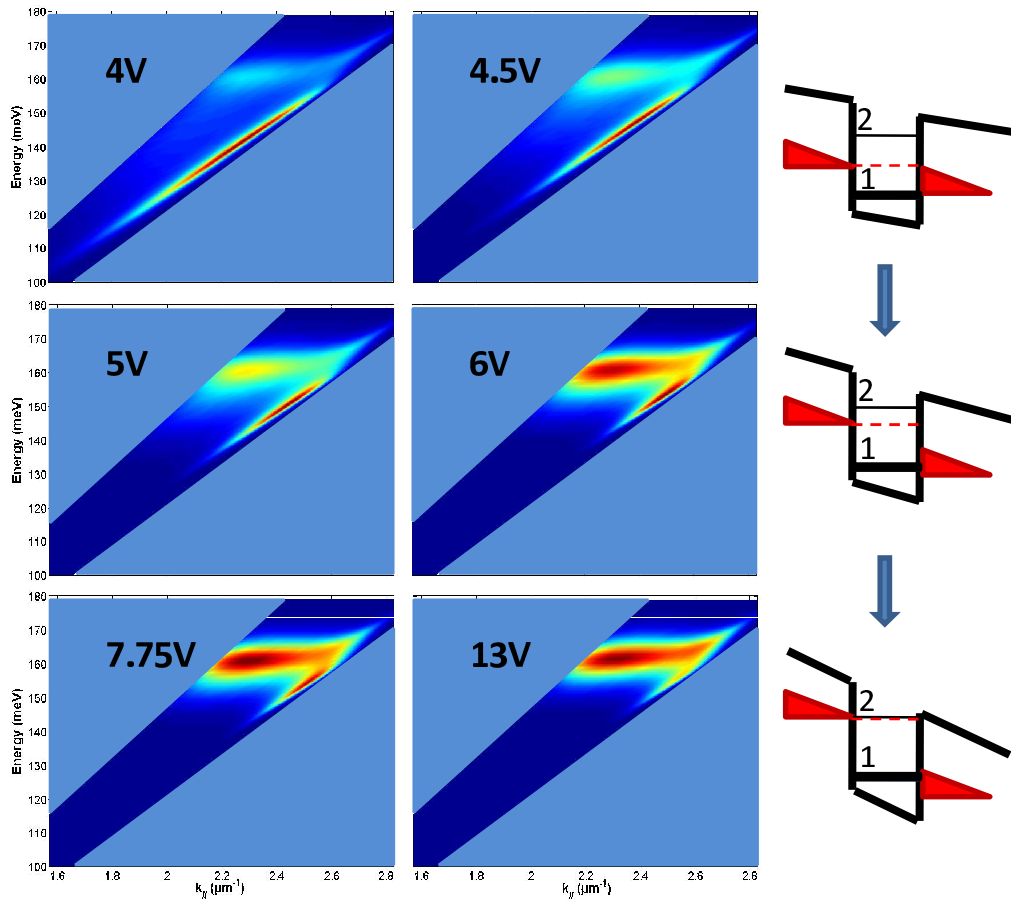
Figure 3.20: Simulated contour plots of the electroluminescence of the polaritonic sample as a function of the inplane wave vector and of the energy, for different applied voltages.

3.5.3 Stark tunability in a single QW

Another way to underline the voltage tunability of the emission is to look at the spectra at a given angle for different voltages. Therefore, we realized a new study of EL spectra between $3.25V$ and $7.75V$. Figure 3.21 and 3.22 show the spectra for each voltage respectively for an angle of 63.4° (from $3.5V$ to $7.5V$ by steps of $1V$) and 74.0° (from $3.25V$ to $7.75V$ by steps of $0.25V$). They are arbitrarily normalized and shifted for better clarity. For 63.4° all the EL spectra are peaked at $\approx 162meV$ with a tail at E_{inj}. At 74.0° the peak shifts from $125meV$ at $3.25V$ to $161meV$ at $7.75V$ and the FWHM decreases from $\approx 40meV$ to $18meV$. Those two very different behaviors in the same voltage range can easily be understood by considering the polaritonic dispersion shown in figure 3.23. In this figure we represent the peak positions of the absorption measured at $0V$ (black triangles), the corresponding simulated absorption dispersion (black continuous line) and the experimental peak position of the EL spectra from figure 3.21 (red squares) and figure 3.22 (blue dots) as a function of the inplane wave vector. The two chosen angles for EL measurements are in two different portions of the polaritonic dispersion. At 63.4° the spectrum only crosses the excited mode at approximately $162meV$; the EL peak is thus always at the same energy. On the contrary, the spectrum at 74.0° follows more or less the lower polariton branch dispersion; the continuum of energy available for the emission allows a tuning of the EL peak with $\Delta\lambda/\lambda \approx 22.5\%$. In the same sample, by only choosing the appropriate angle, we can have both an EL energy that does not depend on the bias or one that strongly varies with the applied voltage, mimicking a Stark effect but in a single quantum well.
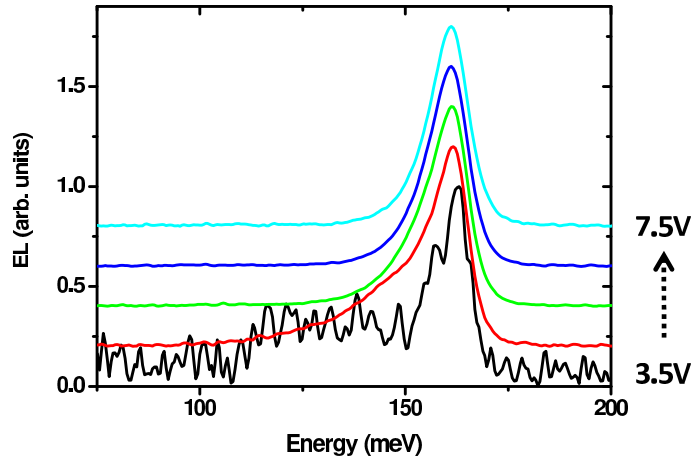
Figure 3.21: Electroluminescence spectra measured for the polaritonic device at $77K$ for $\theta = 63.4°$ with applied voltages from $3.5V$ to $7.5V$ with a step of $1V$. The spectra are normalized to their peak and shifted.
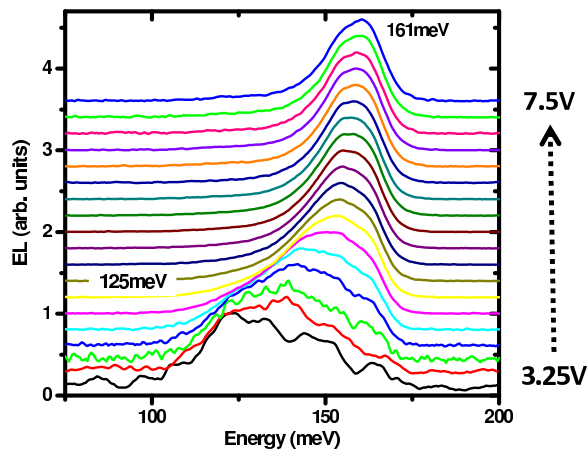
Figure 3.22: Electroluminescence spectra measured for the polaritonic device at $77K$ for $\theta = 74.0°$ with applied voltages from $3.25V$ to $7.5V$ with a step of $0.25V$. The spectra are normalized to their peak and shifted.
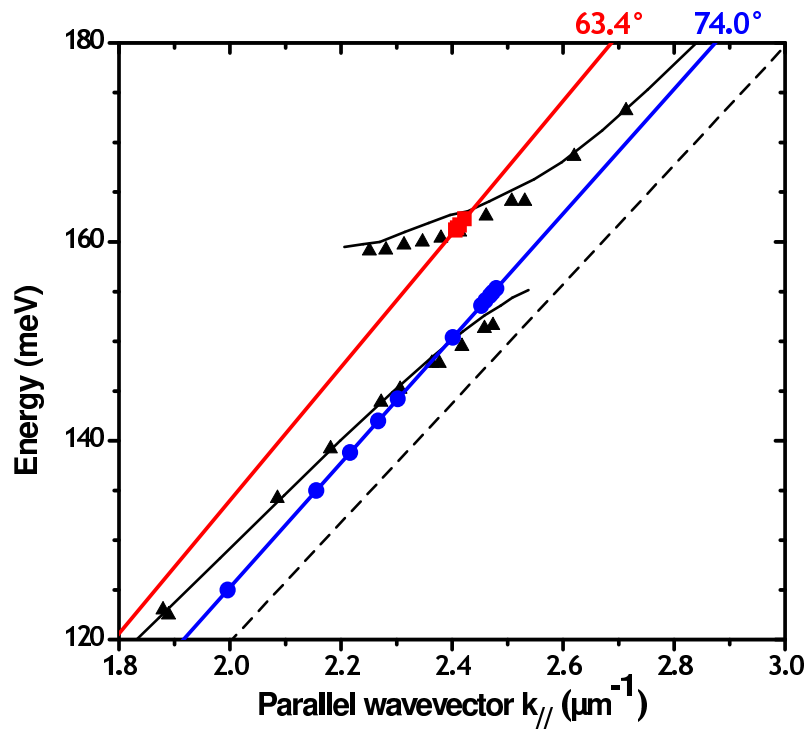
Figure 3.23: Energy dispersion of the polariton branches as a function of the inplane wave vector. The black triangles represent the peaks positions obtained from angle resolved absorption spectra measured at $77K$ with no voltage, the black curves represent the corresponding simulated polariton dispersions, the red squares (blue dots) shows the peak positions of the electroluminescence measured at $77K$ for $\theta = 63.4°$ ($\theta = 74.0°$) for different applied voltages.

3.6 Quantum efficiency

To investigate the difference in the EL signal between the strong and weak coupling regime, we will take advantage of the spatial separation of the weak and strong coupling contributions in the polaritonic sample. Indeed, the strong coupling appears in an angle interval between 66° and 82° while the weak one corresponds to lower angles. The top panel of figure 3.24 shows the integrated EL intensity as a function of the angle θ. It is normalized to the current for each voltage and it is thus proportional to the quantum efficiency. The low angle peak is associated to the weak coupling regime. As a consequence the quantum efficiency is the same for all voltages. The first noticeable difference between these curves is the increase in the quantum efficiency associated to the polaritonic peak when decreasing the voltage applied to the structure: at $4V$ the polaritonic quantum efficiency is twice the weak-coupling one. A second difference between the curves is a small angular shift of the peak of the quantum efficiency ($+1.4°$ when going from $4V$ to $13V$). This is related to the shift of the injector energy with the voltage. These two aspects of the voltage evolution of the quantum efficiency are very well reproduced by our simulations, shown in the bottom panel of figure 3.24, which are obtained by integrating at each angle the electroluminescence spectra of figure 3.20. In the simulations, only the radiative lifetime of the polaritons is taken into account as we only calculate the energy dispersion due to the coupling of the cavity mode to Lorentz oscillators in the quantum well. The fact that our data are well reproduced by these simulations indicates that the observed enhancement comes from a Purcell-like effect and is due to the increased photonic density of states of the fundamental mode with respect to the excited mode.

An other way to represent the EL intensity is to integrate it as a function of the energy. In figure 3.25, we take advantage of the spatial separation of the weak and strong coupling contributions and only integrate the spectra for angles above 66°. This allows to see the evolution of the contribution on the lower polariton branch only. Two behaviors are visible as the applied voltage increases (color curves). First the peak energy shifts toward higher energies (the electrical injection is tuned with the voltage) and second, the maximum intensity (and the area) decreases as the injection gets closer to the intersubband transition energy.

The fact that we do not obtain the expected enhancement due to the polaritons is attributed to the *dark states* (DS) [De Liberato and Ciuti, 2009a] described in the first chapter. Their energy is the same one as the intersubband transition as schematized in figure 3.26.

In our sample, the electronic injector always has an overlap with the dark
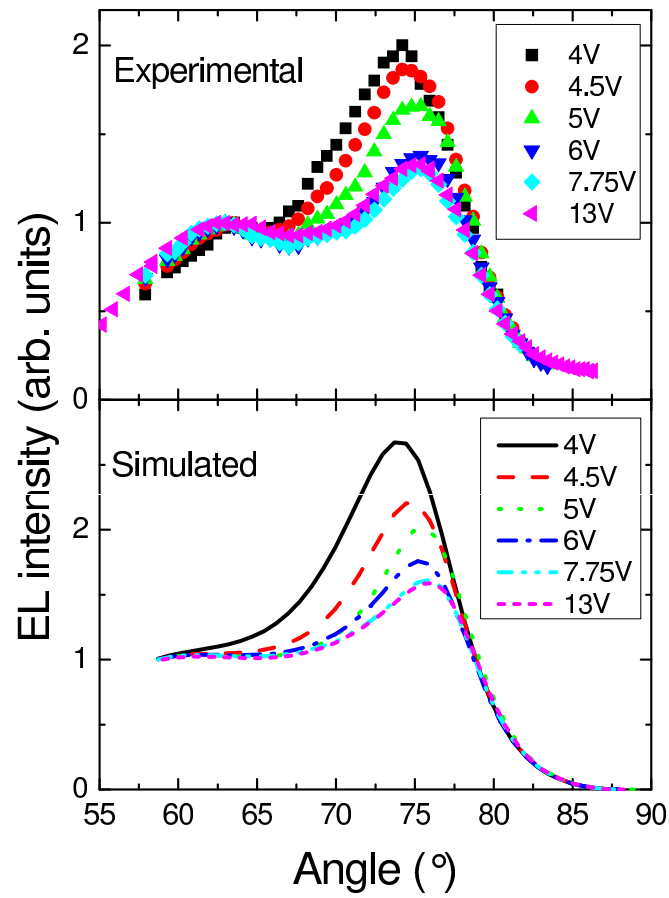
Figure 3.24: Experimental (top panel) and simulated (bottom panel) integrated intensity of the electroluminescence spectra as a function of θ for different voltages. The experimental curves are normalized by their corresponding current to be proportional to the quantum efficiency.
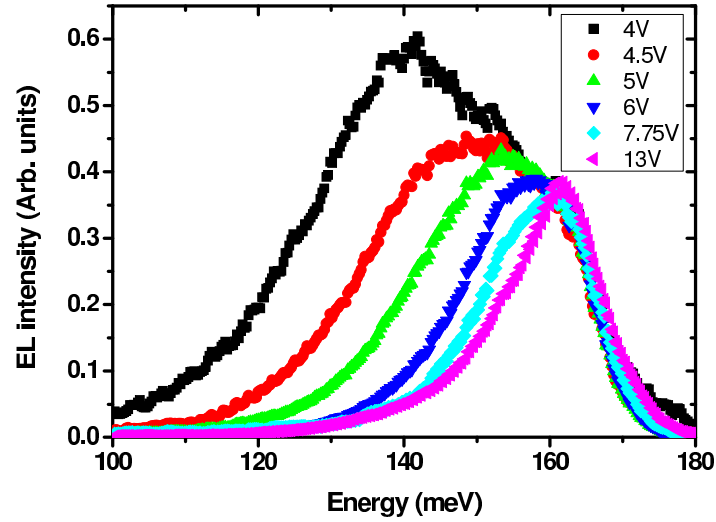
Figure 3.25: Experimental integrated intensity of the electroluminescence spectra taken above 66° as a function of the energy for different voltages. The experimental curves are normalized by their corresponding current to be proportional to the quantum efficiency.
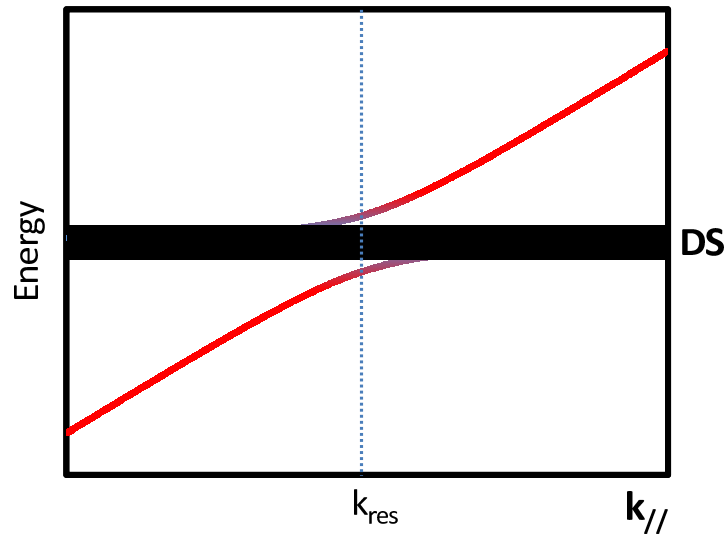
Figure 3.26: Schematic representation of the polaritonic dispersion as a function of the inplane wave vector. The black dashed line is the intersubband transition energy and the black rectangle represents the dark states.

states. Therefore, due to their spectral weight, most of the electrons are injected in the dark states and thus do not participate in optical emission. The electronic transport in our structure is thus governed by the dark states. In our device, the band structure simulations predict that above $6V$ the energy of the injector should be above the energy of the excited state and thus that the electronic injection should appear in the upper polariton branch. This is in contradiction with the datas presented in figure 3.16 where, for voltages above $6V$, no contribution comes from the upper polariton branch. It can be explained because the electrical transport in our structure is dominated by the dark states. Therefore, the best configuration is obtained when the injector is tunneling resonant with the dark states and results in the locking of the injector at the ISB energy for voltages higher than $6V$.

3.7   Conclusion

To conclude, the data and simulations presented in this chapter have proven the electrical resonant injection in the polariton states. This allowed us to obtain electroluminescence at energies otherwise unreachable. A detailed study of the data has permitted to investigate the different parameters controlling the polaritonic emission. The voltage dependance of the EL has also been investigated and a large tunability of the emission energy has been reached.

To bypass the problem of the dark states to enhance the polaritonic quantum efficiency, we believe that a larger Rabi splitting is necessary as well as a new cavity design to obtain a dispersion-less cavity mode giving rise to a high photonic density of state. In this configuration a resonant injection specifically in the polariton states would be easier. It is with those objectives in mind that we studied another type of cavity for strong coupling in the following chapters.

Chapter 4

Double metal cavities in the mid infrared

Contents

4.1 Introduction

In order to obtain a more suitable device for a selective electrical injection in intersubband polariton states, we explored a different photonic confinement for mid-infrared wavelengths. The cavities that we realized are based on a semiconductor slab embedded between two metallic layers, one of which is patterned as a periodic grating. This type of cavity has already been used in different energy ranges of the electro-magnetic spectrum, particularly in the microwaves ranges [Hibbins et al., 2004],[Lockyear et al., 2009] and THz

[Todorov et al., 2010b] to confine and manipulate light at sub-wavelength dimensions. There are two main advantages for using these cavities to realize polaritonic devices. The first one is the possibility to use extremely sub-wavelength dimensions for the light confinement. For polaritonic systems, 1.28 indicates that the Rabi frequency is proportional to $1/\sqrt{L}$; decreasing the cavity length is thus a synonym of increasing the splitting between the polaritonic branches. The second aspect concerns the energy dispersion of the cavity mode; by choosing the appropriate parameters, it is possible to obtain dispersion-less modes, characterized by a high density of photonic states which are very suitable for resonant electrical injection.

In this chapter, after describing the photon confinement in Metal-Dielectric-Metal (MDM) cavities, I will present my experimental results that demonstrate the feasibility of similar cavities in the mid-infrared domain. The influence of their different parameters will be studied in detail both with experiments and simulations. I will conclude by describing some experimental advantages of the MDM cavities. All the measurements presented in this chapter have been realized at room temperature. Some of the results presented here have been published in [Jouy et al., 2011a].

4.2 Photonic confinement in MDM cavities

4.2.1 Double metal cavity mode

To understand the confinement in our MDM cavities we consider the simplest double metal cavity geometry (schematized in figure 4.1) made of a semiconductor slab of thickness L (assimilated to the cavity length) embedded between two metallic mirrors. To begin with, we will consider perfect metals to describe the light confinement. The x direction corresponds to the direction of propagation of the light in the semiconductor layer plane (to simplify, $k_y = 0$) while z corresponds to the direction perpendicular to the layer. This geometry supports both TM and TE guided modes confined between the two metallic mirrors. As represented in the bottom of figure 4.1, the only non-zero components for the TM modes are E_z and E_x for the electric field and H_y for the magnetic field while for TE modes it is E_y for the electric field and H_x and H_z for the magnetic field. To obtain confined guided modes, the boundary conditions on the electric field for perfect metals impose the tangential components to nullify at the interface metal/semiconductor ($E_x = E_y = 0$ for $z = 0$ or $z = L$), E_z to vary as $\cos\left(z\frac{\pi Q}{L}\right)$ and E_x and E_y to vary as $\sin\left(z\frac{\pi Q}{L}\right)$ along the z axis with Q the mode index and $z = 0$ at the interface of the lower metallic mirror and the semiconductor. In particular for $Q = 0$, in the z di-

rection, $E_z = cst$ and $E_x = E_y = 0$. As a result, the TE_0 mode does not exist (as all its electric field components are equal to zero) and for the TM_0 mode, only the component E_z is different from zero and is constant along the z axis. The intensity along z of E_z for the TM_Q and of E_y for the TE_Q first modes is schematized in figure 4.1 with a blue line.

Solving Maxwell equations for this geometry [Adams, 1981] allows to obtain the energies of the different cavity modes. Their energy dispersion as a function of the inplane wave vector k_x is shown in figure 4.2 and it is given by the Helmholtz equation:

$$E = \frac{\hbar c}{n}\sqrt{k_x^2 + k_y^2 + k_z^2} \quad with \quad k_y = 0 \quad and \quad k_z = \frac{\pi Q}{L} \qquad (4.1)$$

where n is the semiconductor refractive index. The dispersions have been calculated for $n = 3.3$ (which corresponds to the $GaAs$ refractive index in the MIR) and $L = 0.3\mu m$. For $Q \geqslant 1$ the cavity modes correspond to a standing wave in a $\lambda/2$ like mode and the TM_Q and TE_Q modes have the same energies. The minimum energy of those modes (called cut off energy) is obtained for $k_x = k_y = 0$ and it is related to the cavity length L as $E_{cut\ off} = \hbar c \pi Q / nL$. This means that to confine photons of a certain energy implies a minimum thickness for L. A $300nm$ thick $GaAs$ cavity can thus not confine photons of less than about $630meV$. On the contrary for $Q = 0$, $k_z = 0$. Therefore the confinement of the TM_0 mode does not depend on L and thus does not present a cut off energy, allowing arbitrarily thin cavities. Actually, the metal is not perfect and a small fraction of the electromagnetic field penetrates in it. To take into account this effect on the light propagation in the MDM cavity we use an effective refractive index n_{eff} instead of n. We obtain in section 4.4.2 a value of $n_{eff} = 4.5$ in the MIR for a cavity thickness of $0.3\mu m$ which only reduces the minimum cut off energy to about $460meV$. Because we are interested in very small cavity volumes (less than $300nm$) at energies around $110meV$, only the TM_0 mode can be exploited for light confinement.

An advantage of the TM_0 mode in double metal cavities, compared for example to the single metal cavities presented in the first chapters, is that the entire intensity of the electric field is confined between the two mirrors (we can neglect the fraction in the metal) as it is almost zero at the metal/semiconductor interface. On the other hand, one inconvenient of this design is the difficulty to couple the cavity mode with the free space due both to small dimensions (typically $300nm$ thick cavities for mid-infrared) and to the impedance mismatch at the end of the cavity. One can intuitively understand this point when considering the spacial distribution of the mode. Indeed, because $L \ll \lambda_0$ where λ_0 is the cavity mode wavelength, the transvers Fourier transform of the cavity profile on the facet that gives its wave vector
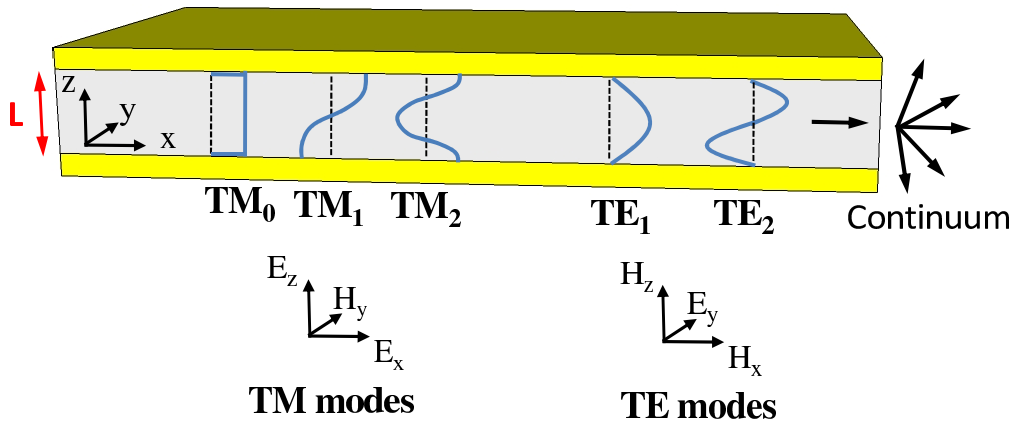
Figure 4.1: The top part is a scheme of a double metal cavity. The left three blue curves represent the vertical electric field component intensity E_z along the z axis for the three first TM modes. The right two blue curves represent the horizontal electric field component intensity E_y along the z axis for the first and second TE modes. The bottom part shows the nonzero components of the electric and magnetic fields for TM and TE modes.
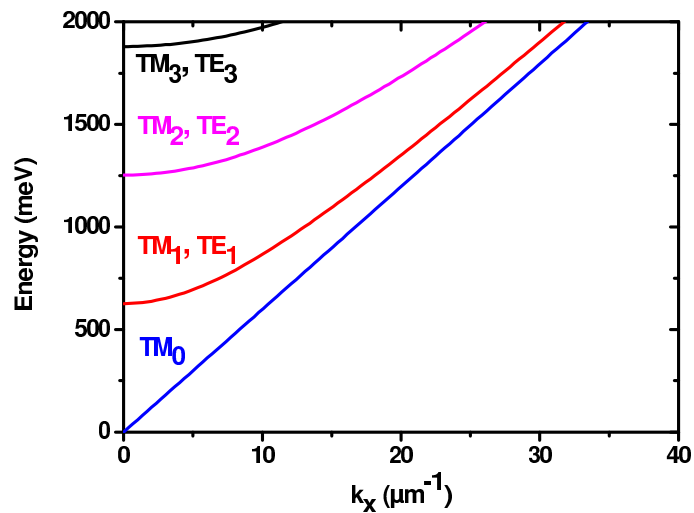
Figure 4.2: Calculated energy dispersion as a function of the inplane wave vector for the first TM and TE modes. The calculation is made for a double metal cavity made of perfect metals and a $GaAs$ semiconductor core of constant refractive index $n = 3.3$.
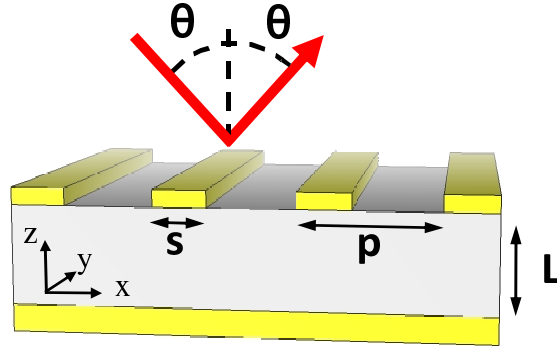
Figure 4.3: Scheme of our MDM cavity. The parameters of the top metallic grating are the strip width s and the period p. The core thickness is L. The angle for the light propagation on the surface of the sample is θ.

distribution covers a very broad range of wave vectors. On the contrary, in the free space, the wave vectors Fourier components are limited by the *light cone* given by $|k| < 2\pi/\lambda_0$. Therefore, only the photons satisfying $|k| < 2\pi/\lambda_0$ can exit the cavity and propagate in the free space while the others (which represent the majority) bounce back in the cavity. This phenomena is responsible for the high reflectivity of facet with sub-wavelength dimension. To prevent this problem, different approaches have been imagined for example in double metal lasers [Kumar et al., 2007], [Maineult et al., 2008] to extract the light from such cavity modes.

Instead of two planar metallic mirrors we chose to replace the top one with a metallic periodic grating allowing the coupling with the free space through the sample surface. Note that here the periodicity of the grating is not engineered to match the confined photons wavelength as in a DFB (distributed feed back) cavity. Figure 4.3 represents a scheme of the cavity with L the semiconductor thickness, s the width of the metallic strips and p its period. Additionally, because the top metal is not infinite anymore, the TM_0 mode can no longer propagate freely along the x direction and only the modes forming a standing wave under the metallic strips are supported. We simulate the vertical component of the electric field (E_z) by using the modal method formalism with surface impedance boundary conditions [Todorov and Minot, 2007]. Figures 4.4 represents in color scale the simulated E_z component for the first standing wave cavity modes for an incoming plane wave with a normal incidence on the cavity ($\theta = 0°$). It shows that the mode is localized under the metallic strips and that modes from two neighbors strips are uncoupled. One can notice that E_z slightly leaks in the semiconductor from the region

between two metallic strips. This translates in an effective strip width s_{eff} slightly larger than s. We choose to integrate this effect in the effective refractive index n_{eff} introduced above. Keeping $k_y = 0$, the following condition
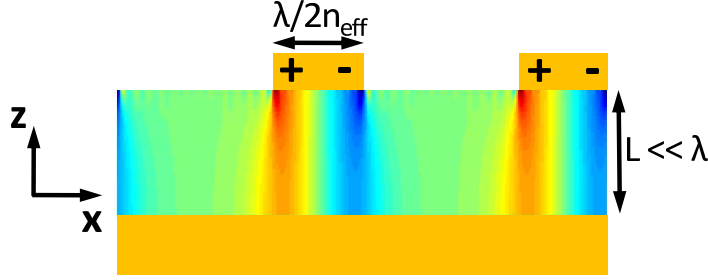
Figure 4.4: Coupe of the MDM cavity perpendicularly to the metallic strips. The color scale represents the simulated intensity of the vertical component of the electric field E_z in the semiconductor. The "+" and "-" signs scheme the electrons oscillations in the metallic strips.

on the cavity mode wavelength is obtained

$$\lambda = \frac{2s n_{eff}}{K} \tag{4.2}$$

where K is a non-zero integer corresponding to the number of nodes along the x axis for E_z and n_{eff} is the effective refractive index of the cavity mode. The dispersion due to k_y in our devices will be studied in the section 5.5 of the next chapter where we estimate the shift in energy to be negligeable as of less than 5%. This geometry thus allows the confinement of the light also in the x direction and to obtain dispersion-less cavity modes.

It is easy to couple light in this type of cavity from free space as it acts as a patch antenna. Indeed, the electric field of an incoming electro-magnetic wave is gonna make oscillate the electrons in the metallic strips (as schemed in figure 4.4). These oscillations of charges can then couple to the E_z component of the MDM cavity mode.

4.2.2 Surface plasmon mode

In our MDM cavities, the lower continuous metallic mirror permit the propagation of plasmonic modes at its surface. Because the metals are not perfect, those modes present losses and their energy is limited by the so called *plasma energy*. I will now briefly present the main properties of surface plasmons that will be used in this work.

For metal/dielectric or metal/air interfaces, the electromagnetic field can be confined at the metal surface and its amplitude exponentially decreases in the semiconductor or air region (see right pannels of figures 4.5 and 4.6). At the interfaces the coherent oscillations of the free electrons of the metal support the so called surface plasmon polariton (SPP) modes. In general for an interface between a metal (of dielectric constant ε_m) and a medium with dielectric constant ε_1, the SPP energy dispersion is given by the equation

$$E = \hbar c k_x \sqrt{\frac{1}{\varepsilon_m} + \frac{1}{\varepsilon_1}} \tag{4.3}$$

where k_x is the inplane wave vector in the x direction and c the light velocity. In the free electron Drude model the metal dielectric function depends on E as

$$\varepsilon_m(E) = 1 - \frac{E_P^2}{E^2} \quad \text{with} \quad E_P = \hbar \sqrt{\frac{Ne^2}{\varepsilon_0 m}} \tag{4.4}$$

where E_P is the plasma frequency, N the bulk electron density of the metal, e the electron charge, ε_0 the vacuum permitivity and m the electron mass. The cavity mode energy dispersion is thus limited for large k_x by the surface plasma energy (E_{SP}) related to the maximum frequency to which free electrons from the metal can oscillate. It is given by

$$E_{SP} = \frac{E_P}{\sqrt{1 + \varepsilon_1}} \tag{4.5}$$

Figure 4.5 represents the SPP energy dispersion as a function of the inplane wave vector (black curve) and the light line (red line) for a metal/air interface (as schematized on the right panel). For small k_x the SPP is very close to the light line $E_{ll} = \hbar c k_x$. When k_x becomes comparable and greater than $E_{SP\ air}/\hbar c$, the energy dispersion tends asymptotically to the surface plasma energy $E_{SP\ air} = E_P/\sqrt{2}$ (indicated with a dashed blue line in the figure). The right panel represents the intensity decay of the plasmon electric field along z in the air. The decay length corresponds to the distance to the surface to which the field is divided by a factor e. It is given in the air by

$$z_{decay} = \frac{1}{|k_z|} \quad \text{with} \quad k_z = \sqrt{\frac{\omega^2}{c^2} - k_x^2} \tag{4.6}$$

If we replace the air with a semi infinite semiconductor region as $GaAs$ (see scheme and energy dispersion in figure 4.6), the light line becomes $E_{ll} = \hbar k_x c/n$ where n is the semiconductor refractive index and the cavity energy

Figure 4.5: Left panel: calculated energy dispersion of the air-gold SPP as a function of the inplane wave vector (black continuous curve). The red line represents the light line and the dashed blue line corresponds to the asymptote $E_{SP\ air}$ of the SPP. Right panel: scheme of the interface and of the decay length of the SPP along the z axis (black line).
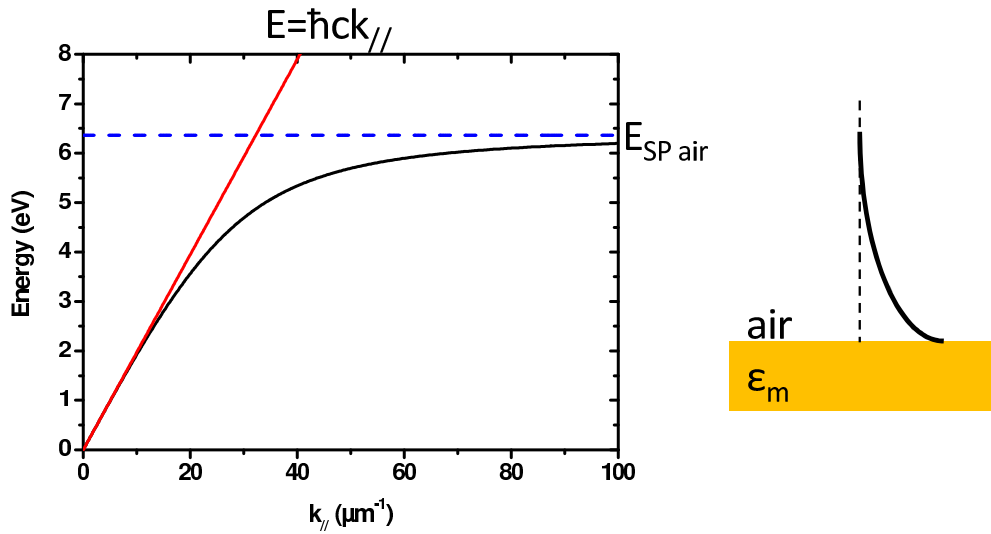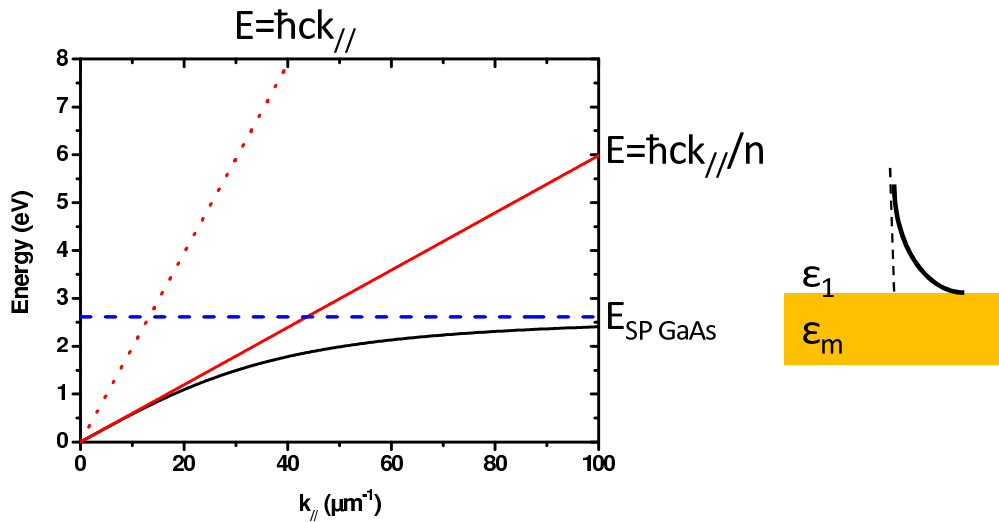

Figure 4.6: Left panel: calculated energy dispersion of the $GaAs$-gold SPP as a function of the inplane wave vector (black continuous curve). The red line represents the light line and the dashed blue line corresponds to the asymptote $E_{SP\ GaAs}$ of the SPP. Right panel: scheme of the interface and of the decay length of the SPP along the z axis (black line).

asymptote becomes $E_{SP\ GaAs} = E_P/\sqrt{(1+\varepsilon_1)}$. The decay length is now given by

$$z_{decay} = \frac{1}{|k_z|} \quad \text{with} \quad k_z = \sqrt{\frac{\varepsilon_1 \omega^2}{c^2} - k_x^2} \tag{4.7}$$

The field is thus more compressed in the semiconductor than in the air.

For the SPP, the cavity in figure 4.3 presents two different zones: a metal/semiconductor/metal interface under the metallic strips and a metal/semiconductor/air interface between the metallic strips.

In the Metal/semiconductor/metal region, because the semiconductor thickness is smaller than the decay length of the SPP, the electric field intensity is compressed in the semiconductor slab between the two metallic layers, as the plasmon almost does not penetrate in the metal. For the metal/semiconductor/air zone, the two regimes described in figures 4.5 and 4.6 take place as shown in figure 4.7. Indeed, for small inplane wave vectors, the decay length is large and most of the SPP mode is localized in the air and almost does not overlap with the $300nm$ thick semiconductor slab. In this region, the SPP energy follows the one of the metal/air SPP. When increasing the inplane wave vector, the decay length becomes shorter and shorter until most of the SPP field is concentrated in the semiconductor. The dispersion thus follows the one of the metal/semiconductor SPP and tends to the asymptote $E_{SP\ GaAs}$.

As the SPP energy dispersion is always below the light line, it does not couple to the free space radiation. Thanks to the periodicity of the cavity grating, the diffraction phenomena appears and the SPP dispersion is folded back in the first Brillouin zone ($k_x^{Brillouin} = \pi/p$) as shown in figure 4.8. The first diffraction order to come into play is the -1 diffracted order which, for the light line, has a wavelength of

$$\lambda_{-1} = p(1 + \sin\theta) \tag{4.8}$$

where θ is the angle of collection of the photons with respect to the z axis. This allows the SPP to couple with the free space when above the light line [Hibbins et al., 2006]. If we change the periodicity of the grating, we change the value of the inplane wave vector corresponding to the first Brillouin zone limit $k_x^{Brillouin}$. Figures 4.8 and 4.9 represent the energy dispersion of a SPP as a function of the inplane wave vector for two gratings with different periodicities. In both cases, the black curve is the plasmon dispersion in the first Brillouin zone (delimited by the vertical dashed black line), the red continuous line represents the light line, the red dotted line represents the different diffracted orders of the light line in the first Brillouin zone and the purple dashed line represents the energy for an angle $\theta = 30°$. We can notice that
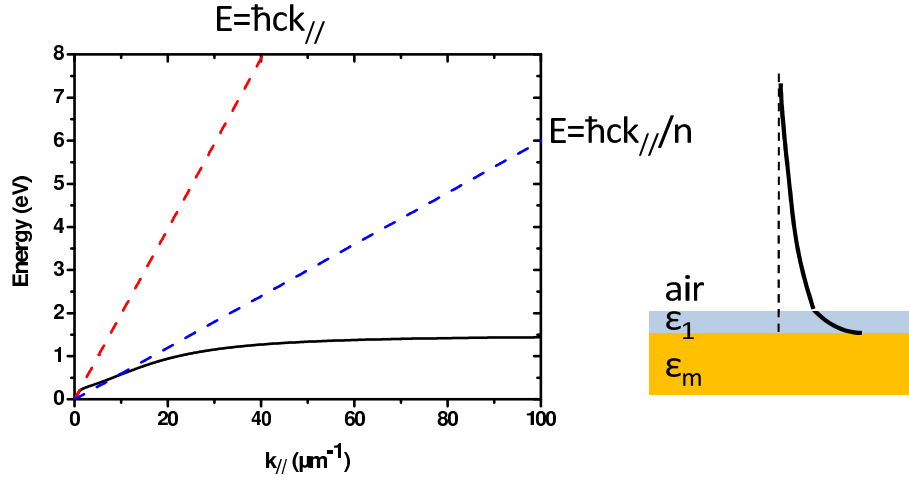
Figure 4.7: Left panel: Calculated energy dispersion of the air-semiconductor-gold SPP as a function of the inplane wave vector (black continuous curve). The red line represents the light line in the air and the dashed blue lines corresponds to the asymptote E_{SP} and $E_{SP\ GaAs}$ of the SPP. Right panel: scheme of the interface and of the decay length of the SPP along the z axis (black line).

for a fixed k_x (or θ) the SPP will be observed at an energy depending on the grating period. For example, in figures 4.8 and 4.9, for $k_x = 5\mu m$ ($\theta = 30°$) the SPP energy is respectively at about $0.9eV$ and $1.6eV$ ($0.8eV$ and $1.4eV$).

Those different features for the SPP will be experimentally observed in section 4.4.3.
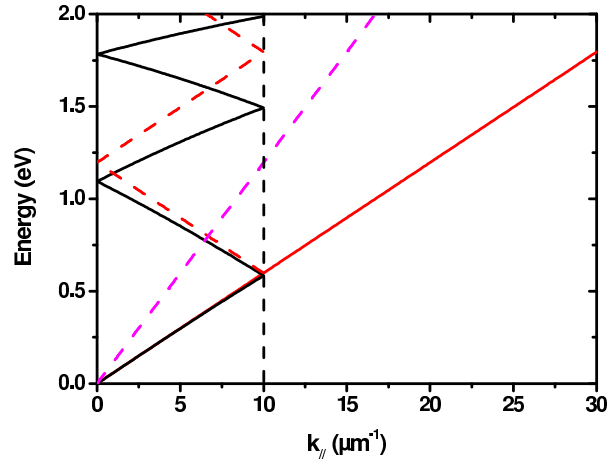
Figure 4.8: SPP energy dispersion as a function of the inplane wave vector in the first Brillouin zone for a period $p = \pi/10$ (black continuous curve). The continuous red line is the corresponding light line and the dashed red line represents its different diffracted orders in the Brillouin zone. The dashed purple line shows the position of a spectra for $\theta = 30°$.
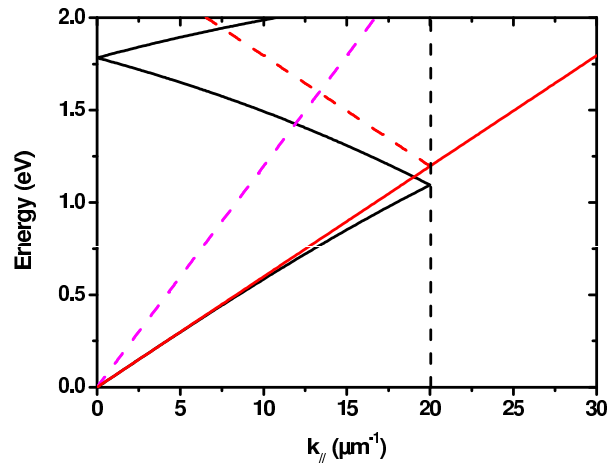
Figure 4.9: SPP energy dispersion as a function of the inplane wave vector in the first Brillouin zone for a period $p = \pi/20$ (black continuous curve). The continuous red line is the corresponding light line and the dashed red line its different diffracted orders in the Brillouin zone. The dashed purple line shows the position of a spectra for $\theta = 30°$.

4.3   Sample processing

This section is devoted to the description of the samples and of the processing steps. The samples that I will describe in this chapter have been grown by MBE in TASC (Trieste, Italy) by G. Biasiol and L. Sorba.

Due to lattice mismatch between gold and $GaAs$ crystal it is not possible to grow the semiconductor on top of a gold layer. To bypass this problem a special fabrication process is necessary (schematized in figure 4.10), called wafer bonding. A $300nm$ thick $Al_{95\%}Ga_{5\%}As$ stop layer is grown on the $GaAs$ substrate wafer before the active region is grown. In this chapter the "active region" is simply a $300nm$ $GaAs$ layer. In the following chapters I will consider the case of a system of quantum wells. A thick gold layer (Ti/Au $10nm/500nm$) is deposited on top of the active region as well as on a host substrate. The Ti layer plays the role of an adhesive layer, to help the gold evaporation on the surface. The two wafers are sent for thermo-compression to an external company. The $GaAs$ substrate is mechanically thinned down to approximately $100\mu m$. A citric acid solution selectively attacks the remaining $GaAs$ substrate and stops on the $Al_{95\%}Ga_{5\%}As$ stop layer. HF allows to selectively remove the stop layer without damaging the active region. Finally, depending on the grating dimensions the top metallic strips are realized with optical ($s > 2\mu m$) or e-beam lithography ($s < 2\mu m$). In both cases the definition of the patterns strongly depends on the thickness of the resist. The thinner the resist, the better the precision. I chose a $1.4\mu m$ thick resist for optical and a $300nm$ thick resist for e-beam lithography. To avoid any complication during the lift-off step after the metal deposition, one needs a ratio of at least 1:3 between the thicknesses of the metal and of the resist layer. Therefore, the top metal grating is only 76nm (Ti/Au $5nm/76nm$) thick for e-beam lithography while I can use the same thickness as for samples of chapters 2 and 3 for optical lithography (Ti/Au $10nm/200nm$).

Figure 4.11 shows a colored SEM (Scanning Electron Microscope) picture (the gold is tinted in yellow while the semiconductor is in blue) of a typical grating obtained with e-beam lithography. For most of the MDM processes I used the e-beam lithography at the Ecole Normale Supérieure.
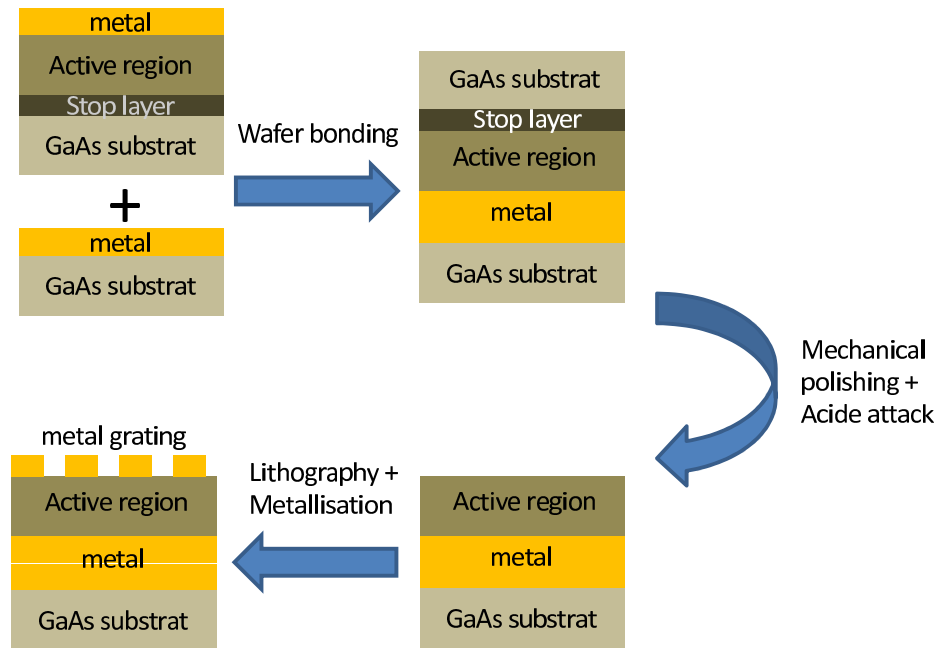
Figure 4.10: Scheme of the different steps for a double metal cavity process.
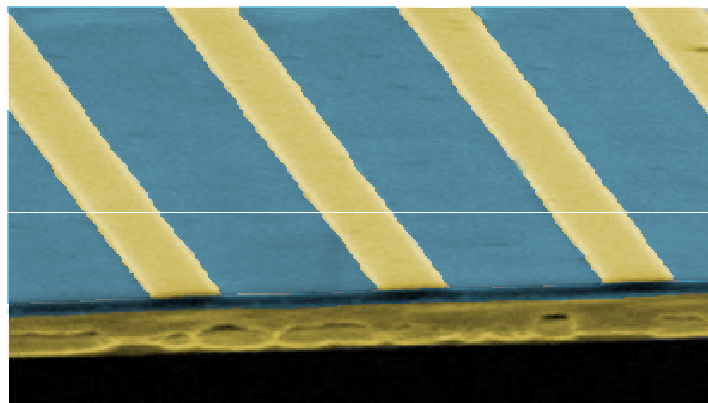
Figure 4.11: Scanning electron microscope picture of a device in false colors (blue for the *GaAs* and yellow for the gold).

4.4   Reflectivity measurements

4.4.1   Experimental setup

In order to characterize the sample, we realize reflectivity measurements. The experimental set-up is shown in figure 4.12. As in chapter 2, a globar is used as broadband source for the MIR (see spectrum in figure 2.14); its beam goes through the FTIR; is then focused thanks to a parabolic mirror on the sample surface with a chosen angle θ. The reflectivity signal is finally collected at the same angle θ and refocused on a detector by two parabolic mirrors. For angles from 30° to 65° the detector is the same MCT as used for measurements of Chapter 2 and 3. A special mount allows to perform 10° reflectivity measurements directly inside the interferometer using a DTGS (triglycine sulfate) pyroelectric detector. In this chapter, we will only vary angles in the xOz plane (see figure 4.3) and keep an incidence normal to the surface in the yOz plane.
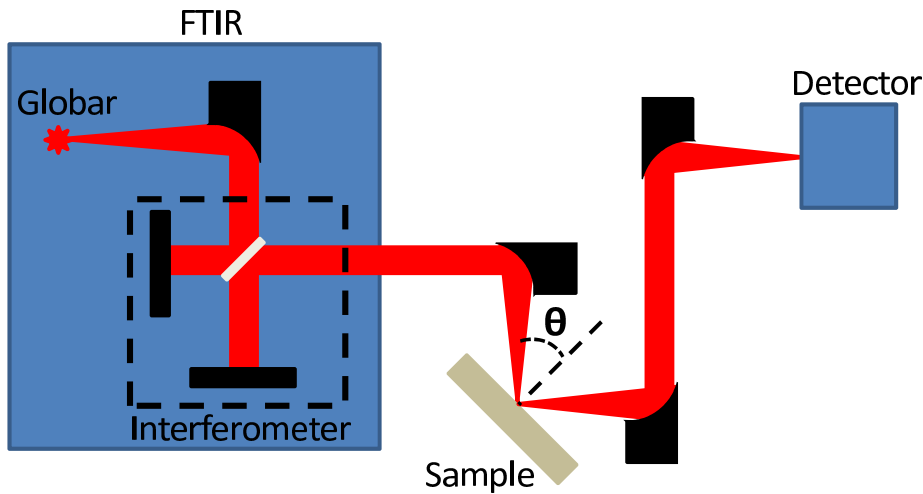
Figure 4.12: Scheme of the reflectivity measurement set up.

4.4.2   Dependency of the photonic modes on the strip width

Following equation (4.2), the energy of the confined modes depends on the strip width. To experimentally verify this dependence and estimate the effective index n_{eff}, we realized several gratings with $s = 0.4\mu m$ to $2.5\mu m$

while the distance between the strips is kept constant $(p - s) = 2\mu m$. Figure 4.13 shows the reflectivity spectrum measured at 45° (black line) for a grating $s = 0.8\mu m$. We can clearly see the first and second order cavity modes at respectively $155meV$ and $240meV$ with quality factors of respectively 7 and 10. The red dashed curve represents the simulated reflectivity spectrum for an incoming plane wave propagating at 45°. The simulations are in a very good agreement with the data using the parameters $s = 0.78\mu m$, $p = 2.71\mu m$ and a dielectric constant for the gold $\varepsilon(E) = 1 - 2.29 \times 107/[E(E + i145)]$, with E the photon energy in meV. Note that the metal losses in this formula are increased with respect to the values known from the literature [Palik, 1998]. This could be due to scattering on the semiconductor-metal interface and to the presence of Ti adhesive layers between the semiconductor and the gold coatings.

It is important to pinpoint that a high contrast (about 90%) is obtained for the first order cavity mode of this grating. This is achieved thanks to an optimization of the grating openings $(p - s)$ in order to reach the situation where the amplitude coupled in the cavity and the losses within it are equal (see [Cai et al., 2000]). The influence of the parameter p on the spectra will be discussed in the next subsection. Figure 4.14 shows the reflectivity measurements at 45° for the first order mode for $s = 0.4\mu m$ up to $1.3\mu m$ with $(p - s) = 2\mu m$ and for $s = 2\mu m$ and $s = 2.5\mu m$ with $(p - s) = 2.25\mu m$. It worth noticing that by varying s from $0.4\mu m$ to 2.5 μm the first order cavity mode energy is continuously tuned from $5\mu m$ up to $20\mu m$ (i.e. from $60meV$ up to $240meV$). On an other hand, the FWHM of the cavity modes remain of the order of 15% of the cavity mode energy which is comparable to the typical width of the ISB transition ($\delta\lambda/\lambda \approx 10\%$) and does not hinder the observation of the strong coupling regime.

Figure 4.15 summarizes the first (red dots) and second (black dots) order cavity mode energies as a function of s; the squares are for the gratings realized with e-beam lithography while the dots are for the gratings realized with optical lithography ($s > 2\mu m$) on another part of the sample. It appears that the cavity wavelength does not increase linearly with s because of the wavelength dependance of n_{eff}. Indeed, figure 4.16 gives the effective index of the cavity modes extracted from the data of figure 4.15 using equation (4.2) as a function of the wavelength. For comparison we also show the bulk $GaAs$ refractive index (purple dots) obtained from [Palik, 1998]. The value of n_{eff} is greater than that in bulk $GaAs$ in the entire wavelength range as expected from a thin slab embedded between two higher optical refractive index layers. The wavelength dependency and especially the great increase of the effective index for short wavelengths can be explained by the plasmonic nature of the cavity modes. Indeed the cavity mode wavelength is limited by the surface
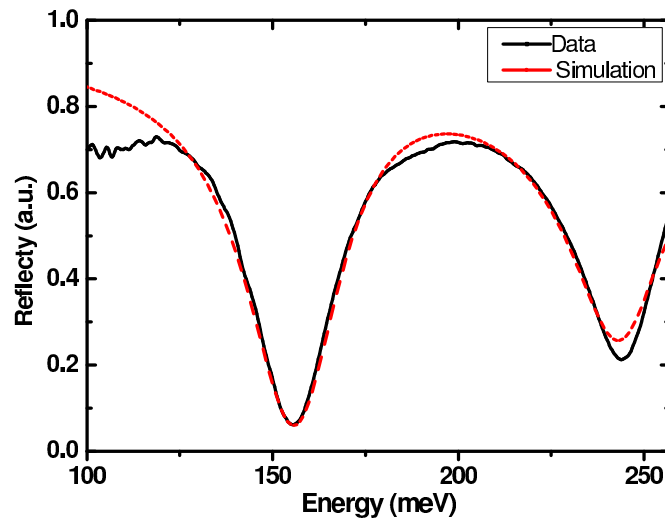
Figure 4.13: Reflectivity spectrum of the two firt cavity modes measured at room temperature for a grating with $s = 0.8\mu m$ and $p = 2.8\mu m$ (black curve). The red dashed line is the corresponding simulation obtained with the modal method formalism.
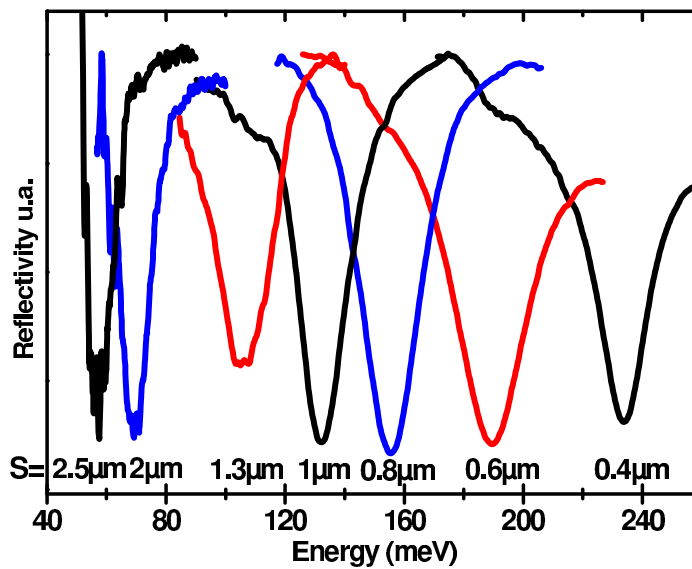
Figure 4.14: Reflectivity spectra for the first order cavity mode measured at room temperature for gratings with s varying from $0.4\mu m$ to $2.5\mu m$.

plasma energy E_{SP} in the metal/semiconductor/metal region. When the cavity mode frequency approaches this limit, related to the maximum oscillation speed of the electrons, its velocity is reduced thus resulting in an increase of the effective index. To illustrate this behavior, we report in figure 4.16 the effective index calculated for a $Au/GaAs$ SPP with a black continuous line. As for our cavity mode, n_{eff} diverges when reaching $\lambda_{SP\ GaAs}$ ($\approx 0.475\mu m$).

One can notice a difference between the effective index of the two cavity mode orders for wavelengths shorter than $10\mu m$; this is due to the overlap of the second order cavity mode with the first diffracted order from the grating given by

$$\lambda = \frac{2p\sin\theta}{l} \tag{4.9}$$

where l is the integer corresponding to the diffracted order.
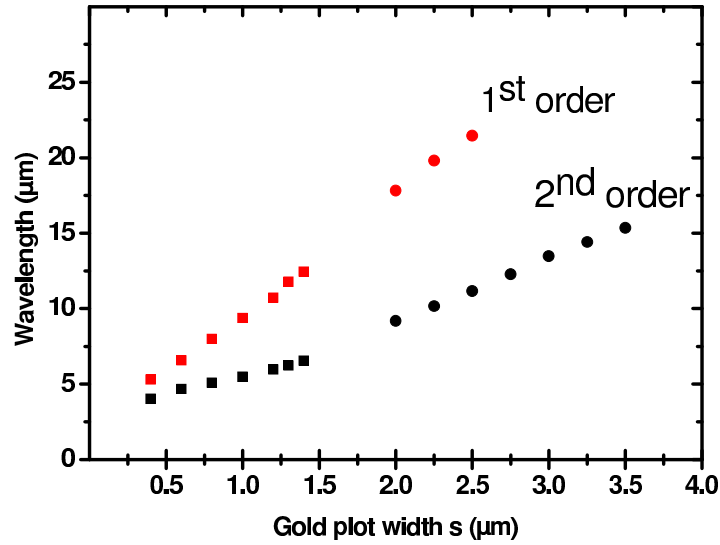
Figure 4.15: Resonant wavelengths for the first order (red symbols) and second order (black symbols) as a function of the strip width s, determined from reflectivity measurements at room temperature. The squares corresponds to samples realized with e-beam lithography while the dots have been realized with optical lithography.

4.4.3   MDM cavity mode and SPP mode coupling

To fully understand the influence of the different parameters on the optical properties of the cavity, we now keep the strip width constant ($s = 0.8\mu m$)
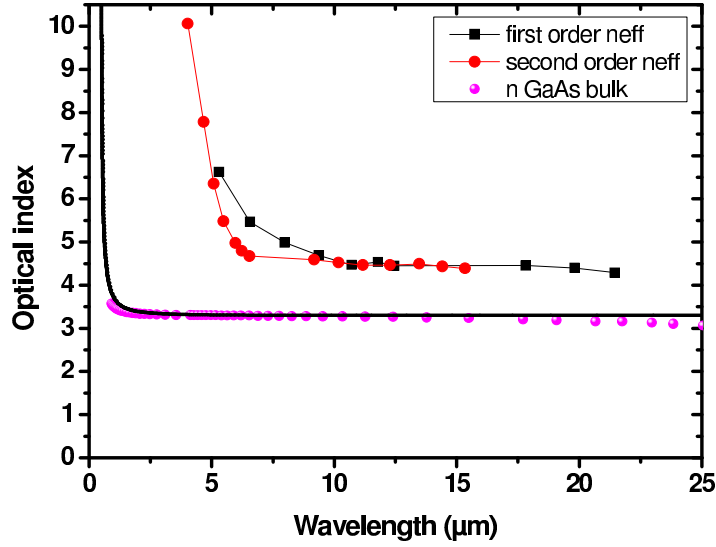
Figure 4.16: Effective index of the first (black squares) and second (red dots) cavity modes as a function of the wavelength deduced from the experimental reflectivity measurements at room temperature by using equation 4.2. The purple curve is the refractive index of the bulk $GaAs$ and the black curve is the effective index calculated for a air-gold SPP.

and vary the period p from $2.3\mu m$ to $4.8\mu m$. The reflectivity spectra and their corresponding simulations are shown in figure 4.17. We clearly observe the first and second order cavity modes (at about $160meV$ and $270meV$ represented with the two vertical black lines), fixed by the width of the strips, plus an additional feature moving in this energy range.

For $p = 2.3\mu m$, only the two cavity modes are visible; for $2.8\mu m$ the additional feature is coupled with the second order mode (slightly changing its energy) and from $3.8\mu m$ up to $4.8\mu m$, it approaches and then passes through the first order cavity mode giving rise to a splitting, which is the signature of a strong coupling regime. Black dashed lines represent the simulated spectra. Figure 4.18 shows a simulation of the vertical component of the electric field in the cavity for a periodicity of $3.8\mu m$ at the energy $E = 190meV$, corresponding to the additional feature (out of resonance with the cavity modes). As we can see, no cavity mode is supported by the metallic strips and a large part of the electric field remains above the grating. We associate this additional feature to a SPP propagating at the surface of the lower planar metallic mirror. As described in section 4.2, changing the periodicity of the grating changes the first Brillouin zone limit $k_x^{Brillouin}$. For the same angle θ the -1 diffracted order of the SPP mode will appear at different energies for different

periodicities. This explains why in figure 4.17, by only changing the distance between the metallic strips, we can tune the SPP energy toward the first order cavity mode. Note that the k_x values we are considering in the different experiences of this work are always relatively small compared to $E_{SP}/\hbar c$ and thus the SPP dispersion is always quite close to the light line or its -1 diffracted order in the first Brillouin zone.
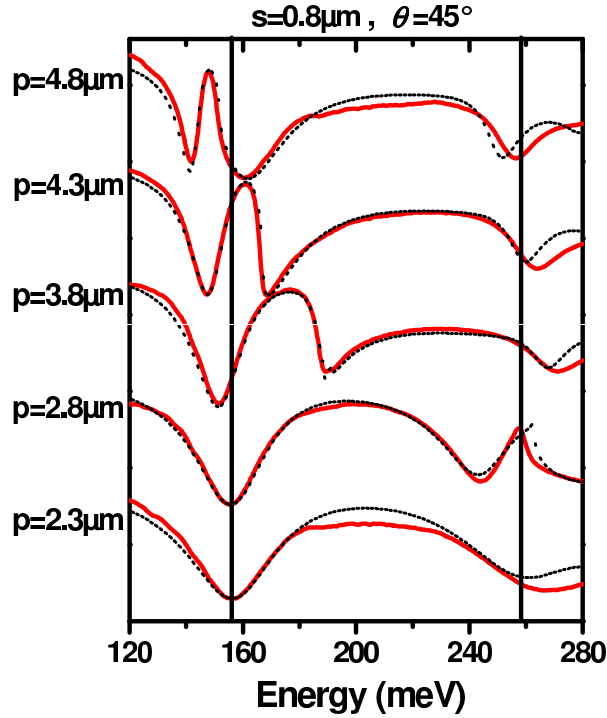
Figure 4.17: Experimental reflectivity spectra (continuous red curves) for structures with strip width $s = 0.8\mu m$ and variable grating period p. The incident angle is $\theta = 45°$. The black doted curves are the corresponding simulated spectra. The black vertical lines indicate the position of the first and second cavity mode.

In order to investigate the SPP and cavity mode energy dispersion as a function of the inplane wave vector, we performed a set of angle resolved reflectivity measurements on two samples with the same $s = 0.8\mu m$ and two different periods, $p = 3.8\mu m$ and $p = 4.8\mu m$. Indeed, by measuring the reflectivity spectra at different angles of propagation in the xOz plane we can tune the k_x component of the wave vector. Reflectivity spectra (red continuous lines) for different angles and the corresponding simulations (black dotted lines) for $p = 3.8\mu m$ are presented in figure 4.19. For this value of the
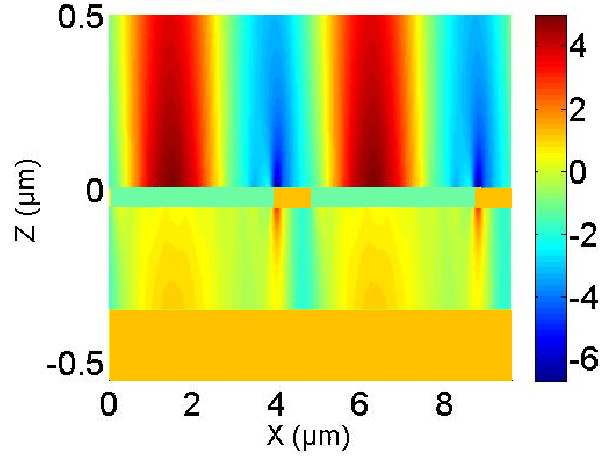
Figure 4.18: Simulation of the vertical electric field (Ez) distribution for the SPP for $s = 0.8\mu m$ and $p = 3.8\mu m$.

grating period the first order cavity mode is never coupled with the SPP, and its energy stays constant with the angle. The positions of the dips, indicated with colored dots are reported in figure 4.20 as a function of the energy and of k_x. The simulated reflectivity spectra are represented in color scale. The green continuous line is the light line and the dashed line is the -1 diffracted orders of the light line in the first Brillouin zone. The conversion from angles to inplane wave vector is obtained once again with

$$k_x = \frac{nEsin\theta}{\hbar c} \tag{4.10}$$

but here we need to consider the air refractive index $n = 1$ because the incoming light couples to the cavity from the air contrarily to Chapter 2 and 3 where the light couples to the cavity mode through the $GaAs$ substrate. We clearly see a dispersion-less cavity mode at approximately $150 meV$ (red squares). We also see a dispersive feature corresponding to the SPP, close to the -1 diffracted order. The second order cavity mode is at about $270 meV$. The simulations well reproduce all those features. One can notice again that the SPP appears always at higher energy than the first order cavity mode in the entire dispersion and thus never couples to it.

   To reach a resonance between the SPP and the first order cavity mode, we need to increase the periodicity in order to increase the first Brillouin zone limit as discussed at the end of section 4.2.2. Therfore, angle resolved measurements and simulations of the sample $p = 4.8\mu m$ are presented in the same way in figure 4.21 and 4.22. On the contrary here, the SPP energy passes

Figure 4.19: Reflectivity spectra (continuous red curves) and corresponding simulations (black dashed curves) for a structure with strip width $s = 0.8\mu m$ and period $p = 3.8\mu m$ for different incident angles θ. The black line gives the first order cavity mode energy and the marks underline the minima positions.
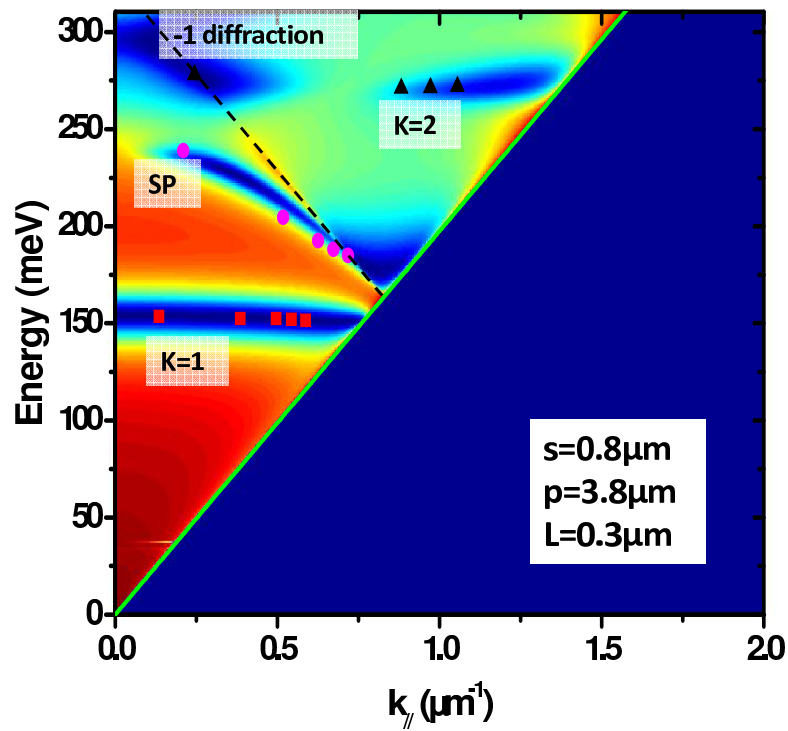
Figure 4.20: Simulated reflectivity (colored contour plot) as a function of the photon energy E and inplane wave vector $k_{/\!/}$ for the grating with $p = 3.8\mu m$. The different marks corresponds to the experimental peaks, the green line is the light line and the dashed line its -1 diffraction order.

through the first cavity mode energy, indicated by the black continuous line in figure 4.21. Figure 4.22 represents the reflectivity spectra as a function of the energy and of k_x. At low k_x the two modes are well separated in energy: the first order cavity mode is at $150meV$ and the SPP at more than $200meV$. While increasing k_x up to $0.6\mu m^{-1}$, the cavity mode energy stays constant and the SPP energy decreases continuously following the -1 diffracted order of the light line. If we go to higher k_x the SPP and the cavity mode energies become resonant and present an anti-crossing. This is the signature of a strong coupling regime between the SPP and the cavity mode. Indeed, the two "branches" exchange their dispersion (the lowest becomes dispersive and the upper becomes dispersion-less) and their FWHM. In our geometry, the two modes spatially overlap in the region below the metallic strips. Because the energy oscillation time between the cavity mode and the SPP is faster than the time for the photon to leave the cavity (due to the metal losses for example), the strong coupling regime is achieved.

In figure 4.23, we represent the simulated spatial dispersion of the E_z component in the cavity for both branches at the anti crossing (for $k_x = 0.75\mu m$). It clearly appears that both the MDM mode under the metal strips and the SPP mode leaking in the air are present. This emphasizes the mixing due to the strong coupling regime between the two modes.

The study of those two samples ($p = 3.8\mu m$ and $p = 4.8\mu m$) shows two different possible configurations for the MDM cavity. By choosing a small periodicity we can achieve a dispersion-less cavity mode. This constant energy as a function of k_x gives rise to a high density of states. It makes the device very suitable to obtain a good efficiency for resonant electrical injection in the polariton states. This is thus the configuration we will exploit in the next chapter to obtain polaritons in MDM cavities. The other possibility is to choose a larger periodicity to couple the MDM cavity mode to a SPP mode. SPP electrical generation or amplification have already been investigated [Babuty et al., 2010]. Furthermore in the past decades, SPPs have been of a great interest for spectroscopy [Liebermann and Knoll, 2000], [Haes and Van Duyne, 2002], [Lal et al., 2007]. Indeed, the sub-wavelength confinement of the electromagnetic field at the surface of a metal allows to reach a very good overlap between the light field and small particles or molecules deposited on the surface. This increases the contrast of the absorption as compared to usual transmission measurements through a solution for example and only needs a small quantity of molecules. The possibility of coupling a SPP with a MDM cavity mode as in our device can be promising to obtain very compact electrically driven spectroscopy systems. Indeed, the idea would be to replace the GaAs region with an active quantum cascade structure to obtain an internal electroluminescent source able to realize
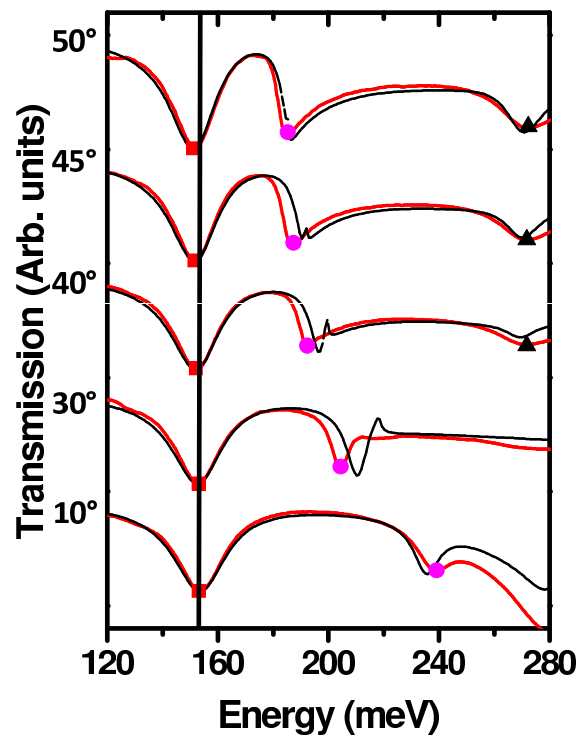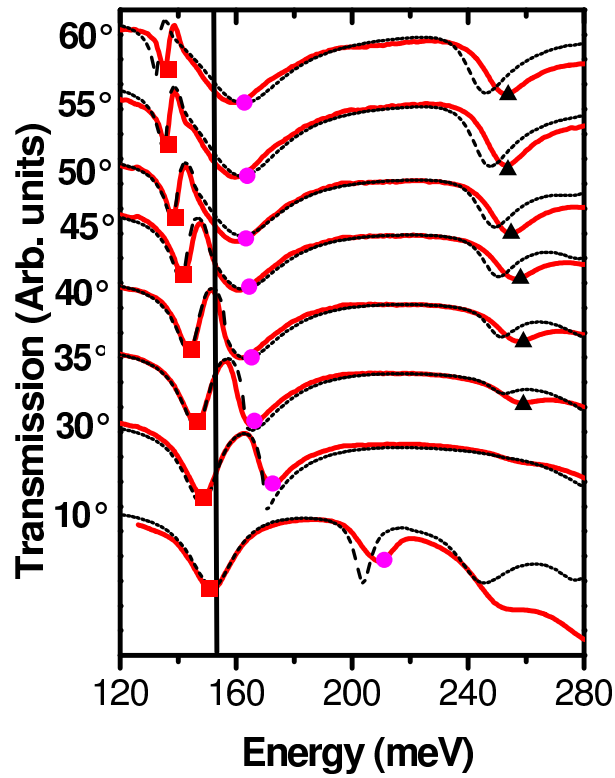
Figure 4.21: Reflectivity spectra (continuous red curves) and corresponding simulations (black dashed curves) for a structure with strip width $s = 0.8\mu m$ and period $p = 4.8\mu m$ for different incident angles θ. The black line gives the first order cavity mode energy and the marks underline the minima positions.
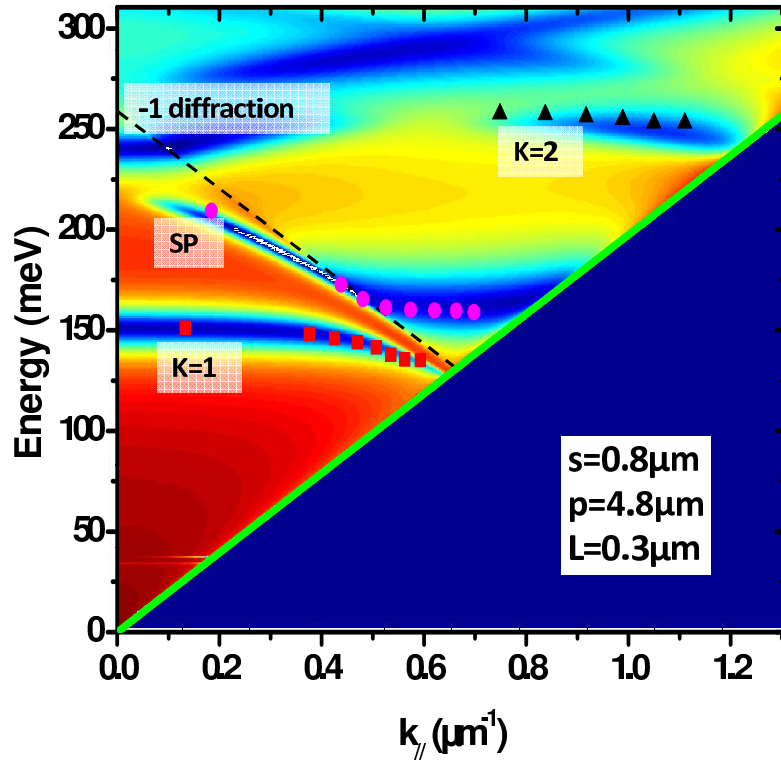
Figure 4.22: Simulated reflectivity (colored contour plot) as a function of the photon energy E and inplane wave vector $k_{/\!/}$ for the grating with $p = 4.8\mu m$. The different marks corresponds to the experimental peaks, the green line is the light line and the dashed line its -1 diffraction order.
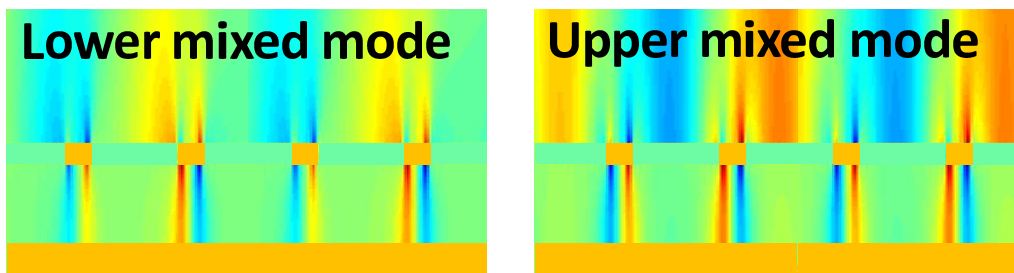
Figure 4.23: Simulation of the vertical electric field (Ez) distribution for the lower (left panel) and upper (right panel) mixed modes when the first cavity mode and the SPP are at resonance.

the spectroscopy of molecules deposited on top of the sample. This system presents the most compact geometry as the light source is directly below the surface where the molecules are deposited. Our cavities designed for the MIR domain fits especially well this purpose considering that most of the molecules present vibrational energies in this part of the electromagnetic spectrum.

4.5   Conclusion

I presented in this chapter our results that demonstrate the feasibility of MDM cavities in the MIR domain. After a brief description to explain the nature of the light confinement I discussed the impact of the different parameters of the gratings on the cavity modes. The first step was to prove the tunability of the cavity energy over a broad range of wavelengths (from $5\mu m$ to $20\mu m$) by changing the metallic strip width of only $2\mu m$. The second part showed the presence of SPP mode for certain periodicity of the grating. An angle resolved study of two samples allowed to prove the existence of two possible configurations: a dispersion-less cavity, as well as a strong coupling between the MDM cavity mode and the SPP.

To conclude this chapter, I would like to describe practical advantages of MDM cavities. First of all, with this geometry, we directly access to the cavity mode from the free space. Therefore there is no loss of intensity due to Fresnel refraction on a facet nor from absorption in a substrate. From an experimental point of view, the measurements alignment can be simplified by adapting the grating dimensions. For our studies we processed gratings on surfaces from $0.2mm \times 0.2mm$ to $2mm \times 2mm$. Additionally, for dispersion-less cavities, we can measure the spectra from any angle θ. On another hand, because the cavity energy depends only on the grating parameters, it is possible to realize a large number of cavities with different mode energies on a single epitaxially grown sample. This allows to keep the exact same growth condition for the different cavities tested. Finally, it is always possible to find a set of parameters to have the cavity mode at resonance for a certain energy. It will be convenient in the next chapter where the AR will be filled with QWs whose intersubband transitions can be shifted from the requested energy due to growth problems for example.

Moreover, MDM cavities present two fundamental advantages for intersubband polaritons. One is the small cavity thickness which increases the Rabi frequency as $1/\sqrt{L}$. As we demonstrated here, highly sub wavelength cavities support confined modes (our cavities are only $300nm$ thick for a wavelength between $5\mu m$ and $20\mu m$). The other point concerns the dispersion-less character of the modes that gives rise to a high density of states. Indeed the

flat dispersion is expected to facilitate the selectivity of the electrical resonant injection and thus to increase the injection efficiency into polariton states by avoiding the dark states mentioned in 3.6.

Chapter 5

Ultra-strong coupling

Contents

5.1   Introduction

As described in chapter 1, the Rabi splitting is proportional to $1/\sqrt{L}$; with a cavity length of only few hundreds of nm, the MDM cavities presented in the previous chapter are thus very good candidates to obtain a large Rabi splitting. This would allow us to increase the energy separation between the polaritonic branches and the dark states, and finally increasing the quantum efficiency of the electroluminescence.

In this chapter I will study the strong coupling between the fundamental mode of a MDM cavity and an intersubband excitation of a two-dimensional electron gas (2DEG). The chapter is organized as follows: I will shortly describe the three samples studied here and show their characteristics without the double metal cavity. Then I will present the reflectivity measurements on the devices and the polaritonic dispersions deduced from them. I will show that a photonic gap appears in the dispersion, which is the signature of the ultra-strong coupling regime for our system. Finally I will demonstrate that

the spectra are independent on the measurement angle. The main results presented in this chapter have been published in [Jouy et al., 2011b].

5.2   Sample description and ISB transition characteristics

To optimize the strong coupling our MDM cavity was completely filled with QWs. This means that the number of periods (which corresponds to a QW and one of its barriers) is directly proportional to the cavity length chosen. As the Rabi splitting frequency is proportional to $\sqrt{1/L_P}$ as described in section 1.3.2, it should thus stay constant for any cavity length. Nevertheless, as represented in the left panel of figure 5.1, we need one more barrier than the number of periods and $GaAs$ claddings on both sides of the AR. Those do not contribute to the strong coupling and occupy a larger fraction of the cavity when the number of periods decreases. As a result, the Rabi splitting changes as a function of the cavity length. It is convenient at this point to introduce the *filling factor* f_w which corresponds to the spatial overlap between the quantum well and the cavity mode and is thus proportional to the square of the Rabi splitting. In the right panel of figure 5.1, the black curve plots the calculated filling factor for our structure as a function of the number of periods in the cavity (i.e. as a function of the cavity length). We can see that it changes drastically for few periods before reaching an almost constant value after about ten periods. Therefore, we chose to grow ten periods in our structure to both obtain a large splitting and a small cavity volume (only $259nm$). The red and blue dashed lines correspond to the filling factor for $AlGaAs$ barriers respectively thinner ($10nm$) and thicker ($20nm$) than the one we chose. As expected, the smaller the barriers, the best the filling factor. We opt for $14nm$ thick barriers as it is the thinnest value for which the wave functions of neighboring quantum wells are not coupled.

The AR is thus made of ten $GaAs/Al_{0.35}Ga_{0.65}As$ QWs with $9nm$ thick $GaAs$ wells and $14nm$ thick $AlGaAs$ barriers. A $10nm$ $GaAs$ cladding is used to avoid the oxidation of the last barrier, while a $5nm$ cladding is used to allow the HF chemical attack of the stop layer without removing the first barrier. The total thickness of the semiconductor region is $259nm$. It is embedded in a MDM cavity as shown in figure 5.2. To study the effect of the electronic density on the strong coupling, we realized three samples which only differ by their doping levels. Samples HM2892 and HM2951 have been delta doped in the middle of the barriers while sample HM2952 is Si doped in the barriers for a length of 12 nm ($1nm$ on each side is kept undoped to limit the diffusion of defects in the well that would result in a broadening
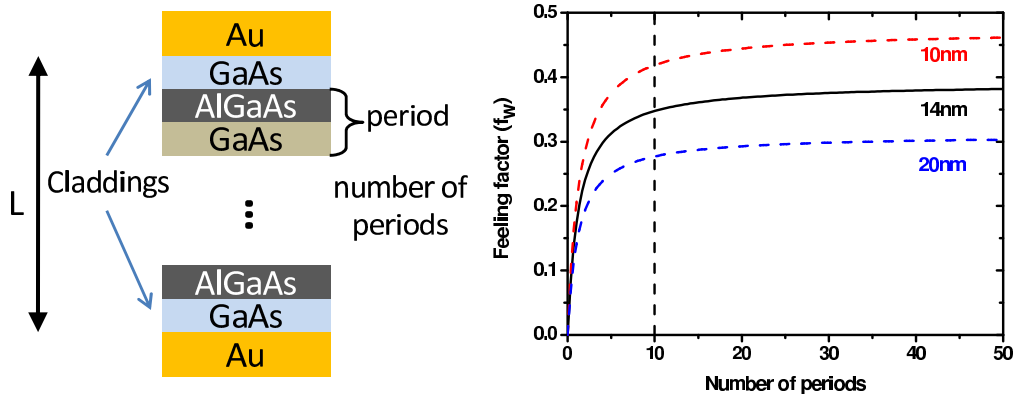
Figure 5.1: Calculated filling factor as a function of the number of periods in the cavity for $14nm$ (black curve), $10nm$ (red dashed curve) and $20nm$ (blue dashed curve) thick $AlGaAs$ barriers. The black dashed line indicates the number of quantum wells that we chose.
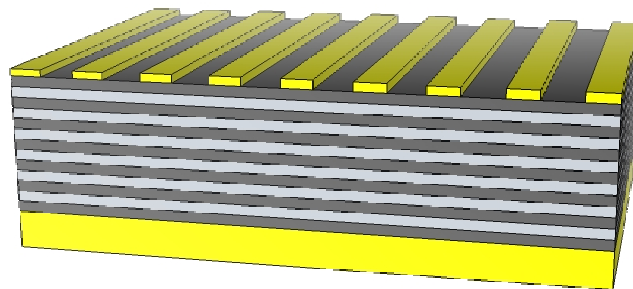
Figure 5.2: Scheme of our MDM cavity with the QWs in the AR.

of the intersubband transition). Shubnikov-de Haas measurements have been performed at $1.5K$ and gave the following electronic densities: $8.10^{11}cm^{-2}$ (HM2892), $1.5.10^{12}cm^{-2}$ (HM2951) and $3.10^{12}cm^{-2}$ (HM2952).

In order to obtain the intersubband transition energies, we realized absorption measurements on the samples before the wafer bonding. A gold mirror was deposited on top of the AR and samples were polished for measuring the transmission in the multi pass geometry. The spectra are shown in figure 5.3 at room temperature for HM2892 (black line), HM2951 (red line) and HM2952 (blue line). Two behaviors appear. First, the integrated absorption intensity increases with the electronic density. And second, while the absorption maximum is at $108.5meV$ for the two lowest electronic densities, it moves at higher energy for HM2952 ($112.5meV$). The increase of the integrated absorption in-
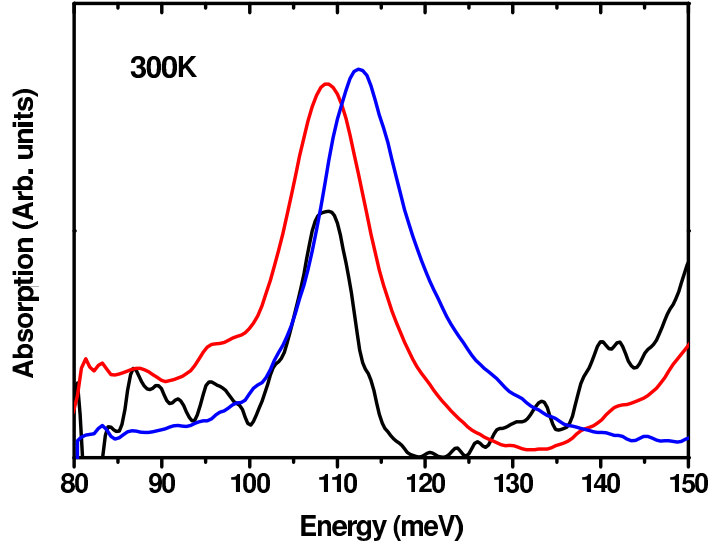
Figure 5.3: Experimental absorption spectra at room temperature for HM2892 (black curve), HM2951 (red curve) and HM2952 (blue curve).

tensity is due to the increase of electron density in the fundamental state of the QW. The energy shift is well explained by taking into account the depolarization shift (or plasma shift) of the intersubband transition introduced in section 1.2.2. The effect is the renormalization of the absorption energy toward higher values as

$$\tilde{E}_{21} = \sqrt{E_{21}^2 + E_p^2} \quad \text{with} \quad E_p = \hbar\omega_p = \hbar\sqrt{\frac{Ne^2}{\varepsilon_0 m^*}} \tag{5.1}$$

where E_{21} is the bare transition energy in the QW expected to be $105meV$

and E_p is the plasma energy. Figure 5.4 shows the simulated spectra corresponding to figure 5.3. They have been calculated by Aymeric Delteil for the different doping levels taking into account the collective character of the intersubband transition through the depolarization shift. Those simulations have been realized with the same bare ISB transition energy ($105meV$) and a FWHM of $8meV$ for HM2892 and HM2951 and of $13meV$ for HM2952 to reproduce the width in the data and by using the electronic densities obtained from Shubnikov-de Haas measurements. The comparison with the data shows that a good agreement is obtained for the relative absorption intensity of the three samples. The resonance position correspond as well for the two highest electronic densities sample but not for the sample HM2892 where the resonance is expected to be at lower energy ($105.5meV$ in the simulation instead of $108.5meV$ in the data). We attribute this difference to the uncertainty on the well width due to growth that can give a slightly different intersubband transition energy for two samples with the same growth sheet but grown separately.
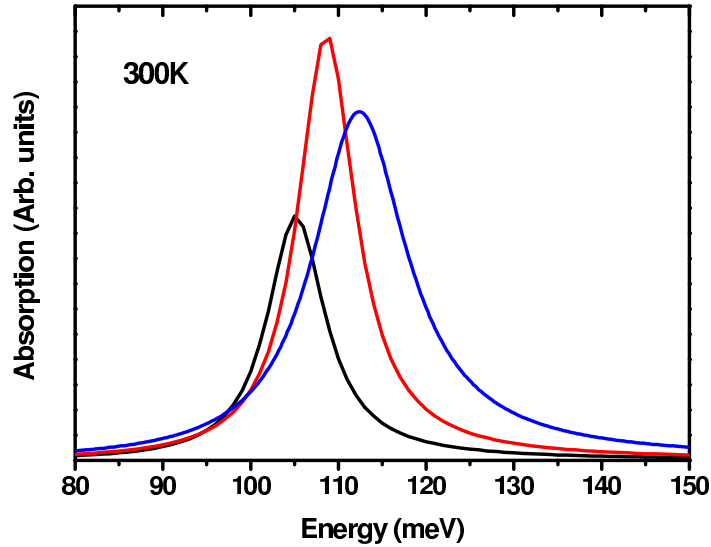
Figure 5.4: Simulated absorption spectra at room temperature for HM2892 (black curve), HM2951 (red curve) and HM2952 (blue curve).

Figure 5.5 represents the absorption spectra for the sample HM2952 measured at $77K$ (blue line) and $300K$ (black line). While at room temperature the absorption is peaked at $112.5meV$, it shifts to $114.5meV$ at $77K$ and the maximum intensity changes. It is well reproduced on the simulations (red dots) as they take into account the variation of the semiconductors gap as a

function of the temperature. At room temperature the gap decreases and as a result of the interactions between the bands (taken into account in the $\vec{k} \cdot \vec{p}$ model used here) the intersubband transition is shifted to lower energy.
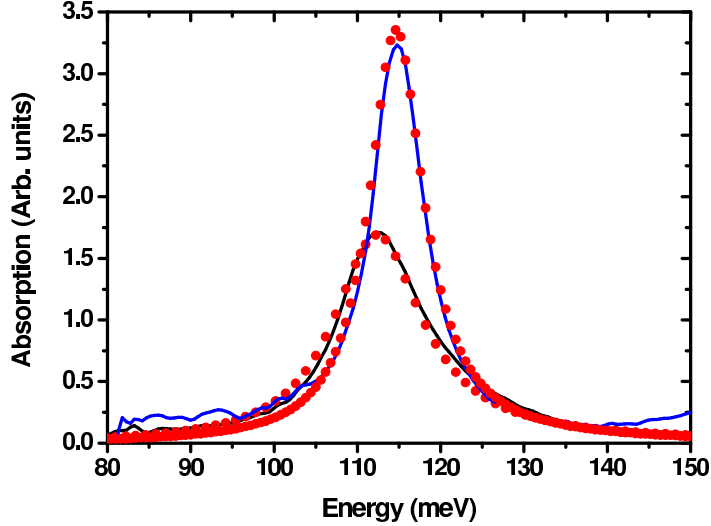
Figure 5.5: Experimental (continuous blue and black curves) and simulated (red dots) absorption on HM2952 at $77K$ and $300K$.

Note that the FWHM in this simulation is manually changed from $8meV$ at $77K$ to $13meV$ at $300K$ to fit the experimental spectra width but the ratio of the maximum absorption value between the two temperatures is directly obtained with the simulation as well as the shape (slightly asymmetric for $300K$) and perfectly reproduces the data.

5.3   Strong coupling

In this section I will focus on samples HM2892 and HM2951 for which the plasma energy contribution is negligible ($\tilde{E}_{21} \approx E_{21}$). A series of MDM cavities with different gratings have been realized. The metallic strip width vary from $0.6\mu m$ to $2\mu m$ while ($p-s$) is kept constant and equal to $1.5\mu m$. Reflectivity measurements were performed at room temperature for $\theta = 10°$ and are summarized in figure 5.6 (top panel for HM2892 and bottom panel for HM2951) which represent the reflectivity spectra for the different values of s. The transmission spectra corresponding to the absorption shown in figure 5.3 is represented here by black dashed line for each sample. The spectra

are offset for clarity. We can observe two peaks moving as the cavity energy is tuned through the variation of the strip width s. For both samples, an anti-crossing of the two branches is clearly visible.
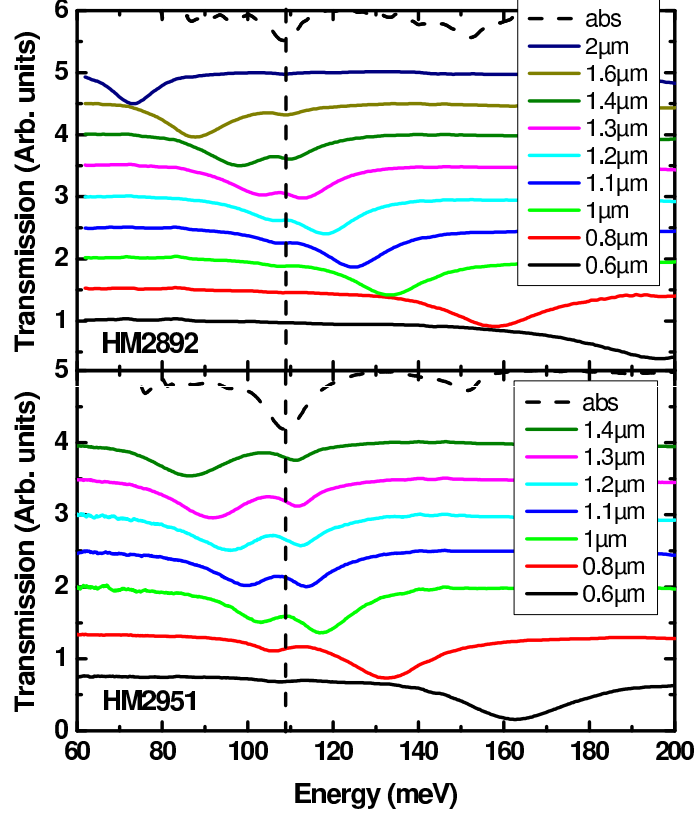
Figure 5.6: Reflectivity spectra measured for samples HM2892 (top panel) and HM2951 (bottom panel) at $300K$ for different values of the strip width. The period p is $1.5\mu m$. The spectrum in dashed line presents the transmission measured at $300K$ on an unprocessed sample in the multipass geometry.

   In figure 5.7 we show the peaks energy obtained from figure 5.6 (black dots) as a function of the cavity mode energy (E_{cav}). E_{cav} is deduced for each value of s from the measurements realized on the empty cavity in the previous chapter. Because the cavity thickness is not exactly the same here and because of the uncertainty on s for each e-beam lithography (it has been realized separately for the empty cavity, HM2892, HM2951 and HM2952), we slightly adjusted E_{cav} to obtain the minimum value of the splitting for $E_{cav} = \tilde{E}_{21}$. The corresponding correction on s is of $57nm$ for HM2892 and of $230nm$ for HM2951. The polariton branches present the expected dispersion, showing an anticrossing when the cavity mode energy becomes resonant with

the intersubband transition one. The blue stars represent the absorption energy obtained in figure 5.3 with no cavity mode. The red curves represent

Figure 5.7: Reflectivity minima at 300 K (bullets), plotted as function of the cavity mode energy. The continuous line is the simulated polariton dispersion, following equation 5.2. The dashed horizontal lines are the asymptotes of the polariton branches. The star indicates the ISB absorption measured from transmission experiments at 300 K on an unprocessed sample. The top panel concerns the sample HM2892 while the bottom panel concerns the sample HM2951.

the calculated polaritonic dispersion given by equation 1.19:

$$E_\pm = \frac{E_{21} + E_c \pm \sqrt{(E_{21} - E_c)^2 + (2\hbar\Omega_R)^2}}{2} \qquad (5.2)$$

where E_+ is the upper polariton branch and E_- the lower polariton branch energy. They correspond to the solutions of the strong coupling equation

$$(E - E_{21})(E - E_c) = (\hbar\Omega_R)^2 \qquad (5.3)$$

The dashed black line represents the intersubband transition energy and corresponds to the asymptote of both polaritonic branches. As E_{21} is deduced from the absorption measurements, the only adjustable parameter for the calculated dispersions is the Rabi frequency. The best correspondence is obtained with $2\hbar\Omega_R = 9.5meV$ for HM2892 and $2\hbar\Omega_R = 14meV$ for HM2951 (those values are reported in table 5.1). The same samples have been characterized at $77K$ and their energy dispersions are presented in figure 5.8. In this case the Rabi splitting is slightly larger ($11.5meV$ for HM2892 and $16meV$ for HM2951). This is due to the thermal population of the excited level of the ISB transition at higher temperature. Indeed, at room temperature approximately 5% of the electrons in the QW are on the level 2; on the contrary, this value becomes less than 0.1% at $77K$. As the splitting is proportional to the square root of the electronic density difference between the fundamental and excited state, it becomes greater at $77K$.

The study of those two samples demonstrated the strong coupling regime in MDM cavities for the mid-infrared and confirmed the dependance of the Rabi splitting on the electronic density.
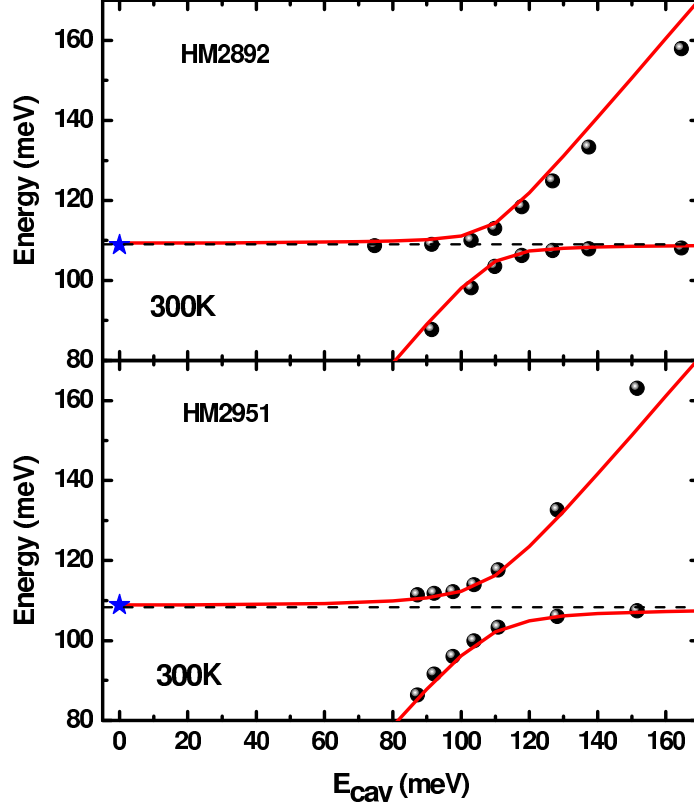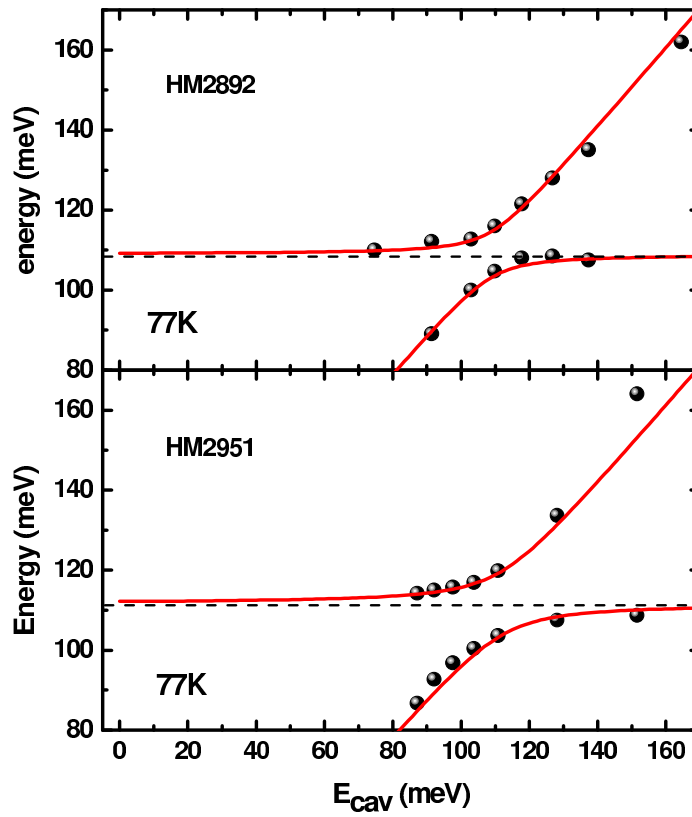
Figure 5.8: Reflectivity minima at $77K$ (bullets), plotted as function of the cavity mode energy. The continuous line is the simulated polariton dispersion, following equation 5.2. The dashed horizontal lines are the asymptotes of the polariton branches. The top panel concerns the sample HM2892 while the bottom panel concerns the sample HM2951.

5.4 Ultra-strong coupling

In this section I present the results of reflectivity measurements on the sample with the highest electronic density (HM2952). As in the previous section, s is tuned from $0.4\mu m$ to $1.4\mu m$ and $(p-s)$ is kept constant and equal to $1.5\mu m$. Figure 5.9 shows the reflectivity spectra at room temperature for the different metallic strip widths (color curves) and the transmission spectrum obtained without cavity (black dashed curve). The spectra are shifted for better clarity and a black dashed line underlines the bare absorption position.
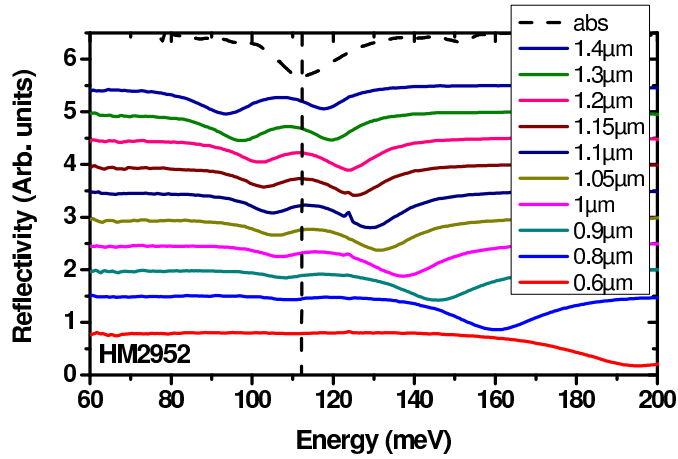
Figure 5.9: Reflectivity spectra measured for sample HM2952 at $300K$ for different values of the strip width. The period p is $1.5\mu m$. The spectrum in dashed line presents the transmission measured at $300K$ on an unprocessed sample in the multipass geometry.

The energy of the two polaritonic peaks for each spectrum of figure 5.9 is plotted as a function of the cavity mode energy in figure 5.10 (black dots). The blue star corresponds to the bare intersubband transition energy obtained in figure 5.5. The two branches present an important anti-crossing as the minimum splitting is $2\hbar\Omega_R = 21.5meV$.

When the Rabi splitting represents an important fraction of the intersubband transition energy, the so called *ultra strong coupling* regime is achieved. In this case, unlike for HM2892 and HM2951, the experimental polaritonic dispersion does not match the calculations with equation 5.2. As in [Todorov et al., 2010a], one needs to solve the following eigenvalue equation resulting from the complete Hamiltonian of the system, including the quadratic term, which accounts for the polarization self-interaction, and the

Figure 5.10: Reflectivity minima at 300 K (bullets), plotted as function of the cavity mode energy for the sample HM2952. The continuous red line is the simulated polariton dispersion, following equation 5.5. The dashed horizontal lines are the asymptotes of the polariton branches. The star indicates the ISB absorption measured from transmission experiments at 300 K on a sample without cavity.

anti-resonant terms [Ciuti et al., 2005]

$$(E^2 - \tilde{E}_{21}^2)(E^2 - E_c^2) = 4(\hbar\Omega_R)^2 E_c^2 \tag{5.4}$$

The two polariton branches energy dispersion is thus given by

$$E\pm = \sqrt{\frac{E_c^2 + \tilde{E}_{21}^2 \pm \sqrt{(E_c^2 - \tilde{E}_{21}^2)^2 + 4(2\hbar\Omega_R)^2 E_c^2}}{2}} \tag{5.5}$$

Contrarily to equation 5.2, the minimum splitting does not occur for $E_c = \tilde{E}_{21}$ but for $E_{c\,min} = E_{21}\sqrt{1 + \frac{E_p^2}{E_{21}^2}(1 - f_w)}$ where $f_w = (2\hbar\Omega_R)^2/E_p^2$ is the spatial overlap between the quantum well and the cavity mode. In our sample f_w is equal to 0.35. $E_{c\,min}$ corresponds as well to the asymptote of the lower polariton branch for $E_c \gg E_{21}$. In the opposite limit, the upper polariton branch energy reaches the value $\tilde{E}_{21}$ for $E_c \ll E_{21}$. These two different values for the asymptotes (represented with black dashed lines on the figure) indicates the opening of a photonic gap between the two polaritonic branches. The parameters for the calculated polaritonic dispersion (red lines in figure 5.10) are directly obtained from the data. Indeed, the plasma energy E_p is extracted from the minimum splitting value that corresponds to $2\hbar\Omega_R$ (The

Rabi frequency is related to f_w and to the plasma energy by $2\hbar\Omega_R = \sqrt{f_w}E_p$) while the bare intersubband transition energy is inferred from the value of E_{min} obtained with the lower polariton asymptote. From those, we can deduce $\tilde{E}_{21}$ and conveniently check it with the upper polariton asymptote value. We estimate the electronic population difference between the two subbands from the plasma energy (see equation 5.1). For this sample at room temperature we obtain $N_1 - N_2 = 8.5.10^{11}cm^{-2}$ while we expect a value of $2.3.10^{12}cm^{-2}$ at $300K$ using the equation:

$$N_2(T) = \frac{m^*k_BT}{\pi\hbar^2}\ln\left[1 + \exp\frac{-(E_2 - E_F)}{k_BT}\right] \tag{5.6}$$

where E_{Fermi} is the Fermi energy, k_B is the Boltzmann constant and T is the temperature. This discrepancy was already observed in the literature [Geiser et al., 2010] and it can be due to the localization of a fraction of the electrons in defects originated from the wafer bonding process.

Measurements realized at $77K$ are summarized in figure 5.11. As for samples HM2892 and 2951, the Rabi splitting slightly increases compared to the room temperature value and is of $23.5meV$.
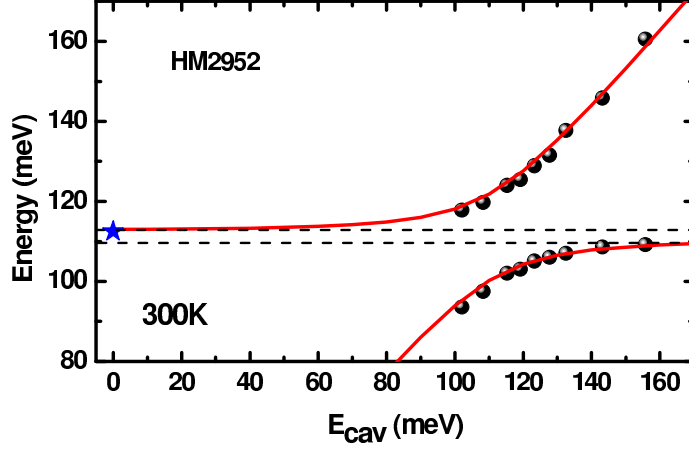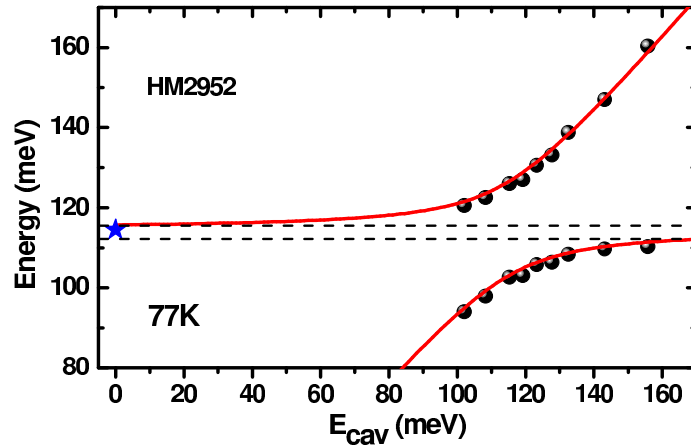

Figure 5.11: Reflectivity minima at $77K$ (bullets), plotted as function of the cavity mode energy for the sample HM2952. The continuous line is the simulated polariton dispersion, following equation 5.5. The dashed horizontal lines are the asymptotes of the polariton branches. The star indicates the ISB absorption measured from transmission experiments at $77K$ on a sample without cavity.

Table 5.1 summarizes all the relevant parameters obtained for the three samples at room temperature and $77K$. As expected, the value of the Rabi

splitting increases as the square root of the electronic density in the sample even if only a part of the electrons seems to be available on the electronic states of the QW. With the different doping concentration used, we have been able to achieve the strong coupling regime for the two smallest electronic densities and to reach the ultra-strong coupling regime for the last sample with a ratio $\hbar\Omega_R/E_{21} = 0.1$ at room temperature.

	n_s Shubnikov-de Haas ($10^{12}cm^{-2}$)	n_s effective ($10^{12}cm^{-2}$)	$\tilde{E}_{21}$ (meV)	$2\hbar\Omega_R$ (meV)	E_g (meV)
HM2892	0.8	0.27 (0.35)	108.9 (108.6)	9.5 (11.5)	0.4 (0.6)
HM2951	1.5	0.53 (0.7)	108.9 (111.6)	14 (16)	0.9 (1.2)
HM2952	3	1.3 (1.5)	112.5 (114.5)	21.5 (23.5)	2 (2.62)

Table 5.1: Summary of the different parameters obtained from the fit of the data for the three different samples. For the four last columns, the values in () are for $77K$ while the others are for $300K$.

The energy gap is given by

$$E_g \approx f_w(\tilde{E}_{21} - E_{21}) = \frac{(2\hbar\Omega_R)^2}{2E_{21}} \tag{5.7}$$

E_g is proportional to the difference between the ISB transition energy renormalized by the plasma energy (which is only visible for high electronic densities) and the bare ISB transition energy times the overlap factor. It is also proportional to the ratio between the Rabi splitting and the bare intersubband transition energy $2\hbar\Omega_R/E_{21}$. When this ratio is of the order of 1, the ultra-strong coupling regime is achieved. The opening of a photonic gap between the polariton branches in our experimental data can be considered as the signature of the ultra-strong coupling regime. Indeed, it is only observable if of the order of few meV due to the broadening of our ISB transition and our cavity mode which are both of $\Gamma_{21} \approx \Gamma_c \approx 10meV$. Following equation 5.7, an energy gap of $2.5meV$ corresponds to a ratio $E_p/E_{21} \approx 0.35$ which is clearly in the ultra strong coupling regime according to figure 1.4. The energy gap is represented as a function of the Rabi splitting in figure 5.12. The black curve is calculated following equation 5.7 for $E_{21} = 110meV$ and the values for the three samples studied in this chapter are marked with black square for room temperature and red circles for $77K$ measurements.
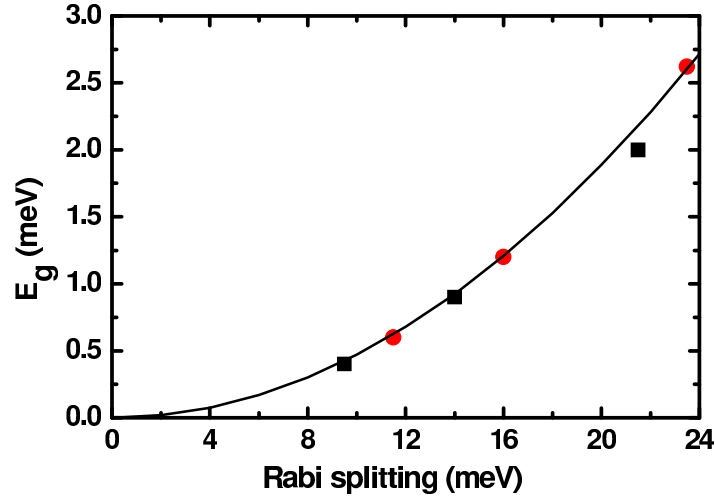
Figure 5.12: Energy gap as a function of the Rabi splitting. The continuous black curve corresponds to the calculation while the black squares (red dots) correspond to the experimental values at $300K$ ($77K$).

5.5 Angular dependance of the spectra

On the sample HM2952, we chose the grating where the cavity mode energy is at resonance with $E_{c\,min}$ ($s = 1.2\mu m$) to perform angle resolved measurements. This allows us to obtain the polariton dispersion as a function of the wave vector components k_x or k_y.

First we only vary the incidence angle θ in the xOz plane. Figure 5.13 shows the measured spectra for different angles (from 10° to 55°) arbitrarily shifted; the two peaks corresponding to the two polariton branches are clearly visible. The energy minima stay constant with the incidence angle. Figure 5.14 shows the energy dispersion as a function of k_x. The grey scale is the simulated absorption coefficient and the white dots are the absorption peaks extracted from the spectra. The simulated and the experimental results are in a good agreement: the system presents a flat energy dispersion as a function of k_x. This is consistent with results found in chapter 4 in which a similar value of $(p - s)$ gave a dispersion-less cavity mode.

We now change the angle in the direction along the metallic strips (in the yOz plane) from 10° to 50°. The spectra are presented in figure 5.15 and are arbitrarily shifted for better clarity. Those results are summarized in figure 5.16 where the polaritonic absorption peak energy is plotted as a function of k_y (black dots). We observe a slight increase of the energy of the two branches
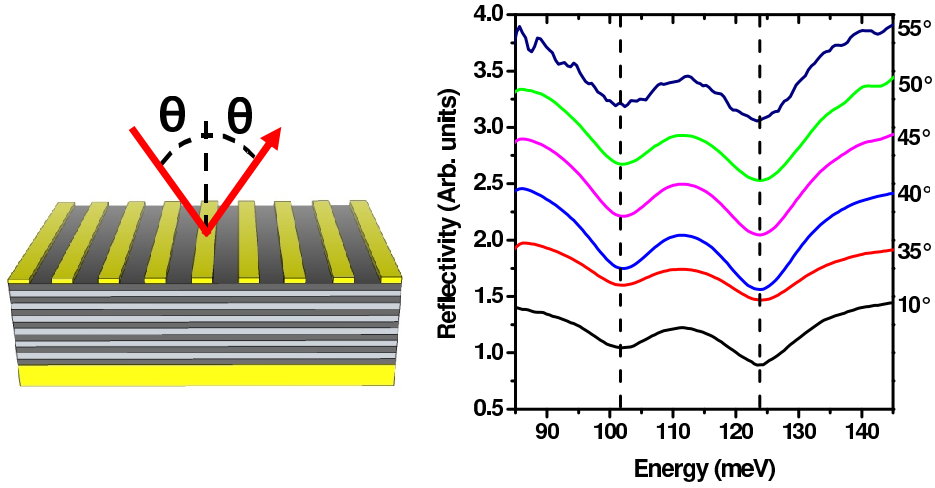
Figure 5.13: Reflectivity spectra measured for sample HM2952 at $300K$ for different values of the θ in the xOz plane. The strip width s is $1.2\mu m$ and the period p is $1.5\mu m$.
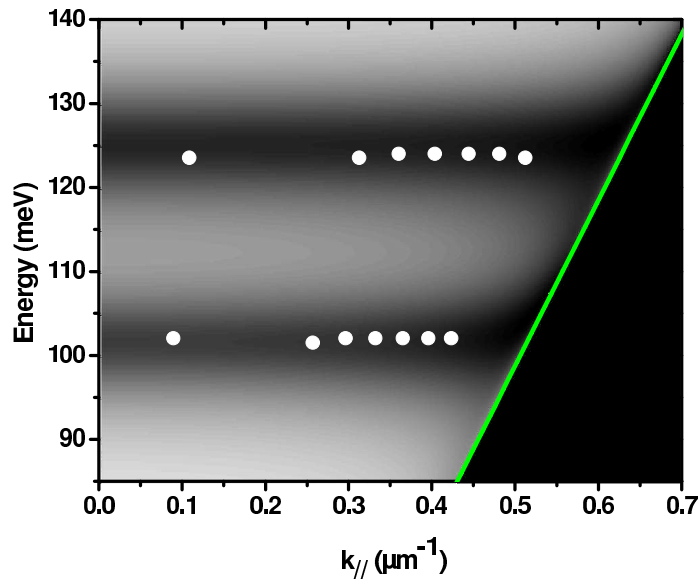
Figure 5.14: Reflectivity minima (white dots) and simulated reflectivity (gray scale) as functions of k_x for $s = 1.2\mu m$; the line represents the light cone.

(less than $2meV$) for the highest values of k_y compared to the lowest one. The cavity mode energy is given by

$$E_c = \frac{\hbar c}{n_{eff}} \sqrt{k_{x\,cav}^2 + k_y^2} \qquad (5.8)$$

where $k_{x\,cav}$ is the component of the wave-vector in the x direction. The calculated energy dispersion for a cavity with $s = 1.2\mu m$ is plotted in red continuous line in the figure. It is clear that, while the cavity mode is confined in the x direction thanks to the metallic strips, no confinement occurs in the y direction (in this direction the strips are $\approx 800\mu m$ and are thus very long compared to the photon wavelength). Therefore, the energy contribution in the y direction can be tuned. Nevertheless, the maximum values of k_y reachable in the experience (limited by the light line) is of the order of $0.6\mu m^{-1}$ for cavities wave vector along the x axis ($k_{x\,cav} = E_c n_{eff}/\hbar c$) around $2.5\mu m^{-1}$. The contribution of k_y is small compared to $k_{x\,cav}$ and thus does not affect much the cavity mode energy. In particular the energy shift with k_y is smaller than the linewidth of the polariton states.
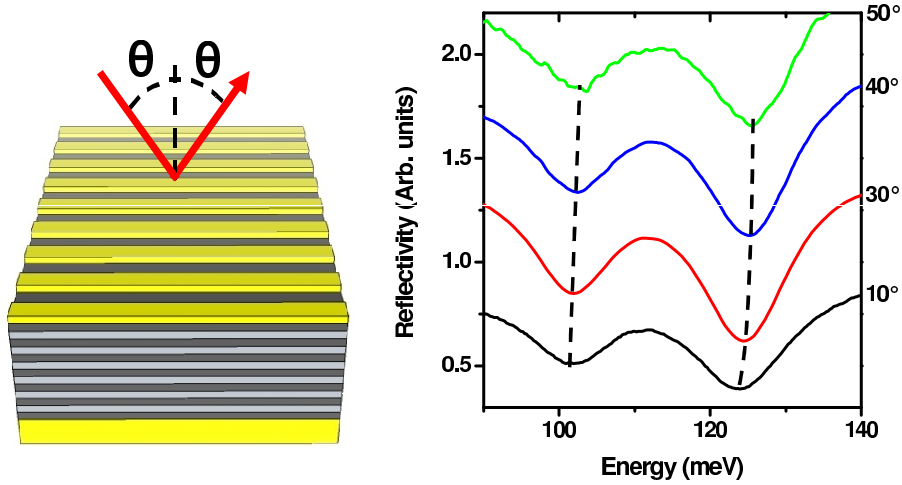
Figure 5.15: Reflectivity spectra measured for sample HM2952 at $300K$ for different values of the θ in the yOz plane. The strip width s is $1.2\mu m$ and the period p is $1.5\mu m$.

Furthermore, as far as concern the electrical injection, our cavity can be considered as dispersion-less. Indeed, the electronic injector FWHM is at least of the order of $5meV$ for our energy range; a shift of only $2meV$ will therefore not affect much the resonant electrical injection.
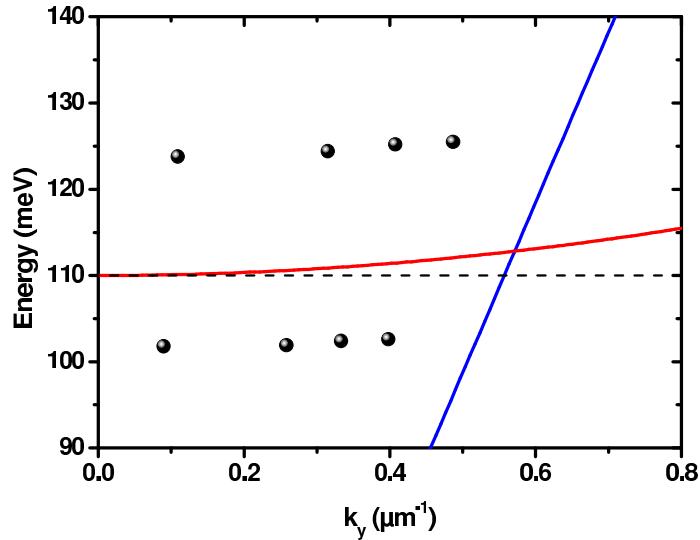
Figure 5.16: Reflectivity minima measured at $300K$ (black dots) as functions of k_y for $s = 1.2\mu m$. The red curve is the calculated dispersion for a cavity mode with an energy of $110meV$ for $k_y = 0$; the blue line represents the light cone.

5.6   Conclusion

Our strategy to maximize the strong coupling was to use highly subwavelength cavities to strongly confine the photonic mode. Three samples have been studied, with different doping level, and allowed to demonstrate strong coupling regime. For the sample with the highest electronic density, the measured Rabi splitting of $21.5meV$ at room temperature represents an important fraction of the intersubband transition energy ($\hbar\Omega_R/E_{21} = 0.1$). In this condition, the energy dispersion showed the opening of a photonic gap energy between the two polariton branches, signature of the ultra-strong coupling regime.

Angle resolved reflectivity measurements both in x and y directions allowed to demonstrate the flat energy dispersion of the polaritons in our samples. This gives rise to a high density of photonic states, very suitable for resonant electrical injection in the polaritonic states.

Chapter 6

Conclusions and perspectives

Contents

In this chapter I will summarize the main results obtained during my PhD and draw some conclusions on this work. The second part of the chapter will be devoted to perspectives and future projects related to my work.

6.1 Conclusions

My PhD work was devoted to the design, realization and characterization of mid-infrared electrically injected devices operating in the light-matter strong coupling regime. I first studied an electroluminescent device, based on a quantum cascade structure inserted in a planar microcavity. It was first characterized by reflectivity measurements, to obtain the polariton dispersion. My PhD work has started by emphasizing the importance of the correct representation of the energy vs the wave vector diagram (the "k space")to obtain the correct value for the Rabi frequency. In this device a Rabi splitting of $2\hbar\Omega_R \approx 13 meV$ was measured. The sample was then characterized by angle resolved electroluminescent measurement, in order to understand how the polariton states are populated by an electrical current. I showed that the electroluminescence spectra are obtained as the product of the optical density of states, given by the reflectivity spectra, times a function describing the occupation of the polariton states. The study of EL for a fixed voltage of the polaritonic and a reference sample allowed us to relate the occupency of the polariton states to the injector of the quantum cascade structure. By varying

the applied voltage, we showed a tunability of the emission from the polariton states from $\approx 140meV$ up to $\approx 160meV$ in a structure based on a single QW. This is possible thanks to the energy dispersion of the lower polariton branch. Nevertheless, this device did not show a significant increase of the quantum efficiency, as expected from an electroluminescent device operating in the strong coupling regime. This was attributed to the presence of the dark states at the intersubband transition energy, that control the electronic transport.

We decided, then, to look for another photon confinement scheme to obtain dispersion-less states and increase the Rabi splitting, with the aim of facilitating a selective electrical injection in the polariton states, avoiding the dark states. We chose to use a very thin MDM cavity with a metallic grating as the top metallic mirror. We first demonstrated the feasibility of such cavity in the MIR. We showed the continuous tunability of the cavity mode by changing the metallic strip width and the possibility of either having a flat energy dispersion as a function of the inplane wave vector or coupling the cavity mode with a SPP by choosing the appropriate periodicity of the grating. We finally inserted doped QWs in MDM cavities to observe the strong coupling regime. Three samples with different electronic densities gave a Rabi splitting at room temperature of $9.5meV$, $14meV$ and $21.5meV$ by using only 10 QWs and a cavity thickness of $259nm$. The most doped sample presented a photonic gap between the two polariton branches which is the experimental signature of the ultra-strong coupling regime. We finally demonstrated a flat dispersion of the polariton branches obtained thanks to the geometry of the cavities.

6.2   Perspectives

The perspectives of my work are, first to inject photons in polariton states using an internal electrically tunable MIR source in a planar cavity and second to realize electroluminescence measurements in the metal-dielectric-metal cavities. The preliminary experimental results I obtained for those two purposes are detailed in appendix A.

On a more general point of view, the research on ISB devices operating in the strong coupling regime is expanding very rapidly, both on the experimental and theoretical side. Two main objectives are pursued: the realization of efficient inversion-less emitters and the realization of sub-THz devices. The work presented in this manuscript proposed new devices for the first objective. In order to obtain efficient emitters the first step is now to complete the investigation for electrical injection in the MDM cavities. Indeed, the

data of chapter 4 and 5 allowed us to optimize the grating parameters to obtain the best absorption in this geometry. We now need to optimize the parameters for the inverse mechanism as we want to extract light from the MDM cavity through EL measurements. Therefore, we need to find out the best geometry for light extraction, by exploiting the properties of the gratings.

Another perspective is the realisation of devices based on polariton stimulated emission. This approach is pursued by Aymeric Delteil in his PhD thesis. He realized an $InAs/AlSb$ QCS to inject electrons in the upper polariton branch. He observed in the EL spectra two features, corresponding to the upper and lower branches, separated by the energy of a LO phonon. This is the signature of a phonon-polariton interaction [Delteil et al., 2011]. A theoretical proposal was published in [De Liberato and Ciuti, 2009b] suggesting that the transition from the upper to the lower polariton branch through phonon relaxation could lead to an inversion-less laser thanks to the bosonic character of the polaritons.

As demonstrated in chapter 5, the Rabi splitting in our devices depends on the difference between the electronic populations in the subbands $N_1 - N_2$ (see equation 1.28). To optimize the strong coupling, the Fermi level must thus be slightly below the second subband. It has been both theoretically and experimentally demonstrated that for high electronic densities the optical response of a 2DEG is strongly modified by the collective nature of the intersubband resonance [Luin et al., 2001, Warburton et al., 1998]. In particular, when several subbands are occupied, the optical response of the system can be concentrated into a single resonance with an increased oscillator strength, at greater energy than the single particle transition. In our group we used a $GaInAs/AlInAs$ highly doped structure with five occupied subbands and coupled it with a planar cavity to obtain an ultra-strong coupling regime, with a Rabi splitting of $55meV$ for an ISB transition at $160meV$. The results from this study are in an article under submission and open a new perspective to increase even more the light-matter coupling in MDM cavities, both in the mid and far-infrared.

Bibliography

[Adams, 1981] Adams, M. J. (1981). *An introduction to Optical Waveguides.* John Wiley & Sons, Chichester. (Cited on page 73.)

[Anappara et al., 2005] Anappara, A. A., Tredicucci, A., Biasiol, G., and Sorba, L. (2005). Electrical control of polariton coupling in intersubband microcavities. *Applied Physics Letters*, 87:051105. (Cited on page 15.)

[Ando et al., 1982] Ando, T., Fowler, A. B., and Stern, F. (1982). Electronic properties of two-dimensional systems. *Review of Modern Physics*, 54:437. (Cited on page 10.)

[Babuty et al., 2010] Babuty, A., Bousseksou, A., Tetienne, J.-P., Doyen, I. M., Sirtori, C., Beaudoin, G., Sagnes, I., De Wilde, Y., and Colombelli, R. (2010). Semiconductor surface plasmon sources. *Phys. Rev. Lett.*, 104(22):226806. (Cited on page 93.)

[Bastard, 1988] Bastard, G. (1988). *Wave mechanics applied to semiconductor heterostructures.* Monographies de physique. Les Éditions de Physique. (Cited on page 6.)

[Benisty et al., 1998] Benisty, H., Stanley, R., and Mayer, M. (1998). Method of source terms for dipole emission modification in modes of arbitrary planar structures. *J. Opt. Soc. Am. A*, 15(5):1192–1201. (Cited on page 51.)

[Benveniste et al., 2009] Benveniste, E., Laurent, S., Vasanelli, A., Manquest, C., Sirtori, C., Teulon, F., Carras, M., and Marcadet, X. (2009). Measurement of gain and losses of a mid-infrared quantum cascade laser by wavelength chirping spectroscopy. *Applied Physics Letters*, 94:081110. (Cited on page 49.)

[Benveniste et al., 2008] Benveniste, E., Vasanelli, A., Delteil, A., Devenson, J., Teissier, R., Baranov, A., Andrews, A., Strasser, G., Sagnes, I., and Sirtori, C. (2008). Influence of the material parameters on quantum cascade devices. *Applied Physics Letters*, 93(13):131108. (Cited on page 45.)

[Blaser et al., 2002] Blaser, S., Diehl, L., Beck, M., Faist, J., Oesterle, U., Xu, J., Barbieri, S., and Beltram, F. (2002). Characterization and modeling of quantum cascade lasers based on a photon-assisted tunneling transition. *IEEE JOURNAL OF QUANTUM ELECTRONICS*, 37(3):448. (Cited on page 129.)

[Cai et al., 2000] Cai, M., Painter, O., and Vahala, K. J. (2000). Observation of critical coupling in a fiber taper to a silica-microsphere whispering-gallery mode system. *Phys. Rev. Lett.*, 85(1):74–77. (Cited on page 85.)

[Ciuti et al., 2005] Ciuti, C., Bastard, G., and Carusotto, I. (2005). Quantum vacuum properties of the intersubband cavity polariton field. *Physical Review B*, 72:115303. (Cited on page 110.)

[Ciuti and Carusotto, 2006] Ciuti, C. and Carusotto, I. (2006). Input-output theory of cavities in the ultrastrong coupling regime: The case of time-independent cavity parameters. *Physical Review A*, 74(3):033811. (Cited on page 41.)

[Colombelli et al., 2005] Colombelli, R., Ciuti, C., Chassagneux, Y., and Sirtori, C. (2005). Quantum cascade intersubband polariton light emitters. *Semiconductor Science and Technology*, 20(10):985. (Cited on page 60.)

[De Liberato and Ciuti, 2009a] De Liberato, S. and Ciuti, C. (2009a). Quantum theory of electron tunneling into intersubband cavity polariton states. *Physical Review B*, 79:075317. (Cited on pages 41 and 67.)

[De Liberato and Ciuti, 2009b] De Liberato, S. and Ciuti, C. (2009b). Stimulated scattering and lasing of intersubband cavity polaritons. *Physical Review Letters*, 102:136403. (Cited on page 119.)

[Delteil et al., 2011] Delteil, A., Vasanelli, A., Jouy, P., Barate, D., Moreno, J., Teissier, R., Baranov, A., and Sirtori, C. (2011). Optical phonon scattering of cavity polaritons in an electroluminescent device. *Physical Review B*, 83:081404(R). (Cited on pages 119 and 131.)

[Dini et al., 2003] Dini, D., Köhler, R., Tredicucci, A., Biasiol, G., and Sorba, L. (2003). Microcavity polariton splitting of intersubband transitions. *Physical Review Letters*, 90(12):116401. (Cited on pages 2, 15 and 36.)

[Dupont et al., 2003] Dupont, E., Liu, H. C., SpringThorpe, A. J., Lai, W., and Extavour, M. (2003). Vacuum-field rabi splitting in quantum-well infrared photodetectors. *Phys. Rev. B*, 68:245320. (Cited on page 40.)

[Faist et al., 1994] Faist, J., Capasso, F., Sivco, D. L., Sirtori, C., Hutchinson, A. L., and Cho, A. Y. (1994). Quantum cascade laser. *Science*, 264(5158):553–556. (Cited on page 1.)

[Foster et al., 2000] Foster, G. T., Mielke, S. L., and Orozco, L. A. (2000). Intensity correlations in cavity qed. *Phys. Rev. A*, 61:053821. (Cited on page 14.)

[Geiser et al., 2010] Geiser, M., Walther, C., Scalari, G., Beck, M., Fischer, M., Nevou, L., and Faist, J. (2010). Strong light-matter coupling at terahertz frequencies at room temperature in electronic lc resonators. *Appl. Phys. Lett.*, 97(19):191107. (Cited on page 111.)

[Haes and Van Duyne, 2002] Haes, A. J. and Van Duyne, R. P. (2002). A nanoscale optical biosensor: Sensitivity and selectivity of an approach based on the localized surface plasmon resonance spectroscopy of triangular silver nanoparticles. *Journal of the American Chemical Society*, 124(35):10596–10604. PMID: 12197762. (Cited on page 93.)

[Hibbins et al., 2006] Hibbins, A. P., Murray, W. A., Tyler, J., Wedge, S., Barnes, W. L., and Sambles, J. R. (2006). Resonant absorption of electromagnetic fields by surface plasmons buried in a multilayered plasmonic nanostructure. *Phys. Rev. B*, 74(7):073408. (Cited on page 79.)

[Hibbins et al., 2004] Hibbins, A. P., Sambles, J. R., Lawrence, C. R., and Brown, J. R. (2004). Squeezing millimeter waves into microns. *Phys. Rev. Lett.*, 92(14):143904. (Cited on page 71.)

[Houdré, 2005] Houdré, R. (2005). Early stages of continuous wave experiments on cavity-polaritons. *physica status solidi (b)*, 242(11):2167–2196. (Cited on page 52.)

[Houdré et al., 1994] Houdré, R., Weisbuch, C., Stanley, R. P., Oesterle, U., Pellandini, P., and Ilegems, M. (1994). Measurement of cavity-polariton dispersion curve from angle-resolved photoluminescence experiments. *Phys. Rev. Lett.*, 73(15):2043–2046. (Cited on page 52.)

[Jouy et al., 2011a] Jouy, P., Todorov, Y., Vasanelli, A., Colombelli, R., Sagnes, I., and Sirtori, C. (2011a). Coupling of a surface plasmon with localized subwavelength microcavity modes. *Appl. Phys. Lett.*, 98(02):021105. (Cited on page 72.)

[Jouy et al., 2011b] Jouy, P., Vasanelli, A., Todorov, Y., Delteil, A., Biasiol, G., Sorba, L., and Sirtori, C. (2011b). Transition from strong to ultra-strong coupling regime in mid-infrared metal-dielectric-metal cavities. *Applied Physics Letters*, 98(23):231114. (Cited on page 100.)

[Jouy et al., 2010] Jouy, P., Vasanelli, A., Todorov, Y., Sapienza, L., Colombelli, R., Gennser, U., and Sirtori, C. (2010). Intersubband electroluminescent devices operating in the strong coupling regime. *Physical Review B*, 82:045322. (Cited on pages 20 and 41.)

[Kumar et al., 2007] Kumar, S., Williams, B. S., Qin, Q., Lee, A. W., Hu, Q., and Reno, J. L. (2007). Surface-emitting distributed feedback tera-hertz quantum-cascade lasers in metal-metal waveguides. *Opt. Express*, 15(1):113–128. (Cited on page 75.)

[Lal et al., 2007] Lal, S., Link, S., and Halas, N. J. (2007). Nano-optics from sensing to waveguiding. *Nature Photonics*, 1:641. (Cited on page 93.)

[Landau and Lifchits, 1994] Landau, L. and Lifchits, E. (1994). *Physique théorique: Théorie des champs*, volume 2. Editions Mir. (Cited on page 50.)

[Leuliet et al., 2006] Leuliet, A., Vasanelli, A., Wade, A., Fedorov, G., Smirnov, D., Bastard, G., and Sirtori, C. (2006). Electron scattering spectroscopy by a high magnetic field in quantum cascade lasers. *Physical Review B*, 73:085311. (Cited on page 60.)

[Liebermann and Knoll, 2000] Liebermann, T. and Knoll, W. (2000). Surface-plasmon field-enhanced fluorescence spectroscopy. *Colloids and Surfaces A: Physicochemical and Engineering Aspects*, 171(1-3):115 – 130. (Cited on page 93.)

[Liu and Capasso, 2000] Liu, H. and Capasso, F. (2000). *Intersubband transitions in quantum wells: Physics and device applications I*. Number vol. 1 ;vol. 62 in Semiconductors and semimetals. Academic Press. (Cited on pages 9 and 10.)

[Lockyear et al., 2009] Lockyear, M. J., Hibbins, A. P., Sambles, J. R., Hobson, P. A., and Lawrence, C. R. (2009). Thin resonant structures for an-gle and polarization independent microwave absorption. *Appl. Phys. Lett.*, 94(04):041913. (Cited on page 71.)

[Luin et al., 2001] Luin, S., Pellegrini, V., Beltram, F., Marcadet, X., and Sirtori, C. (2001). Interplay between disorder and intersubband collective excitations in the two-dimensional electron gas. *Phys. Rev. B*, 64:041306. (Cited on page 119.)

[Lukosz and Kunz, 1977] Lukosz, W. and Kunz, R. E. (1977). Light emission by magnetic and electric dipoles close to a plane interface. i. total radiated power. *J. Opt. Soc. Am.*, 67(12):1607–1615. (Cited on page 51.)

[Maineult et al., 2008] Maineult, W., Gellie, P., Andronico, A., Filloux, P., Leo, G., Sirtori, C., Barbieri, S., Peytavit, E., Akalin, T., Lampin, J.-F., Beere, H. E., and Ritchie, D. A. (2008). Metal-metal terahertz quantum cascade laser with micro-transverse-electromagnetic-horn antenna. *Appl. Phys. Lett.*, 93(18):183508. (Cited on page 75.)

[Palik, 1998] Palik, E. D. (1998). *Handbook of Optical Constants of Solids*. Academic Press, San Diego. (Cited on page 85.)

[Raimond et al., 2001] Raimond, J. M., Brune, M., and Haroche, S. (2001). Manipulating quantum entanglement with atoms and photons in a cavity. *Rev. Mod. Phys.*, 73:565–582. (Cited on page 11.)

[Sapienza et al., 2007] Sapienza, L., Vasanelli, A., Ciuti, C., Manquest, C., Sirtori, C., Colombelli, R., and Gennser, U. (2007). Photovoltaic probe of cavity polaritons in a quantum cascade structure. *Applied Physics Letters*, 90:201101. (Cited on pages 36 and 41.)

[Sapienza et al., 2008] Sapienza, L., Vasanelli, A., Colombelli, R., Ciuti, C., Chassagneux, Y., Manquest, C., Gennser, U., and Sirtori, C. (2008). Electrically injected cavity polaritons. *Physical Review Letters*, 100:136806. (Cited on pages 2, 19 and 41.)

[Sirtori et al., 1994] Sirtori, C., Capasso, F., Faist, J., and Scandolo, S. (1994). Nonparabolicity and a sum rule associated with bound-to-bound and bound-to-continuum intersubband transitions in quantum wells. *Physical Review B*, 50(12):8663. (Cited on page 7.)

[Stanley et al., 1996] Stanley, R. P., Houdré, R., Weisbuch, C., Oesterle, U., and Ilegems, M. (1996). Cavity-polariton photoluminescence in semiconductor microcavities: Experimental evidence. *Physical Review B*, 53(16):10995. (Cited on page 52.)

[Todorov et al., 2010a] Todorov, Y., Andrews, A. M., Colombelli, R., De Liberato, S., Ciuti, C., Klang, P., Strasser, G., and Sirtori, C. (2010a). Ultra-strong light-matter coupling regime with polariton dots. *Physical Review Letters*, 105:196402. (Cited on pages 15, 17 and 109.)

[Todorov et al., 2008] Todorov, Y., Jouy, P., Vasanelli, A., Sapienza, L., Colombelli, R., Gennser, U., and Sirtori, C. (2008). Stark tunable electroluminescence from cavity polariton states. *Applied Physics Letters*, 93:171105. (Cited on pages 20 and 41.)

[Todorov and Minot, 2007] Todorov, Y. and Minot, C. (2007). Modal method for conical diffraction on a rectangular slit metallic grating in a multilayer structure. *J. Opt. Soc. Am. A*, 24(10):3100–3114. (Cited on page 75.)

[Todorov et al., 2010b] Todorov, Y., Tosetto, L., Teissier, J., Andrews, A. M., Klang, P., Colombelli, R., Sagnes, I., Strasser, G., and Sirtori, C. (2010b). Optical properties of metal-dielectric-metal microcavities in the thz frequency range. *Optics Express*, 18(13):13886–13907. (Cited on page 72.)

[Warburton et al., 1998] Warburton, R. J., Weilhammer, K., Kotthaus, J. P., Thomas, M., and Kroemer, H. (1998). Influence of collective effects on the linewidth of intersubband resonance. *Phys. Rev. Lett.*, 80:2185–2188. (Cited on page 119.)

[Weisbuch et al., 2000] Weisbuch, C., Benisty, H., and Houdré, R. (2000). Overview of fundamentals and applications of electrons, excitons and photons in confined structures. *Journal of Luminescence*, 85(4):271 – 293. (Cited on page 52.)

[Załużny, 1991] Załużny, M. (1991). Intersubband absorption line broadening in semiconductor quantum wells: Nonparabolicity contribution. *Phys. Rev. B*, 43:4511–4514. (Cited on page 10.)

Appendix A

Preliminary results

This chapter presents the preliminary experimental results obtained on two different samples during my PhD.

A.1   Electrically driven photonic injection in the polariton states

The samples presented in this section were grown in LPN (Laboratoire de Photonique et de Nanostructures) by Ulf Gennser.

Our goal is to inject photons in polariton states using an internal electrically tunable MIR source in a planar cavity (as in chapters 2 and 3). Figure A.1 represents a scheme of the sample chemically etched in a mesa device (with a $200\mu m$ diameter).
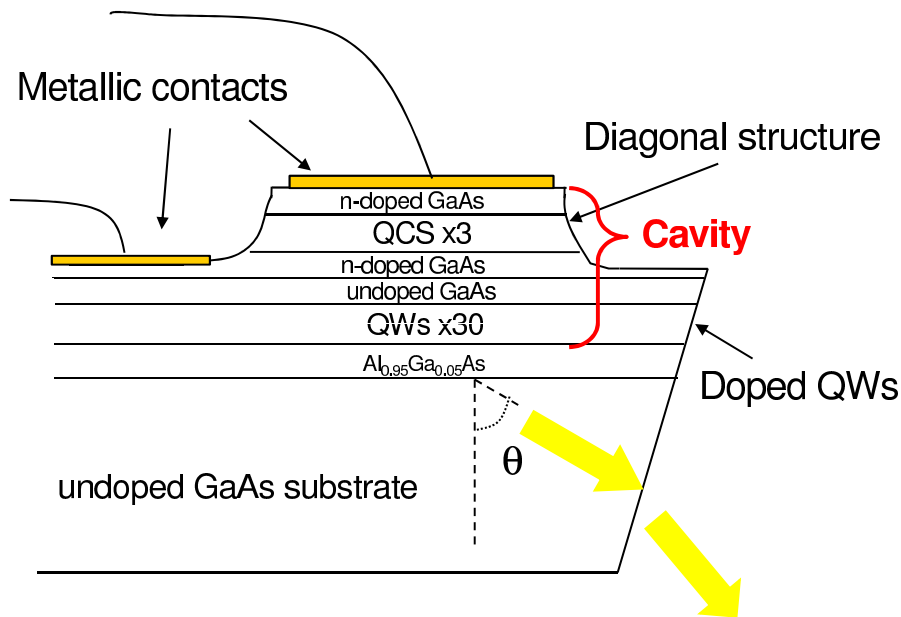
Figure A.1: Scheme of the device for electroluminescence measurements

From top to bottom (the detailed growth sheet is in appendix B.2): the metal layer ($Pd(25nm)/Ge(75nm)/Ti(10nm)/Au(200nm)$ annealed at $350°C$) is used both as a top mirror and as the top ohmic contact; the doped $GaAs$ layer ensure an equal distribution of the current on the entire sample surface. A 3 period QCS is then grown followed by another doped $GaAs$ layer used as a conductive layer to report the bottom contact on the side of the mesa. A $GaAs$ cladding is then necessary to electrically isolate the following

30 highly doped $GaAs/Al_{0.45}Ga_{0.55}As$ ($7.2nm/12nm$) QWs. The intersubband transition between the first two levels of these QWs is coupled with the cavity mode. The structure ends with an $Al_{0.95}Ga_{0.05}As$ low refractive index layer which acts as the bottom mirror of the cavity before an undoped $GaAs$ substrate. The electrons injected with the two electric contacts only circulate in the QCS while the QWs are isolated. Therefore, the chemical etching of the mesa needs to be stopped in the middle of the lower doped $GaAs$ layer using a profilometer to follow the etching depth during the process.

A.1.1 The diagonal QCS

The QCS is based on a diagonal transition [Blaser et al., 2002]. Figure A.2 represents the computed band diagram for two periods as a function of z under a bias of $0.21V$ per period. The black line represents the conduction band profile and the colored curves represent the square moduli of the wave functions plotted at the corresponding energy. The ground and excited states of the diagonal transition are in bold color line and respectively labeled 1 and 2. The injection and extraction minibands are engineered so that the structure can work on a broad bias voltage range. Because the two levels of the diagonal transition are localized in two different QWs, their energy difference is very dependent on the voltage, due to Stark effect. As a consequence, the photon energy can be tuned by applying different voltages.

In order to test the tunability of the QCS, we realized a reference sample with 20 periods of the QCS instead of 3 and without the bottom mirror and the doped QWs. The left panel of figure A.3 summarizes the EL spectra measured at $77K$ for different voltages on the reference sample. The spectra are normalized for better clarity. By tuning the applied voltage from $1.5V$ to $7.5V$, the peak of EL is tuned from $115meV$ up to $142meV$ as shown in the right panel where the energy of the EL peak is represented as a function of the voltage.

A.1.2 Absorption and EL measurements

I realized angle resolved transmission measurements to passively characterize the sample and verify the strong coupling regime. The spectra, measured at room temperature, are shown in figure A.4 for the different measured angles. They are normalized and shifted for better clarity and two dashed curves underline the two polariton branches. We can clearly observe the anti-crossing when the cavity mode is at resonance with the intersubband transition energy and we obtain a splitting of $2\hbar\Omega_R \approx 15meV$ in the k space.
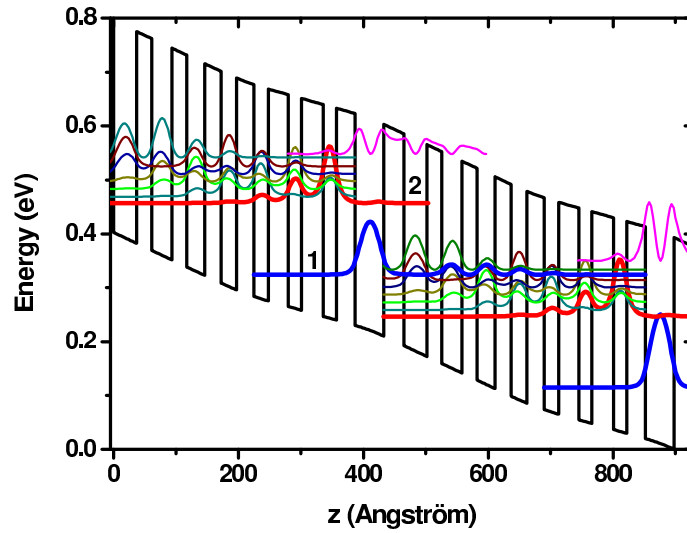
Figure A.2: Band diagram of the diagonal QCS calculated by solving Schrödinger and Poisson equations for a voltage of $0.21V$ per periods. The two states of the diagonal transition are in bold and labeled 1 and 2.
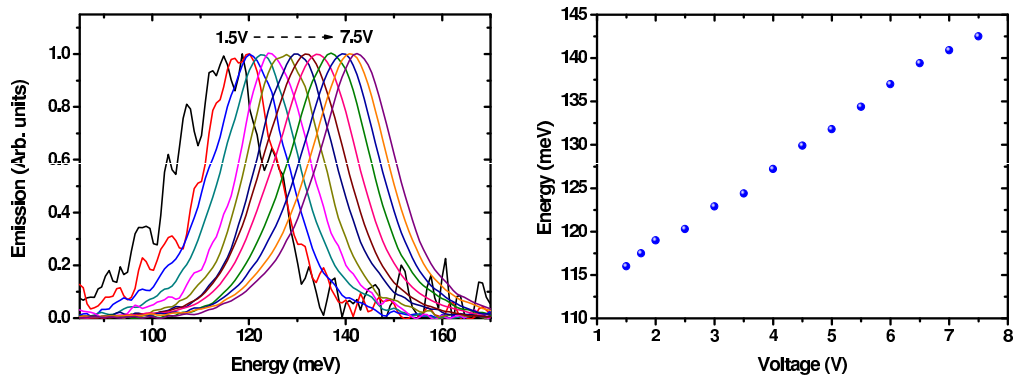

Figure A.3: Left panel: normalized EL spectra measured at $77K$ on the reference sample for voltages from $1.5V$ to $7.5V$ with $0.5V$ steps. Right panel: Energy of the EL peak measured at $77K$ as a function of the voltage applied on the sample.
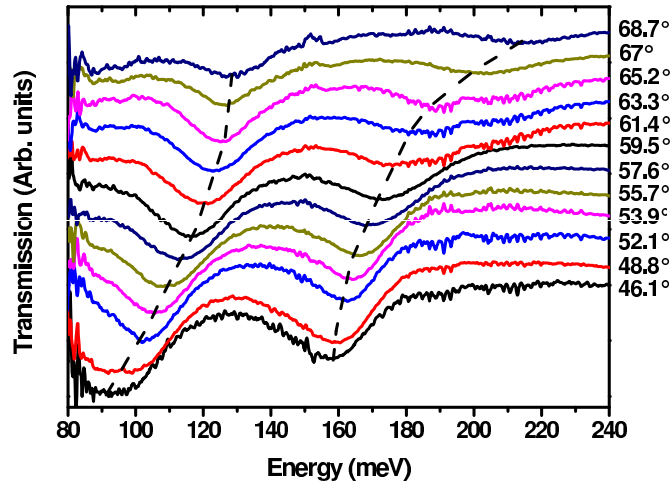
Figure A.4: Transmission spectra measured at room temperature for different angles of propagation of the light. The spectra are normalized and shifted and black dashed curves underline the two polariton branches.

In order to inject photons at different energies in the polariton dispersion, we realized angle resolved EL measurements for different voltages applied on the QCS. Figure A.5 summarizes the k space for $3V$, $4V$, $5V$ and $6V$ at $77K$. We report on each graph a fit of the EL spectrum measured on the reference sample at the same current. In a similar way to what observed in chapter 3, the EL follows the polariton dispersion in an energy window delimited by the linewidth of the QCS EL spectra. Additionally, one can notice for each voltage a signal peaked $\approx 36meV$ below the first contribution. This constant energy difference suggests to attribute this feature to a phonon replica of the polariton state populated by the emitted photons. This phonon-polariton scattering has already been reported in an ISB polaritonic sample [Delteil et al., 2011]. Further studies are necessary to confirm this interpretation and to complete the measurements shown in this section.

For optical pumping of the polariton states, our geometry is the most compact one as the photons are directly created within the same cavity mode as the polaritons. There is no need for an external source nor for optical alignment. While the polaritonic states are populated through their photonic component, their electronic component allows the interaction with the phonons giving the lower energy feature.

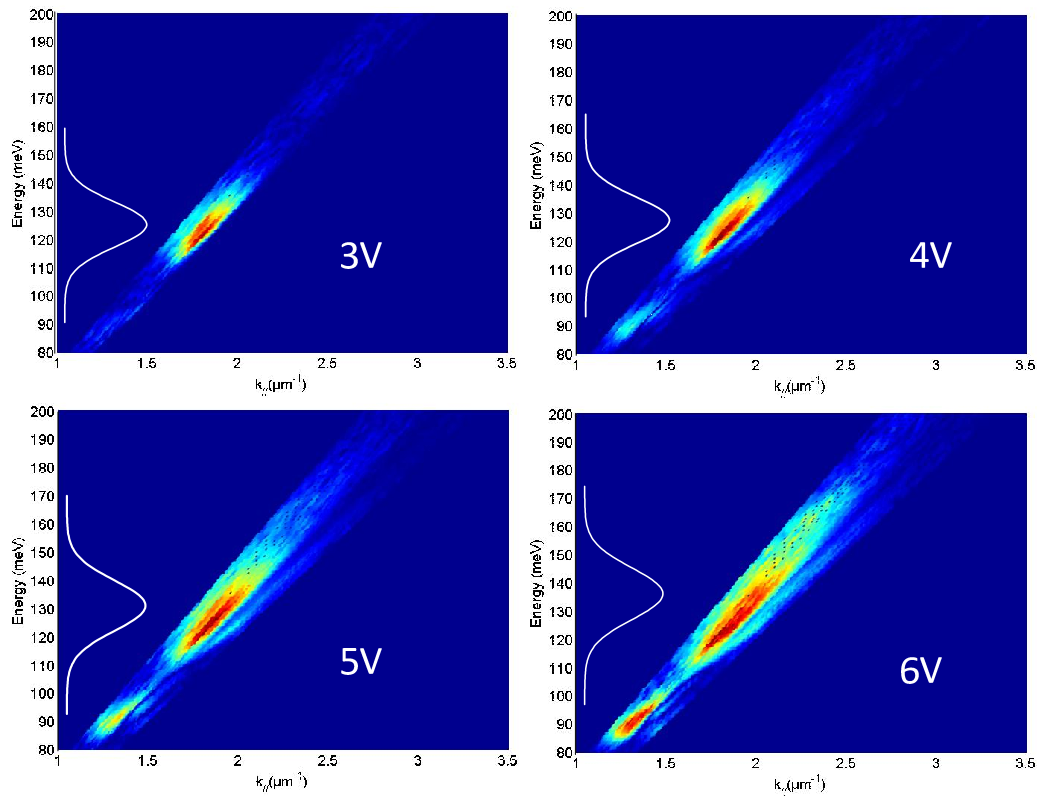Figure A.5: Contour plots of the EL measured at $77K$ for $3V$, $4V$, $5V$ and $6V$. The white lines are the fit of the EL spectra measured on the reference sample for similar currents.

A.2 Electrical injection in MDM cavities

In this section, I will present the preliminary results obtained on a sample designed for electrical injection in the polariton states in a MDM cavity.

A.2.1 Sample description

In order to design a QCS suitable for strong coupling in MDM cavities, it is important to consider that the Rabi splitting depends on the overlap between the QWs and the cavity mode, f_w, hence limiting the total length of the injector region. I designed a device with a $201.8nm$ thick AR, based on only 5 QCS periods. Figure A.6 represents the computed band diagram for two periods of the QCS as a function of z under a bias of $0.14V$ per period. The black line represents the conduction band profile and the colored curves represent the square moduli of the wave functions plotted at the corresponding energy. The ground and excited states of the transition are in bold color line and respectively labeled 1 and 2. As one can notice, only two QWs are used as the injection miniband. Such a short QCS was chosen to reach the best ratio between the width of the QW where the ISB transition takes place and the rest of the QCS in order to increase f_w and hence the Rabi frequency. As in the structure of chapter 3, a thick extraction barrier ensure a long tunneling time out of the main QW.

Two reference samples were realized to test the QCS. They consist of 5 and 20 periods of the diagonal QCS processed in mesas (same geometry as in chapter 3), without photonic cavity (the top of the mesa is covered with metal for the electrical contact but no low refractive index layer is used on the other side of the AR). The left panel of figure A.7 shows EL spectra of both samples (black curve for 5 periods and blue curve for 20 periods) for similar current. They have the same shape and are peaked around $125meV$. This demonstrates that the QCS works as well for 5 than for 20 periods and that the very thin AR is not a problem for EL measurements.

In order to compare the electric characteristics of the samples with ohmic and non-ohmic contacts, we used two different metallic alloys for the electric contact on the 5 periods reference sample. The non ohmic contact is made of $Ti(10nm)Au(200nm)$ while the ohmic contact is made of $Pd(25nm)/Ge(75nm)/Ti(10nm)/Au(200nm)$ annealed at $350°C$ to diffuse the Ge in the doped $GaAs$ layer on each side of the AR. The use of $PdGe$ alloy allows a smaller diffusion length compared to $NiGe$ for example allowing a thinner doped $GaAs$ layer and thus giving a greater value for f_w and reducing the radiative losses due to free carrier absorption. The right panel of figure A.7 presents the voltage-current characteristics for both contacts.
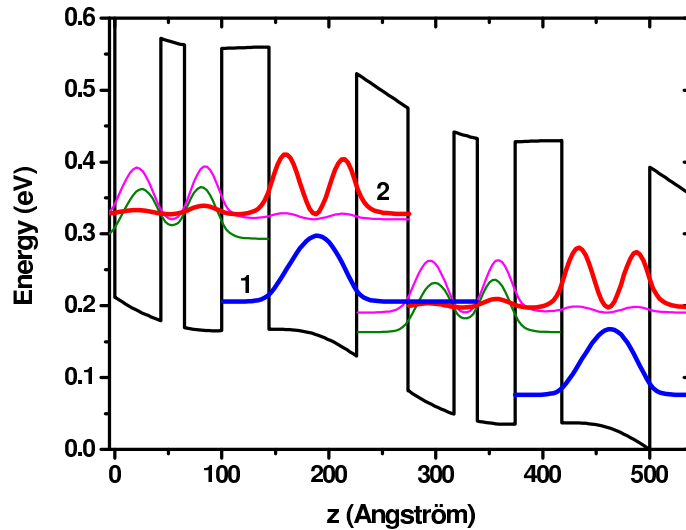
Figure A.6: Calculated band structure of the QCS for a voltage of $0.14V$ per periodes. The fundamental and excited states of the ISB transition are in bold and respectively labeled 1 and 2.

For the same current in the structure, the non-ohmic contact requires a more important applied voltage on the QCS. This is due to the presence of a Schottky barrier at the interface between the $TiAu$ alloy and the doped $GaAs$ layer. In the MDM, the grating is realized by using $TiAu$ mirrors. In order to avoid Schottky barriers for the injected electrons, I realized a $PdGeTiAu$ contact on the back of the sample and polarized the device to have the back contact at ground.

The same processing as in figure 4.10 was used to realize the MDM cavity. Nevertheless, few additional steps are necessary to realize the contacts used for the electrical injection in the QCS. They are schematized in figure A.8. The first step consists in depositing a metallic pad that contacts every metallic strip of the grating and is large enough to allow the wire bonding. Therefore we use an optical lithography followed by a metallic evaporation and a lift-off. The second step consists in the chemical etching of the sample around the grating to reach the bottom metallic layer to realize the wire bonding of the bottom contact. To do so, we realize another optical lithography to protect with the resist the grating and the contact previously deposited. A $H_2SO_4/H_2O_2/H_2O$ (1 / 8 / 80) solution is used to etch the AR. Figure A.9 shows an optical microscope picture of the final sample. We can see several gratings with a top contact pad on each of them.

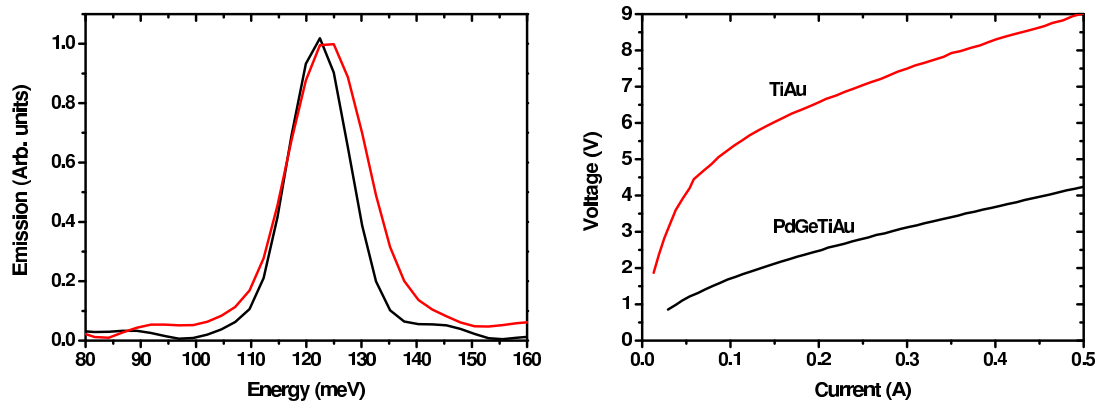Figure A.7: Left panel: EL spectra for the reference samples with 5 (black curve) and 20 (red curve) periods of the QCS. Right panel: V(I) characteristics for a $TiAu$ (red curve) and a $PdGeTiAu$ electric contact.
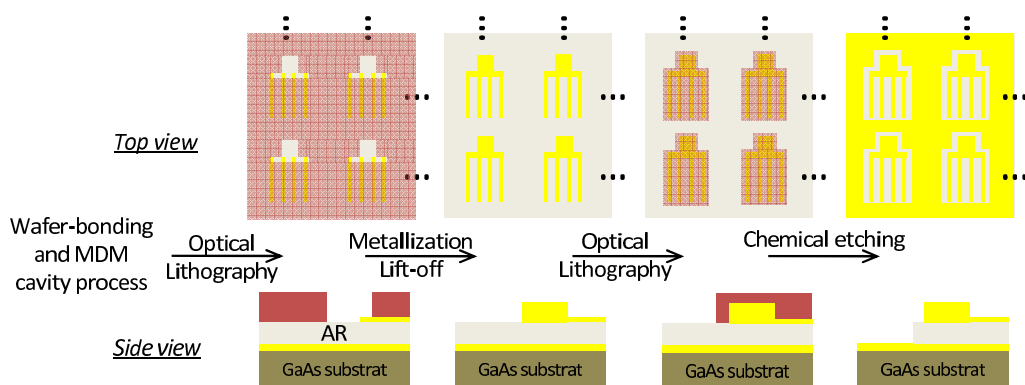

Figure A.8: Scheme of the process steps for EL MDM samples.
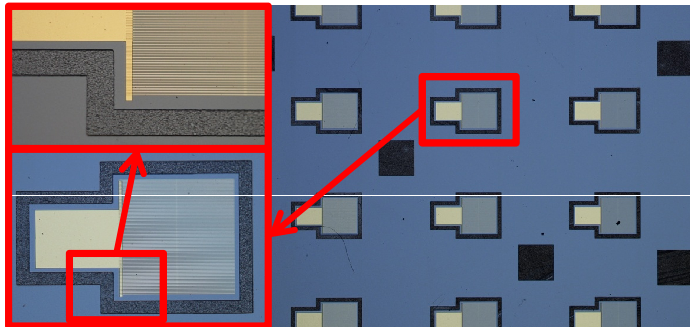
Figure A.9: Optical microscope picture of gratings processed for EL measurements.

A.2.2   Reflectivity and electrical characterizations

In order to obtain the optical dispersion of the device, we first realized reflectivity measurements on gratings with different metallic strip width. The left panel of figure A.10 shows few spectra close to the resonance between the cavity mode and the intersubband transition. They are normalized and shifted for better clarity. In the right panel of figure A.10, we plot with red curves the energy position of the minima from the reflectivity spectra as a function of $1/s$. We observe a splitting between the two branches, experimental signature of the strong coupling regime. The minimum splitting is obtained for $s = 1.15\mu m$ and is of $2\hbar\Omega_R \approx 10meV$.

Figure A.11 shows the electrical characteristic $(V(I))$ of the sample. The QCS aligns at a voltage of $\approx 0.6V$ as expected from our simulations.

Figure A.12 summarizes the first EL spectra obtained at $77K$ for gratings with different metallic strip width. They are normalized and shifted. Two peaks appear: one at the intersubband transition energy and one following the cavity mode energy as we tune s. Unfortunately, a series of deeps in the peaks attributed to a bad lock-in detection configuration (part of the interferogram is negative) degrades the clarity of the spectra. It is thus difficult to clearly interpret the intensity ratio between the two contributions and to observe the Rabi splitting for the EL. Those measurements are nevertheless promising as they represent the first EL for those cavities in the MIR.
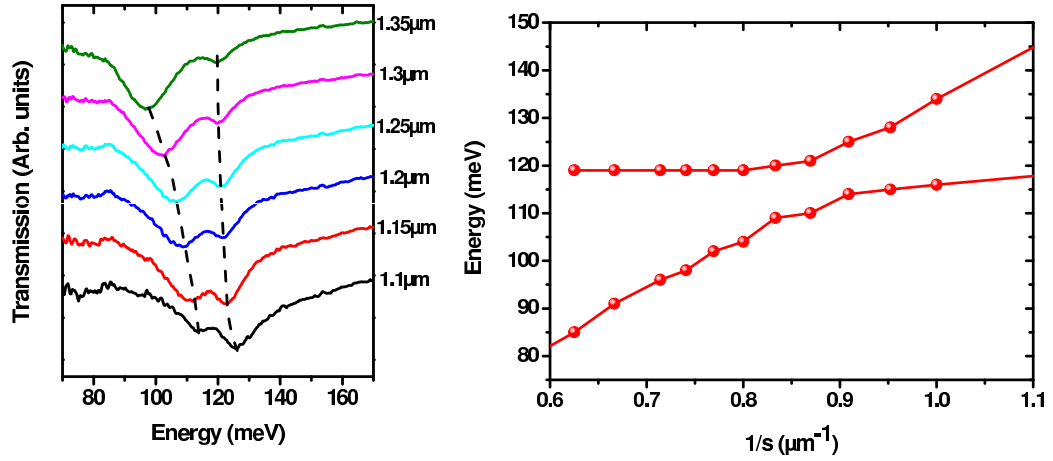
Figure A.10: Left panel: reflectivity spectrum at room temperature for different values of s. The spectra are normalized and shifted. Dashed black curves underline the two polariton branches. Right panel: summary of the polariton energies as a function of $1/s$ obtained from the reflectivity measurements at room temperature.
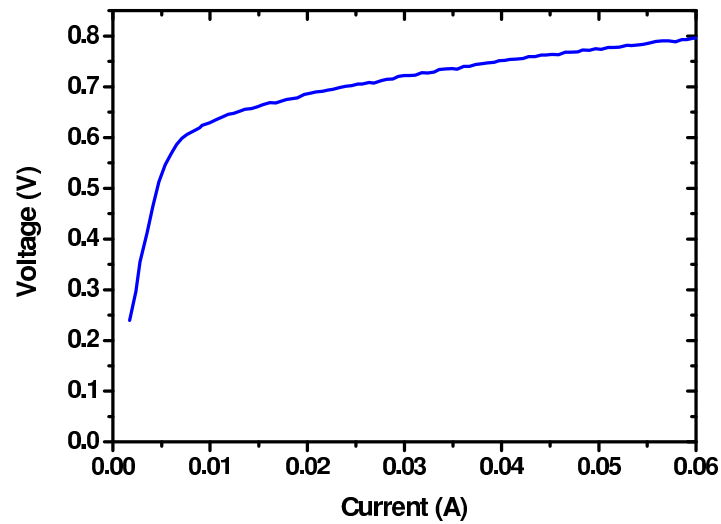
Figure A.11: V(I) characteristic at $77K$ of the sample for electrical injection in a MDM.
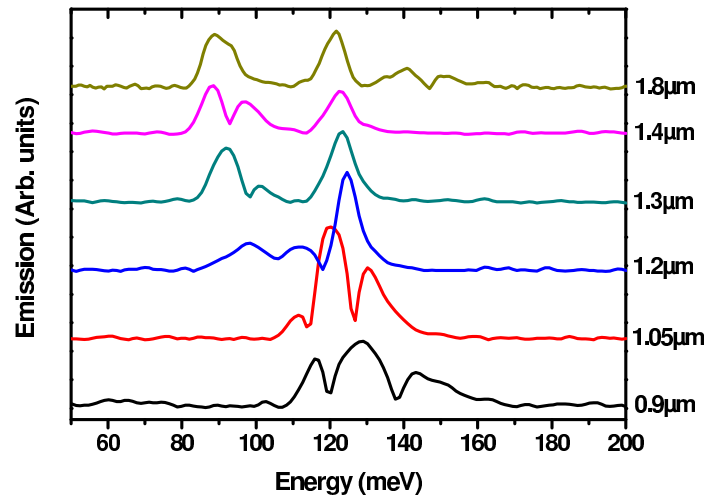
Figure A.12: EL spectra measured at $77K$ for a current of $100mA$ with different values of s. The spectra are shifted for better clarity.

Appendix B

Growth sheets

B.1   Structure chapter 2 and 3

Growth sheet of the sample used in chapters 2 and 3 for the electroluminescence from a sample in the strong coupling regime. The cavity is made of a top metallic mirror and low refractive index layers ($Al_{0.95}Ga_{0.05}As$ and doped $GaAs$). The QCS allows the injection of electrons in the main QW which contains a 2DEG.

The sample have been grown by Ulf Gennser at the Laboratoire Photonique et Nanostructures.

n^{++}	$GaAs$	$3.10^{18}cm^{-3}$	170Å	
n^{+}	$GaAs$	$1.10^{17}cm^{-3}$	860Å	
i	$GaAs$		22Å	
i	$Al_{0.45}Ga_{0.55}As$		22Å	
i	$GaAs$		18Å	
n	$Al_{0.45}Ga_{0.55}As$	$3.10^{17}cm^{-3}$	20Å	
n	$GaAs$	$3.10^{17}cm^{-3}$	19Å	
n	$Al_{0.45}Ga_{0.55}As$	$3.10^{17}cm^{-3}$	20Å	
n	$GaAs$	$3.10^{17}cm^{-3}$	23Å	repeat x30
n	$Al_{0.45}Ga_{0.55}As$	$3.10^{17}cm^{-3}$	18Å	
n	$GaAs$	$3.10^{17}cm^{-3}$	32Å	
i	$Al_{0.45}Ga_{0.55}As$		16Å	
i	$GaAs$		33Å	
i	$Al_{0.45}Ga_{0.55}As$		36Å	
i	$GaAs$		64Å	
i	$Al_{0.45}Ga_{0.55}As$		39Å	
i	$GaAs$		22Å	
i	$Al_{0.45}Ga_{0.55}As$		22Å	
i	$GaAs$		18Å	
n	$Al_{0.45}Ga_{0.55}As$	$3.10^{17}cm^{-3}$	20Å	
n	$GaAs$	$3.10^{17}cm^{-3}$	19Å	
n	$Al_{0.45}Ga_{0.55}As$	$3.10^{17}cm^{-3}$	20Å	
n	$GaAs$	$3.10^{17}cm^{-3}$	23Å	

n	$Al_{0.45}Ga_{0.55}As$	$3.10^{17}cm^{-3}$	18Å
n	$GaAs$	$3.10^{17}cm^{-3}$	32Å
i	Grading to $Al_{0.45}Ga_{0.55}As$		16Å
n^{++}	$GaAs$	$3.10^{18}cm^{-3}$	$0.56\mu m$
i	$Al_{0.95}Ga_{0.05}As$		$0.520\mu m$

Undoped GaAs substrate

B.2   Photonic injection with a diagonal structure

Growth sheet of the sample presented in the appendix A.1 for the photonic injection in the polariton states. The cavity is made of a top metallic mirror and a low refractive index layers $(Al_{0.95}Ga_{0.05}As)$. The electrons circulate in a QCS with a diagonal transition producing photons which energy can be tuned by changing the applied voltage on the structure. Additionally, a passive region made of identical quantum wells containing 2DEG are in the cavity and are used to reach the strong coupling regime.

The sample have been grown by Ulf Gennser at the Laboratoire Photonique et Nanostructures.

n^{++}	$GaAs$	$3.10^{18}cm^{-3}$	200Å	
n^{+}	$GaAs$	$1.10^{17}cm^{-3}$	500Å	
i	$GaAs$		21Å	
i	$Al_{0.45}Ga_{0.55}As$		35Å	
i	$GaAs$		21Å	
i	$Al_{0.45}Ga_{0.55}As$		32Å	
n	$GaAs$	$2.10^{17}cm^{-3}$	23Å	
i	$Al_{0.45}Ga_{0.55}As$		28Å	
n	$GaAs$	$2.10^{17}cm^{-3}$	25Å	
i	$Al_{0.45}Ga_{0.55}As$		26Å	
n	$GaAs$	$2.10^{17}cm^{-3}$	29Å	repeat x3
i	$Al_{0.45}Ga_{0.55}As$		24Å	
i	$GaAs$		32Å	
i	$Al_{0.45}Ga_{0.55}As$		24Å	
i	$GaAs$		37Å	
i	$Al_{0.45}Ga_{0.55}As$		32Å	
i	$GaAs$		46Å	
i	$Al_{0.45}Ga_{0.55}As$		30Å	
i	$GaAs$		21Å	
i	$Al_{0.45}Ga_{0.55}As$		35Å	
i	$GaAs$		21Å	
i	$Al_{0.45}Ga_{0.55}As$		32Å	
n	$GaAs$	$2.10^{17}cm^{-3}$	23Å	
i	$Al_{0.45}Ga_{0.55}As$		28Å	
n	$GaAs$	$2.10^{17}cm^{-3}$	25Å	
i	$Al_{0.45}Ga_{0.55}As$		26Å	

n	$GaAs$	$2.10^{17}cm^{-3}$	29Å	
i	$Al_{0.45}Ga_{0.55}As$		24Å	
i	Grading to $Al_{0.45}Ga_{0.55}As$		32Å	
n^{++}	$GaAs$	$2.10^{18}cm^{-3}$	$0.2\mu m$	
i	$Al_{0.45}Ga_{0.55}As$		500Å	
n	$Al_{0.45}Ga_{0.55}As$	$2.10^{18}cm^{-3}$	120Å	
i	$GaAs$		72Å	repeat x30
n	$Al_{0.45}Ga_{0.55}As$	$2.10^{18}cm^{-3}$	120Å	
i	$Al_{0.95}Ga_{0.05}As$		$2\mu m$	

Undoped GaAs substrate

B.3   Electrical injection in a MDM cavity

Growth sheet of the sample presented in the appendix A.2 for the electrical injection in the polariton states in MDM cavities. The cavity is made of two metallic mirrors. A QCS with only two quantum wells for the injection miniband is used to resonantly inject in the polariton states.

The sample have been grown by Giorgio Biasiol at the laboratory TASC.

n^{++}	$GaAs$	$3.10^{18}cm^{-3}$	300Å	
i	$Al_{0.35}Ga_{0.65}As$		48Å	
n	$GaAs$	$3.10^{18}cm^{-3}$	43Å	
i	$Al_{0.35}Ga_{0.65}As$		22Å	
i	$GaAs$		35Å	
i	$Al_{0.35}Ga_{0.65}As$		44Å	
i	$GaAs$		82Å	
i	$Al_{0.35}Ga_{0.65}As$		48Å	repeat x5
n	$GaAs$	$3.10^{18}cm^{-3}$	43Å	
i	$Al_{0.35}Ga_{0.65}As$		22Å	
i	$GaAs$		35Å	
n^{++}	$GaAs$	$3.10^{18}cm^{-3}$	200Å	
i	$Al_{0.5}Ga_{0.5}As$	etch stop	$0.4\mu m$	

Undoped GaAs substrate

Publication list

Peer-reviewed international journals

1. P. Jouy, A. Vasanelli, Y. Todorov, A. Delteil, G. Biasiol, L. Sorba and C. Sirtori, *Transition from strong to ultra-strong coupling regime in mid-infrared metal-dielectric-metal cavities*, Appl. Phys. Lett. **98**, 231114 (2011).

2. A. Delteil, A. Vasanelli, P. Jouy, D. Barate, J.C. Moreno, R. Teissier, A.N. Baranov, and C. Sirtori, *Optical phonon scattering of cavity polaritons in an electroluminescent device*, Phys. Rev. B **83**, 081404(R) (2011).

3. P. Jouy, Y. Todorov, A. Vasanelli, R. Colombelli, I. Sagnes and C. Sirtori, *Coupling of a surface plasmon with localized subwavelength micro-cavity modes*, Appl. Phys. Lett. **98**, 021105 (2011).

4. P. Jouy, A. Vasanelli, Y. Todorov, L. Sapienza, R. Colombelli, U. Gennser, and C. Sirtori, *Intersubband electroluminescent devices operating in the strong coupling regime*, Phys. Rev. B **82**, 045322 (2010).

5. Y. Todorov, P. Jouy, A. Vasanelli, L. Sapienza, R. Colombelli, U. Gennser, and C. Sirtori, *Stark tunable electroluminescence from cavity polariton states*, Appl. Phys. Lett. **93**, 171105 (2008).

Oral presentations at int. conferences

1. P. Jouy, A. Vasanelli, Y. Todorov, A. Delteil, G. Biasiol, L. Sorba, and C. Sirtori, *Ultra-strong coupling in mid-infrared metal cavities*, OECS 2011 (Paris, France)

2. P. Jouy, Y. Todorov, A. Vasanelli, G. Biasiol, R. Colombelli, C. Sirtori, *Light-matter strong coupling in the mid-infrared region with metallic microcavities*, CLEO 2011 (Baltimore, USA)

3. P. Jouy, A. Vasanelli, Y. Todorov, R. Colombelli, U. Gennser and C. Sirtori, *Electrical injection of intersubband polaritons*, TERA-MIR 2009 (Turuná-Marmaris, Turkey)

Posters at int. conferences

1. P. Jouy, A. Vasanelli, Y. Todorov, A. Delteil, G. Biasiol, L. Sorba, and C. Sirtori, *Ultra-strong coupling in mid-infrared metal cavities*, ITQW 2011 (Badesi, Italy)

2. A. Delteil, A. Vasanelli, P. Jouy, D. Barate, J.C. Moreno, R. Teissier, A.N. Baranov, and C. Sirtori, *Optical phonon scattering of cavity polaritons in an electroluminescent device*, OECS 2011 (Paris, France)

3. P. Jouy, Y. Todorov, A. Vasanelli, R. Colombelli, I. Sagnes and C. Sirtori, *Coupling of a surface plasmon with localized subwavelength microcavity modes*, IQCLSW 2010 (Florence, Italy)

4. P. Jouy, A. Vasanelli, Y. Todorov, L. Sapienza, R. Colombelli, U. Gennser, and C. Sirtori, *Dispositifs électroluminescents en régime de couplage ultra-fort dans le moyen infrarouge*, J3N 2008 (Grenoble, France)

Acknowledgements

First of all I would like to acknowledge Alberto Bramati, Karl Unterrainer, Cristiano Ciuti, Jean-Jacques Greffet, Jean-Sébastien Lauret and Raffaele Colombelli for accepting to be members of my jury, for their scientific expertise and precious critical advices on my manuscript.

This adventure lasting 4 years would not have been as enjoyable without the great leadership of my different advisors: Carlo that always found the right words to motivate me, made this perfectly balanced atmosphere between authority and friendship (thanks again for the coat!) and for his refreshing enthusiasm for any new data; Angela for the many hours she devoted to my manuscript and articles, her availibility at anytime for scientific discussions, teaching questions or friendly conversations and for always taking great care of her PhD students (I think she was more stressed for my PhD defense than myself...); Yanko for introducing me to the experimental world of physics, sharing all his tips and theoretical knowledge on polaritons and double metal cavities and for his unlimited amount of jokes (both good and bad ones...). It has been an incredible pleasure and privilege to work with all of them. They will clearly remain good friends and mentors that I will refer to all along my carrier and personal life.

I am very greatful as well to all the members of MPQ laboratory and more specifically to the members that were in the QUAD group while I was here. Elsa Benveniste for teaching me her sample polishing technics and for the great evenings at "Le Chabert"; Wilfried Maineult for showing me how to use liquid nitrogen (even after 4 years using it I still find it magical...); Jean Teissier for his incredible amount of experimental tips, his inspiring overflowing energy and for sharing our similar interests for ski and rollerblades; Pierre Gellie for sharing the same office and the same challenges brought by the french administration requirements for a PhD during all these years and for his legendary calm and his friendship; Aymeric Delteil for his refreshing sarcasm and for his concern about my everyday hydration level ("On va boire un coup?"); Ariane Calvar for sharing the same office whilst coping with our blood temperature difference and for all the nice talks; Sabine Laurent for the funny discussions after few beers; Stefano Barbieri for a great visit to Istan-

bul; Marco Ravaro for his advises on motorbikes; Robert Steed for bringing some British classy gentlemanly style into the lab; Anna Yuk-Nga Chen for her constant smiles; Olivier Cathabard for his inspiring travel stories; Khalid Akalbi; David Barate; Benjamin Askenazy for continuing my work; Cheryl Feuillet-Palma; Margot Renaudat-Saint-Jean; Jean-Michel Manceau; Vishal Jagtap; Giulia Pegolotti; Maria Amanti; and to all the interns. All of them contributed with their own personalities to create a scientific and very friendly atmosphere necessary to fully enjoy our common passion for physics.

I would like to acknowledge as well all the staff from the different clean rooms I worked in during my PhD. In particular - in Paris diderot - Christophe Manquest for his kind and helpful approach, Pascal Filloux for his funny sarcasm and his advice and Stephane Suffit for helping me to become familiar with the new equipment; Michael Rosticher at ENS for teaching me and helping me with the e-Beam lithography; and at IEF: Jean-René Coudeville for showing me my first process, Raffaele Colombelli for his expertise and precious advice, Adel Bousseksou for his kindness and his constant smile, Elodie Strupiechonski for her support in conferences and for her help in clean room, Grégoire Sevin for showing me the substrate removal technic...

Finally, I wish to acknowledge Ulf Gennser and Isabelle Sagnes from the LPN and Giorgio Biasiol and Lucia Sorba from TASC for the growth of the different samples I studied during my PhD. I want to thank Sara Ducci for giving me the chance to integrate the master "DQN" where I first discovered the world of nano-science and where I met great comrades.

I believe that, at some point, research and science in general is all about personal interpretation of direct observations, datas or theories. Therefore, evolving among all the laboratories cited above and sharing opinions with all these colleagues was a great chance for me to develop my scientific back ground as well as my scientific approach in a very convivial atmosphere.

I am as well very indebted to Anne Servouze (thank you so much for all the candies...), Véronique Glorieux, Kounvary Thoun and Joëlle Mercier from the administration branch of the laboratory for simplifying the administrative work, allowing me to focus on my research work and to Patrick Lepert for helping me adjusting mechanic parts for the experimental setups.

Now comes the family and friends section... Those thanks to whom I managed to find a balance between work and other activities; those without whom I would not have been able to appreciate my PhD at its best.

I want to thank all the members of my family and particularly my parents that have always been there for me; Etienne for always supporting me, pushing me forward and for the long talks while jogging in Vincennes; Marie-Pierre for taking great care of me and helping me in so many ways; Margot for being

the cutest niece and for bringing me into her wild/crazy/magical/epic stories; Gabin for the great chat and the comforting smiles; Elise for introducing me to the Parisian life and for always being there for a good talk, Maïky and Bruno for welcoming me so many times for holidays, lunch or just nice family time; my grandfather and Philippe for constantly reminding me where I come from; everyone in the Marsan family and especially Jacques, Katherin, Franz, Hélène, Clara, Roxane & Samuel; "les Reigues": Antoine, Adèle, and Lili.

I can not thank enough my three best friends Ben (for showing me a new way to interact with people, for all the profound or shallow conversations and for being the best travel buddy), Hai Son (for being hilarious 24/7, for the amazing road trip around Vietnam and for being always full of surprise) and Joseph (for all the coffee break discussions, sharing and showing his vision of Paris and for trying to be a good wingman) as well as Laïna for being a great friend for more than 10 years and for introducing me to her art world. Many thanks to Rebecca, Mila, Ross and Joanna for the few month they spent in Paris during which we had such good times and for all the epic memories. Thanks Charles and Patoche for being amazing classmates and great companions. Thanks to Selene and Gabi for the crazy Parisian nights; Emi for her unforgettable drunk laugh, Philippe for the endless poker nights and the roller hockey games. Thanks to Elise W. for her help and for letting me borrow Ben as much as I wanted. Thanks to Marie for being there during my defense preparation, for all the talking I really fancied and for helping improve my english; thanks to Julie for everything she gave me and for her precious friendship; to Megan C. for her spontaneous nature and great travel stories; to Megan S. for making me discover London's hot spots and the swedish delights; to Laura for her great music tastes and for the endless walks in Paris nights; to Jana for good memories with crazy horses and for her generosity; to Amanda who motivated me to learn english; to Hélène for making me discover "Jaegger Bombs"; to Rachel for hosting me in Baltimore, showing me around and for the great rooftop party; to Andrea for wandering around Paris and for her charming personality; to Jess for the crazy nights in NYC; to Gerri for being a great host and giving me the best German beer; to Lesli for her incredible peach pies and for the picnics in Bures-sur-Yvette; to Eva for being a great presence and to all my others couchsurfers for enlightening me with their travel stories and for aiding me to conquer the english language.

Finally I would like to thank anyone that will read this manuscript (I wrote it specially for you!) and I would like to thank myself for being easy to work with (I don't think I could have done it without my help...) and for allowing me to enjoy this great journey at its fullest.